Structuring of polymer surface by evaporation of sessile microdrops

DISSERTATION

zur Erlangung des Grades "Doktor der Naturwissenschaften"

am Fachbereich Chemie/Pharmazie

der Johannes Gutenberg-Universität
in Mainz

vorgelegt von

Master-Chem. Guangfen Li

aus Tianjin (V. R. China)

Mainz – 2007

1. Berichterstatter: Prof. Dr. Hans-Jürgen Butt
2. Berichterstatter: Prof. Dr. Andreas Janshoff

Tag der mündlichen Prüfung: 22nd May, 2007

Die vorliegende Arbeit wurde unter Betreuung von Herrn Prof. Dr. Hans-Jürgen Butt im Zeitraum zwischen April 2004 bis März 2007 am Max-Plank-Institut für Polymerforschung, Mainz, Deutschland angefertigt.

ABSTRACT

In this thesis different homemade experimental setups were used to study (1) the evaporation dynamics of liquid mcirodrops on smooth, insoluble planar surfaces, (2) the microstructuring of soluble polymer surfaces by solvent drops, and (3) the interfacial tension between two immiscible slugs in a microcapillary, where evaporation is avoided.

(1) The evaporation dynamics of pure water drops on self-assembled monolayers of thiols and disulfides (SAMs) on gold showed a stronger pinning of the rim of the droplet, the more hydrophilic the surface was. The hydrophilicity was tuned by the end-groups of the SAM alkyl chains. The total evaporation time, t_{tot}, for drops with different initial volumes, V_0, obeys a power law of the type $V_0 = a \cdot \mathrm{t}_{\mathrm{tot}}^{b}$ with an exponent b differing from the theoretical expected value of 1.5 for a diffusion-limited evaporation. This is explained with an increased evaporation through a thin water layer in contact with the droplet.

(2) If a pendant toluene drop is deposited from a syringe tip on a soluble polystyrene (PS) surface by fast up- and downward motions of the substrate table (~ 9 mm/s), a concave microtopology is observed after drop evaporation. This can be explained by a flow of solvent and dissolved polymer to the rim during the evaporation of the pinned solvent drop, a phenomenon known from ring-like coffee-stains. When the retraction speed is decreased to 10 µm/s, polymer dissolution is favored and a convex structure is observed instead. This can be explained with a gelation of the polymer-rich droplet. Concave microstructures occurred even if the pendant drop was evaporating close to the polymer surface without contact. This can be attributed to a diffusion of toluene into PS.

Additionally, the dissolution rate of the polymer is decreasing with increasing molar mass. Thus, the microtoplogy changes from convex (gelation-driven), over concave (flow-driven), to disordered pile-ups (instability-driven). For the system polyethylmethacrylate/ethylacetate exclusively concave structures occured, most likely due to the lower dissolution and/or faster evaporation rate.

(3) The interfacial tensions between slugs of water and different organic solvents in a microcapillary were successfully measured with a novel homemade technique, especially useful for the application in microfluidics.

INDEX

1 INTRODUCTION AND MOTIVATION

The research on microdrops can be very interesting since they directly concern many application fields i.e. printing, coating, DNA stretching, firefighting and medicines. In firefighting, the drop sizes have profound influences on the flame cooling by water, since smaller drop has a larger surface to volume ratio, thus more heat can be taken during drop evaporation. An optimized drop diameter as ~ 0.3 mm is expected[1]. It can also affect the effectivity of some medicine when it is taken as spraying therapy for e.g. chronic lung disease. Commonly, only part of the inhalant dose can be adsorbed by the ill area of lung due to the drop size dependence. The droplet with diameter of 3 µm is for general respirability, and 5 µm drop is preferentially for deep lung respirability[2]. It is also found that the fluid-fixed DNA molecules can be easily stretched by a drop evaporation process, thus a further study can be performed immediately[3]. Although these applications seem very simple, it contains much more complex and challenging physics, which up to know, has not yet been well understood. Therefore a lot of effort has been made from either experimental aspect or theoretically aspect by dealing with varies cases for obtaining a reasonable explanation on it.

The studies of liquid drops can be principally categorized into two major research fields: the investigation of (i) a single sessile drop, on a planar solid surface, or (ii) single drop or adjacent drops traveling as liquid slugs in microfluidics or in microfluidics channel[4, 5] (3 rd section in yellow). In (i) the droplet is usually subject to evaporation, while in (ii) evaporation is minimized or hindered. Drop evaporation process has been investigated and then used for the description of the complex interactions between solid and liquid inter-phase for more than 100 years[6-10]. The research on drop evaporation can be divided into two separated branches: the evaporation of sessile drops on non-soluble (1st section in blue) or more recently on soluble substrates (2nd section in green) (**Figure 1**).

In this thesis, different aspects of liquid drop concerning each of sections according to the sketch will be studied.

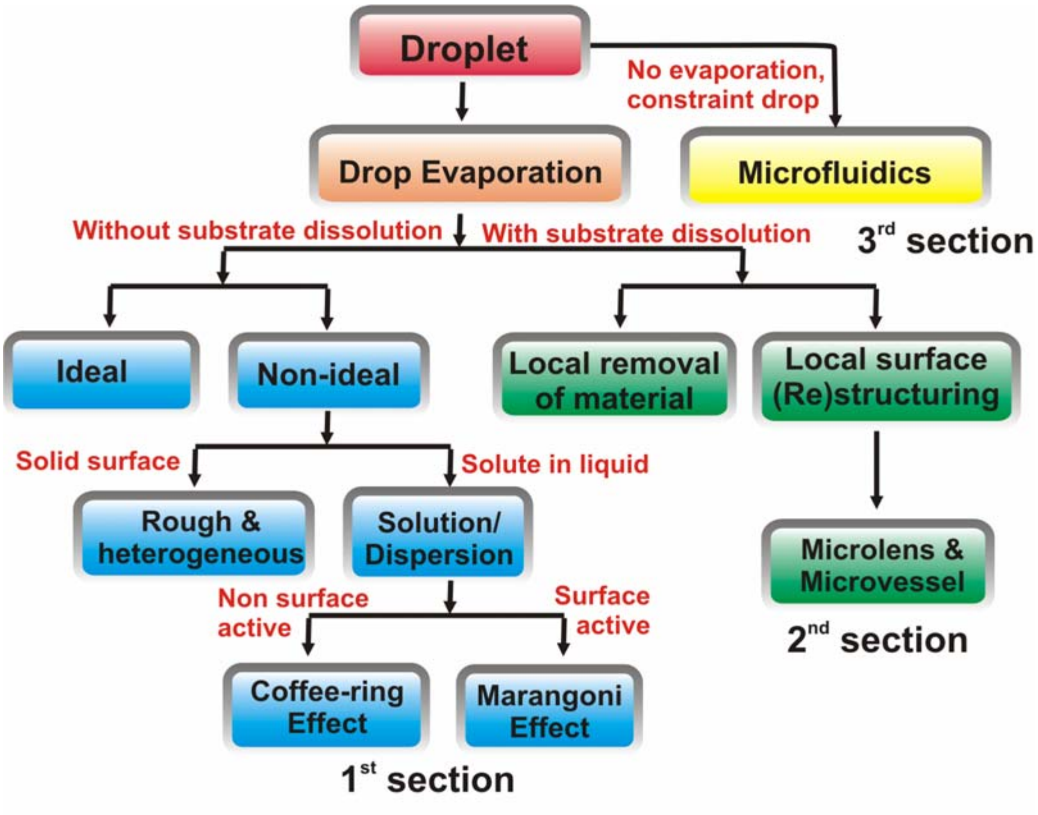

Figure 1 *Sketch of studies of droplets*

In the first section, basically there is no dissolution process occurring during the drop evaporation. They are commonly encountered in the so called ideal or non-ideal liquid/solid systems. In an ideal system, the selected liquid is normally a pure solvent (often water) and the solid surface is smooth and homogenous. The early theoretical studies on evaporation dynamics are mainly developed based on simple situations by collecting detailed information about the evaporation mode, the evaporation rate, or the flow velocity etc.[11, 12]. The evaporation dynamics can occurs in three basic evaporation modes. Either the contact angle, or the contact radius as constant (constant contact angle ≡ CCA mode or constant contact angle mode ≡ CCR mode, respectively) or a mixed mode containing both cases is observed[10].

The evaporation dynamic and the contact angle hysteresis are affected by the hydrophilicity of the surface. The higher the hydrophilicity of the surface is, the smaller becomes the static contact angle, the more pins the droplet on the solid surface, the higher is the hysteresis of the contact angle. Pinning leads to an increased ratio of surface to volume and thus a faster evaporation rate. Other surface properties as chemical composition, heterogeneity or roughness also give rise to the hysteresis and usually all these properties are coupled in a real system. To systematically study the contribution of each of these properties to the evaporation dynamics, the contact angle hysteresis, the hydrophilicity and heterogeneity must be decoupled from the surface roughness. Therefore, a model system, one of which the surface properties can be varied to our demand, is required.

In the first part of this thesis I concern about how surface properties as hydrophilicity and heterogeneity influence the dynamics of sessile drop evaporation. As a model system, I studied the evaporation of pure water drops, on self-assembled monolayers (SAMs) on mica covered with gold. The surface hydrophilicity and heterogeneity were separately adjusted by chemisorption of pure alkane thiolates (thiols) or dialkyl disufides, containing functional groups with different polarity at the end of the alkyl chains (non-polar methyl group versus polar hydroxyl group). Additionally, the length of the individual alkyl chains in the disulfide can be varied, providing a hairy surface. Thus the use of disulfides instead of the common thiols mixture[13-15] ensure that de-mixing effects can be neglected. Moreover, the use of mica as a support for the gold layer provides a low surface roughness. Thus, a smooth surface is obtained and the hydrophilicity and the heterogeneity are decoupled from the surface roughness. The evaporation dynamics is studied in dependence of the surface hydrophilicity and for a 1:1 mixture of methyl-and hydroxyl-terminated alkyl chains, in dependence of the length of the individual alkyl chains. For this, the evaporation mode and especially the transition between them, the evaporation time for different initial volumes of the droplets, and the drop size are measured with a self-made optical microscope. This was optimized for the measurement and analysis of spherical microdrops, for which an influence from gravitation can be neglected.

In non-ideal behavior, i.e. pinning is imposed into drop evaporation by dissolved molecules. Typical solutes are particles[16-18], polymers [8, 19-27], protein[28], DNA [3, 11, 29, 30]or surfactants/detergent [27, 31, 32]. Usually, if a drop of solution is evaporating, the solute is accumulated at the rim of the droplet and thus leaves behind a circular rim on the substrate after the drop evaporation. This is an everyday life phenomenon known from the evaporation of coffee drops and therefore is called coffee stain effect[33]. When the liquid contains a surface active component such as a detergent, the surface tension within the surface of the drop can additionally change, which might lead to Bernard convective cell owing to a Marangoni effect[27]. The drop evaporation becomes even more complex if polymers are used as solutes. M. Doi, U. Schubert and L. Pauchard individually predicted and found deviation from the ring structure[23, 24, 34]. For larger initial concentration (Mw. 282 kDa) in the sessile evaporation drop, the polymer piles-up in the center of the drop instead of forming a ring-like structure[24, 35]. This pilling was discussed as influenced by several intrinsic material properties or external process parameters, such as glass transition temperature[25], concentration[34], humidity[26], and initial contact angle[23]. All these examples show that drop evaporation can lead to different types of structuring within the surface, depending on the system under investigation.

In the second section (in green), dissolution process of substrate by solvent is embedded. The dissolution occurs during the evaporation process. This is a completely different case comparing the polymer solution prepared before drop evaporation. For a better understanding of the formation of microstructures of polymers initiated by evaporating solvent drops, in the second part of this thesis I study the evaporation of pure sessile solvent drops on polymer substrates, which starts to dissolve substrate locally after drop deposition. After evaporation a concave surface topology is left. This was first observed by R. H. Friend et al., who used this technique to remove a polymer from an electrode to vertically contact it with polymer transistor circuits[36]. Recently, this method was utilized in producing microstructures as microlenses and -vessels[37,38] in an one-step procedure[39, 40]. In this work, I study the influence of external process parameters and intrinsic material properties on the formation of microstructures. For an optimized decoupling of these two types of parameters, a syringe system was constructed, with which polar or apolar liquids can be (i) pumped with controlled velocity, and (ii) deposited in a controlled way. The evaporation of the droplet can be visualized simultaneously from the side to provide evaporation parameters as the contact angle and the droplet height. As external process parameters, the dependence of the microstructuring on the approach and retraction speed between drop and polymer substrate, and the duration of the contact between syringe tip and polymer was studied. For the influence of intrinsic material parameters on the microstructuring, the dependence on the polymer molar mass and the solvent/polymer system were studied as well. The contribution to the microstructuring from the coffee-ring effect, the Marangoni effect and the dissolution of polymer into the droplets are discussed.

So far the evaporation of droplets on a planar solid surface was studied. When the droplet is confined to a capillary or a channel, as shown in **Figure 2**, the surface properties become more and more important due to the increased ratio of surface to volume. The evaporation can be stopped or reduced. This leads to microfluidics.

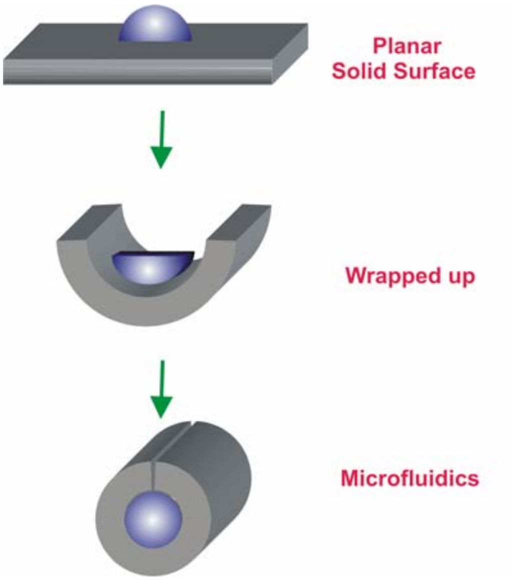

***Figure 2** Illustration for the transition from droplet evaporation on planar solid surface to a confined droplet as used in microfluidics*

Microfluidics systems are especially useful, when a small amount of analytes are required [41-44]. Thus they can be applied for providing spatial information or as an analysis tool for separation or analysis of biological or pharmaceutical samples[45, 46]. Principally, microfluidics can be performed digitally or continuously in one or more phases. If only one phase is present, a liquid can be transferred continuously through channels to reaction chambers. Or a separation in microanalytic systems is performed, leading to well-separated digital zones. Two or more phases can e.g. be realized by using immiscible liquid slugs in a microchannel. Naturally, this procedure is digital, the zones and any solute there can be well separated. Microfluidic devices may contain chemical synthesis steps between immiscible liquids as a precondition for the analyst to be transformed into an appropriate substance[5, 47]. There, the reaction takes place at the interface between the two liquids. The interfacial tension may possibly be affected with the progress of the reaction. A change of the interfacial tension might lead to an increase or decrease of interfacial area resulting in a better or worse reaction yield. In other systems, however, a constant interfacial tension is desired for the reason of proper processing[48, 49]. This also holds for the solid-liquid interface between liquid phase and channel walls. Usually, adsorption of dissolved chemicals to the channel walls of the micro-fluidic system must be avoided, although the surface properties inside the channel may differ. In this case, a change of interfacial tension indicates such an undesired adsorption. In this thesis, a new technique was developed for the purpose of an online measurement of the interfacial tension between two immiscible liquid slugs as they appear in digital microfluidic system. This technique is demonstrated for standard solvents, as hexane, toluene, and cholorform in contact with water slugs and was accepted as a patent.

2 FUNDAMENTAL

2.1 Sessile droplets

2.1.1 Young's equation for sessile droplets

Contact angle, as an important evaluation criterion, can be used to describe the surface properties, i.e. hydrohilicity of surface. The most common method of measuring contact angle is a sessile droplet method with a goniometer or a video recording system. The contact angle can be then directly measured or calculated with other measured parameters. Contact angle is the angle between liquid and solid by drawing a tangent at the edge of three phase line which is between solid, liquid and vapor. Such contact angle reading is taken at equilibrium, or strictly to say in quasi-equilibrium. Therefore a static contact angle is reached. In equilibrium, there are three forces acting on the edge of a sessile liquid drop to keep it still, shown in **Figure 3**.

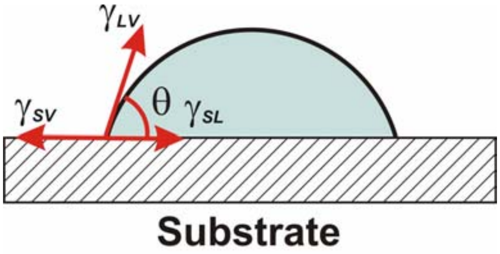

Figure 3 *Three forces acting on a liquid drop*

These forces are acting along the three interfaces between the solid, liquid and vapor phases, and commonly measured as corresponding surface tensions at the solid-liquid, solid-vapor, and the liquid-liquid vapor interface. In the equilibrium they are related to the contact angle θ_{eq} by the Young's equation and this equation is based on the equilibrium thermodynamics of a ideal system under the assumption of (i) the solid surface is flat and inert, (ii) the three interfacial tensions are constant, (iii) the gravity and line tension can be neglected.

$$\gamma_{LV} \cdot \cos\theta = \gamma_{SL} - \gamma_{SV} \qquad \text{Eq. 1}$$

Hereby γ_{SV} is solid- vapor interfacial tension, γ_{LV} is liquid- vapor interfacial tension and γ_{LS} is liquid- solid interfacial tension respectively, where θ is the contact angle of droplet.

The dynamic contact angle is used in probing a sessile droplet in motion which means three phase (liquid/solid/vapor) boundary is in actual motion. When droplet volume increases continuously by added more and more liquid, advancing contact angle is obtained, which is $\theta_{adv.}$ And when droplet starts to shrink, one gets receding contact angle θ_{Rec}. The difference between advancing contact angle and receding contact angle is defined as hysteresis, where $\theta_{adv} \geq \theta_e q \geq \theta_{Rec}$. Hysteresis provides information of solid surfaces such as roughness, contamination and chemical heterogeneity et al. Hysteresis can be also attributed to surface active impurities present in the liquid, swelling of the substrate and configuration of metastable states. In the present of the hysteresis, the solid surface becomes non-ideal.

Dynamic contact angles may be assayed at various rates of speed and thus can be used as well in describing evaporation dynamics. When dynamic contact angle is measured at a low velocity it should be equal to properly measured static angles. Static and dynamic contact angle provide a constant value in dependence of a given parameters as the surface hydrophilicity and speed of three phase line etc.

2.1.2 Evaporation dynamics of sessile drops

Evaporation of single sessile droplets provides contact angle as a function of time. This is a characteristic plot depending on surface properties i.e. surface hydrophilicity. Beside the influences from system itself, the contact angle can be also affected by the drop geometry when different drop size taken.

2.1.2.1. Spherical geometry

To distinguish a big drop from a small drop, a criterion can be applied. Generally a smaller droplet is defined when its radius is lower than 3.8 mm. This can be calculated according to the equation of $\kappa^{-1} = (2\gamma / \rho g)^{1/2}$[50]. κ^{-1} is capillary length, γ the surface tension, g the acceleration of gravity and ρ the density of the liquid. Larger drops become flatten owing to gravity and thus an elliptic geometry has to be adapted. Smaller droplet has always advantage in the investigation of evaporation dynamics of liquid since the shape of a small droplet can be considered as spherical. Based on the spherical geometry (**Figure 4)**, three basic parameters, namely, contact angle θ, contact radius a, and height of droplet h can be measured directly.

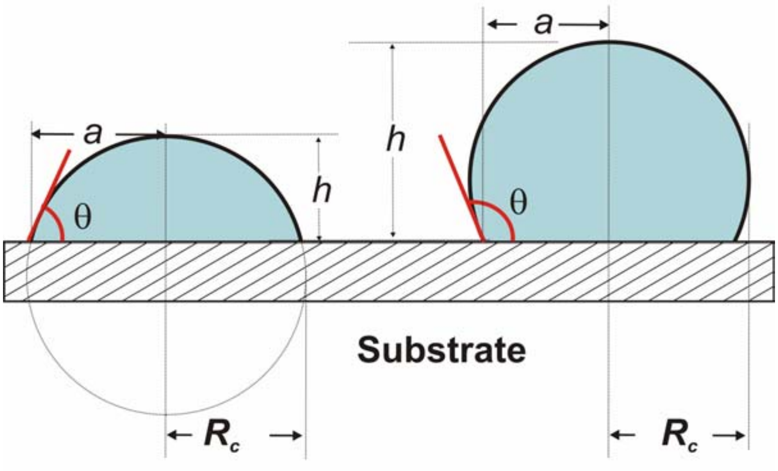

Figure 4 *Sessile drop geometry on both hydrophilic surface (left) and hydrophobic surface (right).*

Each can be expressed as a function of anther two parameters by a simple geometry, whereas, R_c is drop cap radius.

$$R_c = a / \sin\theta \qquad \text{Eq. 2}$$

$$h = R_c(1-\cos\theta) \qquad \text{Eq. 3}$$

$$\theta = 2\arctan(h/a) \qquad \text{Eq. 4}$$

With above equations, R_c, the volume V, drop cap area A_s, and surface area A_c can be derived by contact radius and drop height.

$$V = \pi h\left(3a^2 + h^2\right)/6 \qquad \text{Eq. 5}$$

$$R_c = \left(h^2 + a^2\right)/(2h) \qquad \text{Eq. 6}$$

$$A_s = \pi(a^2 + h^2) \qquad \text{Eq. 7}$$

$$A_c = \pi a^2 \qquad \text{Eq. 8}$$

2.1.2.2. Evaporation mode and evaporation rate of sessile drops

The evaporation of a sessile droplet occurs in three modes: constant contact angle mode (CCA), constant contact radius mode (CCR) and the mixed mode, shown in **Figure 5**.

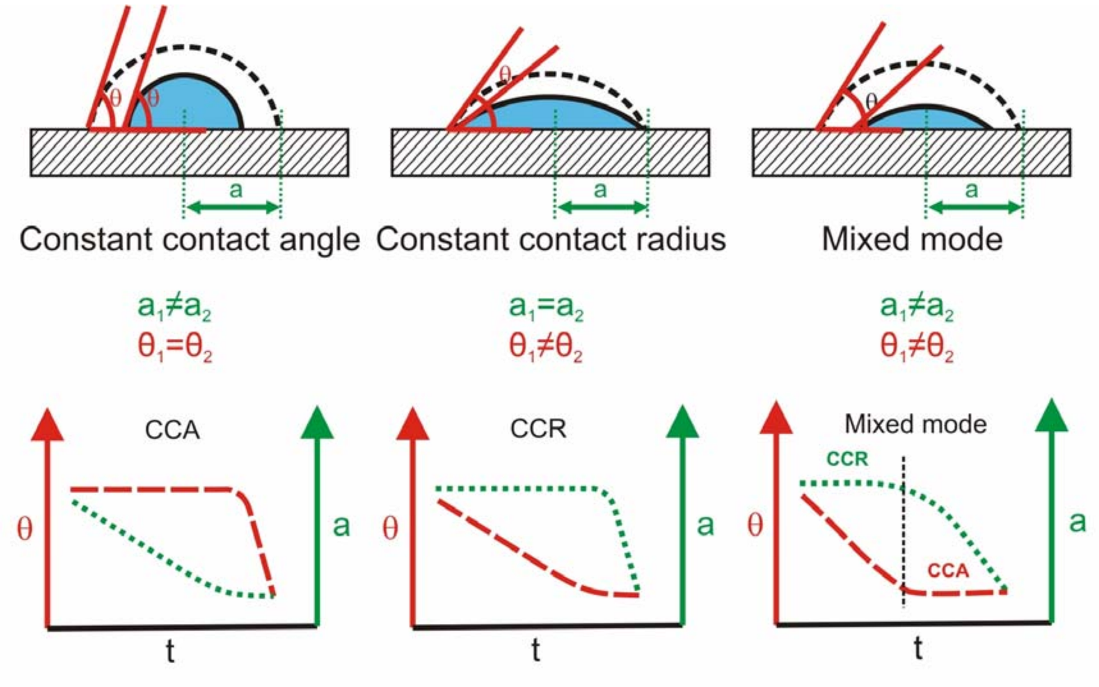

Figure 5 Three basic evaporation modes of droplet evaporation process and the correspondent plots of contact angle and contact radius versus time

The CCA mode is usually found in droplets with an initial contact angle larger than 90°[51] and the contact angle remain constant until the end of evaporation. The CCR mode is observed for an initial contact angles smaller than 40°, the contact radius keeps constant through the whole evaporation process, whereas the contact angle decreases. Between 90° and 40° often a transition from CCR to CCA is observed. The drop first evaporates with a pinned contact line, then becoming flatter during evaporation. After that the contact line starts to move and the contact radius decreases with a nearly constant contact angle. Generally a liquid droplet evaporates fast on hydrophilic surfaces since the CCR is favored. The area stays longer larger for a pinned drop. The plots of contact angle and contact radius as a function of evaporation time show how the evaporation mode looks like principally

(**Figure 5**). From this plots evaporation mode can be directly measured. The evaporation mode can reflect even slightly changed surface properties [10, 13, 14, 52-54].

During the evaporation process, all the other parameters i.e. drop volume, surface area and drop spherical cap area change accordingly. Physically the evaporation can be further described by an evaporation model based on the volume changes dV[10, 52, 54, 55]. The evaporation rate of a single sessile droplet can be described by [9,56]

$$-\left(\frac{dV}{dt}\right)=\frac{4\pi D}{\rho}\left(\frac{3V}{\pi\beta}\right)^{1/3}(C_s-C_\infty)f(\theta) \qquad \text{Eq. 9}$$

The evaporation rate is proportional to water concentration differences between drop surface and far away from drop and function of contact angle. C_s here is the water concentration at the spherical surface, and C_∞ is the water concentration at infinite distance. D is the diffusion coefficient of liquid and ρ is the liquid density. Both $f(\theta)$ and β are the function of contact angle of the spherical cap.

$$\beta=(1-\cos\theta)^2(2+\cos\theta) \qquad \text{Eq. 10}$$

Picknett & Bexon, Rowan et al. and Shanahan et al. separately provide three different solutions for $f(\theta)$. Here we only introduced one expression of $f(\theta)$ derived by Picknett & Bexon. Picknett and Bexon developed $f(\theta)$ in power series by using the analogy between the diffusive flux and electrostatic potential. They converted the problem of determining the evaporation rate of a sessile drop to a problem of evaluating the capacitance of an isolated conducting body of the same size and shape as the drop as an equiconvex lens. It is related to the contact angle by applying Snow series. To facilitate an easier calculation, they provided two empirical polynomials fit between the capacitance factor and contact angle, and $f(\theta)$ changes under different range of contact angle.

For $0.175 \leq \theta \leq \pi$ ($10° \leq \theta < 180°$)

$$f(\theta)=1/2(0.00008957+0.6333\theta+0.116\theta^2-0.08878\theta^3+0.01033\theta^4) \qquad \text{Eq. 11}$$

Assuming we are dealing with an ideal gas in this case, then combing $PV=nRT$, with equation of solution concentration, expressed by molar mass of the liquid M, solution volume V, $C = n \cdot M / V$, the concentration in **Eq. 9** can be replaced with vapor pressure. Given the drop as a full spherical drop[57], the evaporation rate can be expressed as

$$-\frac{dV}{dt} = 2\pi D \cdot R_c \cdot f(\theta) \cdot \frac{P_0 M}{\rho R T} \qquad \text{Eq. 12}$$

Whereas R is gas constant, P_0 is the vapor pressure of a liquid, T the temperature. ρ is the liquid density. If the contact angles are in the range of 39°~100°, $f(\theta)/\beta^{1/3}$ has a nearly constant value of 0.4. Provide that the diffusion of molecules in the gas phase is rate limiting, that a steady state is reached at each stage of evaporation. Assume that the temperature and the diffusion coefficient are constant and that the vapor pressure of the liquid far away from the drop is zero.[10] **Eq.12** can be integrated analytically as:

$$V^{2/3} = V_0^{2/3} - \frac{8}{3}\pi\left(\frac{3}{\pi}\right)^{1/3} \cdot D \cdot \frac{P_0 M}{RT} \cdot \frac{f(\theta)}{\rho\beta^{1/3}} \cdot t \qquad \text{Eq. 13}$$

Here, V_0 is the initial volume of the drop. When $V^{2/3}$ is plotted versus evaporation time t in a single droplet, a linearly fitting can be obtained[10, 52, 54, 58]. Such linearity of plot $V\sim t^{1.5}$ in single drop evaporation is widely found for different surfaces. It apparently indicates the plot is irrelevant to the surface properties [14]. Thus a standard equation containing constants of K_1 and K_2 is derived,

$$V^{2/3} = K_1 + K_2 t \qquad \text{Eq. 14}$$

For $t = 0$, K_1 becomes $V_0^{2/3}$ with V_0 initial drop volume, for $t = t_{tot}$, the total evaporation time, V equals to zero, thus K_2 is given as

$$K_2 = -V_0^{2/3} / t_{tot} \qquad \text{Eq. 15}$$

By replacing K_1 and K_2 into **Eq. 14**,

$$V = V_0 * (1 - t / t_{tot})^{3/2} \qquad \text{Eq. 16}$$

Such the linearity was recently reconfirmed by applying water droplets on a few SAMs surfaces, although apparent divergence at the end of curve is clearly shown especially on hydrophilic SAM surface. Given that 2/3 is not accurate enough to show such smaller changes, I would better to take 1/b inserting into the **Eq.16,** instead of 2/3. Hence a new equation is resulted.

$$V = V_0 * (1 - t / t_{tot})^b \qquad \text{Eq. 17}$$

In this work, the measurement of evaporation dynamics on a series SAM's surfaces, prepared from dialkyldisulfate or alkylthiols with different end group, hydrophilicity and/or alkyl chain length is carried out. The influences on the evaporation dynamics are studied. In contrast to the other studies[13], where the surface roughness also dominates evaporation dynamics, in this wok the roughness is decoupled from the surface hydrophilicity. Thus the influence of surface roughness can be ignored, an ideal SAMs surfaces are obtained.

2.1.3 Coffee ring effect and Marangoni effect

In an evaporation sessile droplets, many effects like Marangoni instability, coffee ring effect, Rayleigh-Bernard convection, buckling instability, crust effect and contact line pinning-unpinning account for the microstructure formation during the evaporation process[20, 24, 26, 40]. In this section I will introduce how the mechanism of such effects is responsible of driving the liquid moving inside of droplet. As being most concerned effects, coffee ring effect and Marangoni effect will be elucidated individually.

Coffee ring effect is caused by pinned contact line of drying droplet (**Figure 6**). Due to the fast evaporation rate at the rim, a certain volume of liquid is removed by the evaporation in a small time scale. In order to compensate the reduced volume (orange area), the liquid is transferred from interior drop toward the drop periphery by an outward flow (red arrows inside drop). This eventually gives rise to a ring formation. The phenomena is driven by so called capillary flow and it can be easily found in the dry process of dispersion containing either particles or solute as long as the substrate itself is partial wetting and solvent is volatile. Traditional mechanism as Marangoni effect, Rayleigh-Bernard convection, wetting phenomena and diffusion etc. do not account for the ring formation. Ring formation is a potentially important process which influences the printing, coating processes.

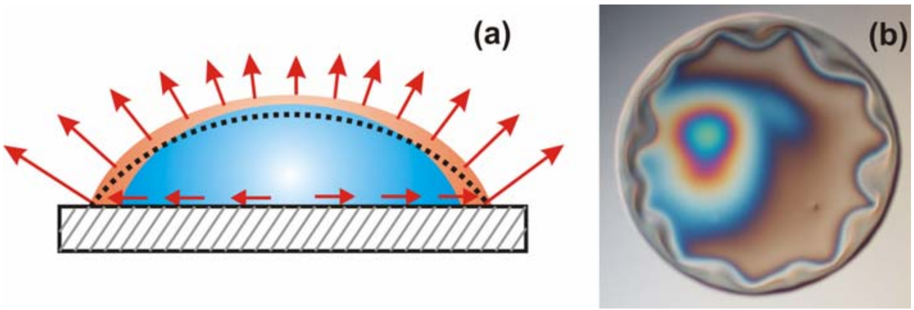

Figure 6 *A cross section of the ring formation mechanism in a droplet due to coffee ring effect (a), and a top view of ring formation by deposition of droplet (0.1 wt% polystyrene in toluene) on silicon surface (b).*

The pinned three phase line can arise from solute precipitation on a non-soluble substrate after a drop, containing either polymer material or particles, is detached onto substrate surface. It can be also resulted by an immediate material dissolution and following precipitation, when a solvent drop is deposited on a soluble material surface. The mass balance dictates a radial solvent flow toward the periphery to replenish the evaporative losses.

The velocity of the radial flow to the outer rim of the drop can be calculated by assuming a circular cross-section and rotation symmetry of the sessile drop, i.e. for small drops, which are governed by surface tension and not by gravity. A theoretical model based on axis-symmetric drop is applied in the solute transferring process in the drop evaporation for predicting the ring-like deposition of solute (**Figure 7**).

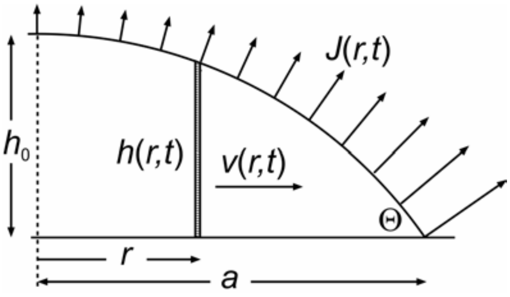

Figure 7 *Schematic diagram of the solute transfer in a sessile drop. The assumption is made on the droplet being axis-symmetric.*

Here the velocity of the flow of the liquid is assumed as laminar and the conservation of the liquid mass can be expressed in radical coordinates[59]:

$$\rho\frac{\partial h}{\partial t}=-\rho\frac{1}{r}\frac{\partial}{\partial r}(rhv)-J(r,t)\sqrt{1+\left(\frac{\partial h}{\partial r}\right)^2} \qquad \text{Eq. 18}$$

v is the vertically averaged radial flow of the liquid, ρ is the density of the liquid, r is the radial distance of the air-liquid interface from the droplet center, t is the evaporation time, h is the position of the air-liquid interface above the substrate surface, J is the evaporation flux from the surface of the drop (in kg·m^{-2}·s^{-1}). h_0 and a are the initial height and radius. The $\partial h/\partial r$ term is rather small and it is kept here for completeness. Thus, **Eq. 18** can be integrated, providing

$$v = -\frac{1}{\rho r h}\int_0^r dr r\left(\rho\frac{\partial h}{\partial t} + J(r,t)\sqrt{1+\left(\frac{\partial h}{\partial r}\right)^2}\right) \qquad \text{Eq. 19}$$

The drop is assumed as hemispherical, thus the height profile can be expressed as:

$$h(r,t) = \sqrt{\left(h_0^2 + a^2\right)^2 / (2h_0)^2 - r^2} - \left(a^2 - h_0^2\right)/2h_0 \qquad \text{Eq. 20}$$

The evaporation flux is given by $J \approx f(\lambda) J_0 \left[1-(r/a)^2\right]^{-\lambda}$ with $\lambda = (\pi - 2\theta)/(2\pi - 2\theta)$, which is a good approximation for the enhanced evaporation through whole drop surface. J_0 is the evaporation rate for $\lambda = 0$. Whereas the parameters of h_0, a, ρ are known, h, r, t are the value at the assigned moment. For a small contact angle and pinned droplet, integration of Eq. 19 provides [60]

$$\begin{aligned} v = &-\frac{1}{2rhh_0^2}\frac{\partial h_0}{\partial t}\cdot\left[\frac{r^2}{2}\left(h_0^2 - a^2\right) - \frac{1}{12h_0^2}\left\{\left(h_0^2 + a^2\right)^2 - 4r^2h_0^2\right\}^{3/2} + \frac{\left(h_0^2 + a^2\right)^3}{12h_0^2}\right] \\ &+ \frac{2\lambda a^2 J_0}{\rho r h}\cdot\left[1 - \left\{1 - (r/a)^2\right\}^{\lambda}\right] \end{aligned} \qquad \text{Eq. 21}$$

This model developed for a radial, height averaged velocity distribution in an evaporation droplet and the observed the ring formation of a solute after evaporation[33, 59] is successfully in explaining qualitatively the formed drying structure[61]. Beside coffee ring effect, for a quantitative description of coffee ring formation, the Marangoni effect has to be included as well, which is virtually reverse to the coffee ring deposition[62].

Marangoni effect is in principal a mass transfer driven by gradient changed surface tension inside of the liquid (**Figure 8**).

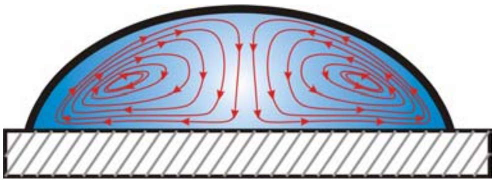

Figure 8 *A cross section view of the Marangoni effect in a droplet*

Since the liquid with higher surface tension tends to pull the surrounding liquid with lower surface tension toward itself, thus a flow convection is resulted. Marangoni effect normally occurs in a liquid-gas or a liquid-liquid system and arises from local variation of the interfacial tension, which is caused by a gradient of temperature or concentration[63]. In the case of concentration gradients, the effect is called the solutal Marangoni effect. When temperature gradients result the Marangoni effect, the effect is frequently named as thermocapillarity, since in the evaporation process of a liquid drop, the evaporation rate at the rim is faster than that in the center. An evaporation cooling effect is induced in the drop. This results a temperature gradient from center to rim. Apart from this temperature gradient, a concentration gradient inside the drop occurs if a solution is present. Usually, the concentration of the solutes influences the surface tension of the liquid surface. Therefore, an additional surface tension gradient might occur.

Marangoni effect is found to be rather weak in the pure water droplets[59, 62]. In contrary it becomes significantly when the evaporation process of a volatile organic solvent drop is taken into consideration. Since the evaporation induced non-uniform cooling along the drop surface, a temperature gradient occurs and leads to surface tension gradient. The Marangoni effect arising from latent heat of evaporation carries the materials from free liquid surface inward toward top of drop, and then plunges into the center of drop and finally to the edge. This effect leads to redistribution of the solute in the droplet.

Subsequently a full analytical solution combining a lubrication theory with a finite element method (FEM) is introduced, which can be used for expressing a full asymmetric velocity field in the evaporating droplets with pinned contact lines[30, 62]. The Marangoni effect is considered quantitatively into both vertical and radical evaporation flux equations in **Eq. 22** and **Eq. 23**.

$$\begin{aligned}
v_r = {} & \frac{3}{8}\frac{1}{1-\tilde{t}}\frac{1}{\tilde{r}}\Big[\big(1-\tilde{r}^2\big)-\big(1-\tilde{r}^2\big)^{\lambda(\theta)}\Big]\left(\frac{\tilde{z}^2}{\tilde{h}^2}-2\frac{\tilde{z}}{\tilde{h}}\right)+ \\
& \left\{\frac{\tilde{r}{h_0}^2\tilde{h}}{a^2}\Big(\tilde{J}\lambda(\theta)\big(1-\tilde{r}^2\big)^{-\lambda(\theta)-1}+1\Big)\left(\frac{\tilde{z}}{\tilde{h}}-\frac{3}{2}\frac{\tilde{z}^2}{\tilde{h}^2}\right)\right\}+ \\
& \frac{Mah_0\tilde{h}}{2R}\Big(ab\tilde{r}^{b-1}+2(1-a)\tilde{r}\Big)\left(\frac{\tilde{z}}{\tilde{h}}-\frac{3}{2}\frac{\tilde{z}^2}{\tilde{h}^2}\right)
\end{aligned}$$

Eq. 22

$$\begin{aligned}
v_z = {} & \frac{3}{4}\frac{1}{1-\tilde{t}}\Big[1+\lambda(\theta)\big(1-\tilde{r}^2\big)^{-\lambda(\theta)-1}\Big]\left(\frac{\tilde{z}^3}{3\tilde{h}^2}-\frac{\tilde{z}^2}{\tilde{h}}\right)+ \\
& \frac{3}{2}\frac{1}{1-\tilde{t}}\Big[\big(1-\tilde{r}^2\big)-\big(1-\tilde{r}^2\big)^{-\lambda(\theta)}\Big]\left(\frac{\tilde{z}^2}{2\tilde{h}^2}-\frac{\tilde{z}^3}{3\tilde{h}^3}\right)\tilde{h}\big(0,\tilde{t}\big)- \\
& \Bigg\{\frac{{h_0}^2}{a^2}\Big(\tilde{J}\lambda(\theta)\big(1-\tilde{r}^2\big)^{-\lambda(\theta)-1}+1\Big)\left(\tilde{z}^2-\frac{\tilde{z}^3}{\tilde{h}}\right)+\frac{\tilde{r}{h_0}^2}{a^2}\tilde{J}\lambda(\theta)\big(\lambda(\theta)+1\big)\big(1-\tilde{r}^2\big)^{-\lambda(\theta)-2}\left(\tilde{z}^2-\frac{\tilde{z}^3}{\tilde{h}}\right)- \\
& \frac{\tilde{r}{h_0}^2}{a^2}\Big(\tilde{J}\lambda(\theta)\big(1-\tilde{r}^2\big)^{-\lambda(\theta)-1}+1\Big)\left(\frac{\tilde{z}^3}{\tilde{h}^2}\right)\tilde{h}\big(0,\tilde{t}\big)\Bigg\}- \\
& \frac{Mah_0}{4R}\Big(ab^2\tilde{r}^{b-2}+4(1-a)\tilde{r}\Big)\left(\tilde{z}^2-\frac{\tilde{z}^3}{\tilde{h}}\right)+\frac{Mah_0}{2R}\Big(ab\tilde{r}^{b}+2(1-a)\tilde{r}^2\Big)\left(\frac{\tilde{z}^3}{\tilde{h}^2}\right)\tilde{h}\big(0,\tilde{t}\big)
\end{aligned}$$

Eq. 23

Here v_r represents the local radical velocity and v_z the vertical velocity, respectively. $v_r = v_r t_f / a$, $\tilde{t} = t / t_f$, $\tilde{r} = r / a$, $\tilde{z} = z / h_0$, $\tilde{h} = h / h_0$, t_f is the drying time and $h\big((r,t\big) = h\big(0,\tilde{t}\big)\big(1-\tilde{r}^2\big)$. **A**nd the Marangoni number is defined as $Ma \equiv -\beta\ (T_e-T_c)-t_f/\mu R$, with β the surface tension-temperature coefficient, and μ is the viscosity of the liquid. T_e is the surface temperature at the edge of the droplet, and T_c the surface temperature at the top of the droplet.

2.2 Polymer dissolution behavior of polymer

When dealing with drop evaporation on a soluble polymer substrate, the dissolution of the polymer material must be considered. In this case, beside the coffee ring effect and

Marangoni effect, the understanding of polymer dissolution process becomes important. In this chapter, the basic dissolution behavior of polymer will be introduced.

2.2.1 Processes in sessile evaporating solvent droplets on a polymer surface

The new aspect in this thesis is that the polymer dissolution process during the evaporation is different from the previous studies, which considered only pre-prepared polymer solution[25, 36]. To better understand the experimental results, simulation were performed in Prof. W. Wiechert group, in University Siegen[64, 65]. Therefore a briefly description will be given here.

The evaporation process of droplets containing either particles or polymers is quite complex[66-69], many physical processes are involved, like mass transfer, solvent diffusion, gelation, skinning formation, dissolution, surface tension effect, instability, pinning-depinning (**Figure 9**). After drop deposition usually pinning of the three-phase line is observed. During the evaporation polymer is dissolved into the solvent. Owing to a flow toward the rim of the droplet, the dissolved polymer accumulates at the rim and forms a gel.

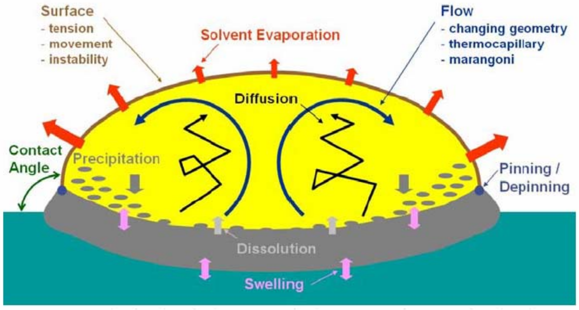

Figure 9 *Different processes occurring during a sessile toluene droplet evaporating on a PS surface*[65]

In the following, the theoretical background for the different processes involved in drop evaporation is presented.

2.2.2 Mechanism of polymer dissolution

As polymer dissolution process in solvent is equivalent with it in solvent drop. In this chapter the mechanism of polymer dissolution in solvent will be introduced and later it will be used to give an explanation on the solvent drop evaporating on the soluble polymer surface.

Basically polymer dissolution process occurs when solvent directly contacts with soluble polymer surface and they are affected by many parameters, such as size of solvent molecules, kind of solvent, molar mass of polymers, polydispersity, tacticity of polymer, temperature etc[70, 71]. Two types of dissolution are discussed: a normal dissolution and a non-normal dissolution. In normal dissolution, an amorphous, non cross-linked polymer is immersed into a good solvent. The solvent enters the free space inside of the polymer matrix and a multi-layer forms which shows in the sequence of pure polymer, infiltration layer, solid-swollen layer, gel layer, liquid layer and pure solvent (**Figure 10**). The infiltration layer and swollen layer are in glass state, whereas the gel layer is in rubbery-like state. The formation of these layers occurs owing to the solvent penetration into free channel and holes in the glassy state polymer. Thus the polymer swells with increasing solvent concentration. The swollen material is pushed out into solvent, which in turn helps the entangled polymer chains to disentangle. Therefore in normal dissolution a gel-like layer is present between a pure polymer and a pure solvent phase, whereas in non-normal dissolution, the gel lay disappear. For a certain system, the normal dissolution process can be tuned into non-normal polymer by lowering the experimental temperature. The gel layer becomes thinner and thinner and vanishes when the temperature reaches a certain value.

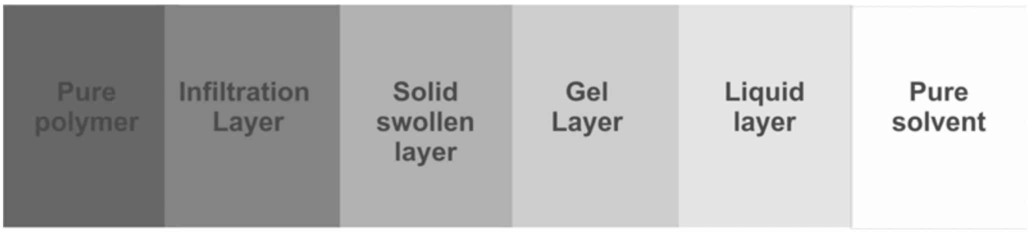

Figure 10 *Schematic picture of polymer surface layers during dissolution process in a solvent*[70].

In principle, two transport processes occur during the dissolution of a polymer into a solvent, the solvent diffusion into the polymer and a disentanglement of the polymer chains. The solvent has the tendency to penetrate the polymer matrix whereas the entangled polymer chain is solvated and swell when the polymer dissolution rate is comparable low. The swelling proceeds until a quasi-stationary state is reached. After that the swollen polymer will be separated from glassy polymer through dissolution process into the solvent (**Figure 11**).

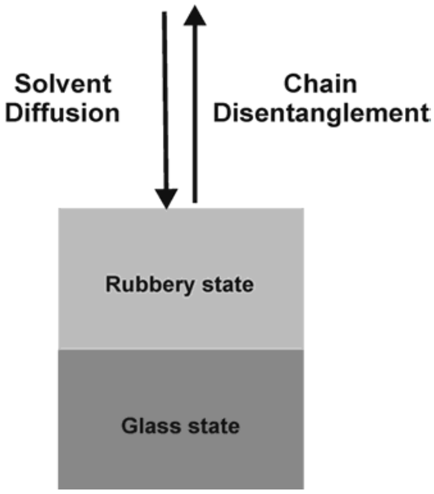

Figure 11 *Scheme of one-dimensional solvent diffusion and chain disentanglement during polymer dissolution process*[70, 72, 73].

Dynamically, there are two temporary processes, which can be distinguished. A transition from glass state to rubbery state can be observed as an intermediate swelling layer forms between them. The swelling layer is in glass-rubbery state and the gel-like layer in rubbery state (**Figure 12**).

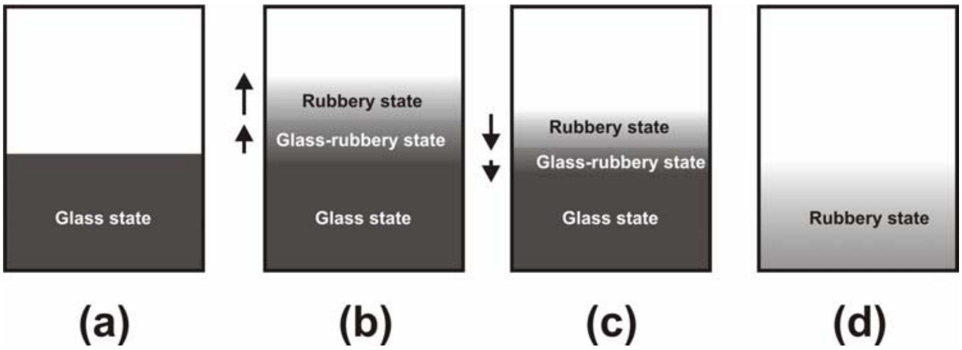

Figure 12 *Dynamic of polymer dissolution: swelling (a, b) and consecutive dissolution by disentanglement (c, d)* [70]

At the first stage, swelling dominates and both gel layer and the swelling layer becomes thicker and expands with time. And after a certain induction time, which is correspondent to the disentanglement of polymer chain, the actual dissolution occurs. Then these two layers start to move inward the polymer and swollen layer becomes thinner. After the swollen layer vanished, the rubbery state of the gel-like layer continuously moves until the dissolution is complete.

The dissolution rate is principally determined by the penetration rate and the disentanglement rate. It was found that the dissolution rate is governed by polymer molar mass[70]. For low molar mass polymer, the dissolution rate is limited by the penetration rate since dissolution is fast, i.e. the diffusion process of solvent into polymer is predominant. For high molar mass the dissolution rate is dominated by the disentanglement rate[72]. Polymer with a larger molar mass has a higher degree of disentanglement, thus to less swelling and therefore to a slower disentanglement.

2.2.3 Dependence of polymer dissolution rate on disentanglement and solvent diffusion

Up to know it is quite clear that when a solvent drop is deposited on the polymer surface, the dissolution process occurs immediately, accompanying by a simultaneously evaporating process. The dissolution process is fast process comparing to the evaporation process and the concentration of polymer in solvent raises up continuously due to both effects. The polymer molecules at the final stage of the evaporation process dominate the mass transfer inside of drop and the formation of microstructure. In this chapter the molecules behavior changing with concentration will be pictured and a quantitative description of diffusion of molecule with different molar mass will be discussed.

When solvent molecules enter into the polymer surface, dissolution of polymer chain into solvent leads to concentration changes in the rubbery state in the gel-like layer, which is close to the solvent phase. Thus concentrated, semi-dilute and a dilute regime are formed[74] (**Figure 13).** In dilute regime, polymer chains distance between two polymer chains is larger than the radius of gyration, thus no interaction occurs. In the semi-dilute regime, polymer coils overlap, at the overlap concentration of C^*. The radius of gyration R_G and overlap concentration of polymer solution are correspondent to the polymer molar mass M_w and can be expressed as

$$\langle R_G \rangle = 1.38 \times 10^{-4} Mw^{1.19} \qquad \text{Eq. } 24^{75}$$

$$C^* = \frac{3Mw}{4\pi N_A (R_G)^3}$$ Eq. 25[75]

Here N_A is the Avogadro's number. The dissolution occurs when polymer chain disentangles, as described before. Thus an overlap concentration has to reach before a dissolved polymer is found as coil like in the solution.

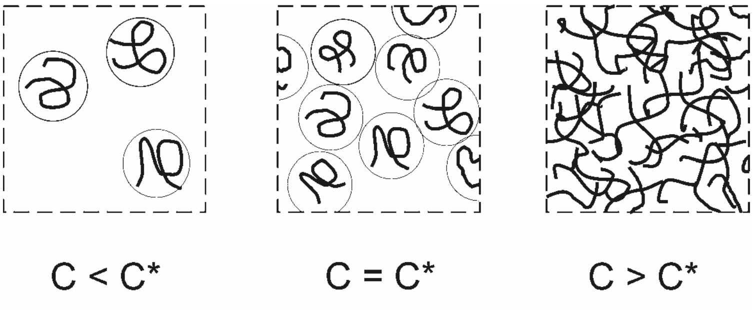

Figure 13 *Concentration regimes of polymer in a good solvent during dissolution. (a) dilute, (b) semi-dilute, (c)concentrated solution*[74].

From these equation, the self-diffusion coefficient *D* in dilute and semi-dilute solution can be calculated [76-78]. D_0 is the diffusion coefficient of solvent.

$$D = D_0 \cdot exp(-ac^u)$$ Eq. 26

$$D_0 = 2.8 \times 10^{-8} M_W^{-0.55} m^2 / s$$ Eq. 27

Both α and u are variables and are dependent of molar mass as $\alpha \propto M_w^{-1}$ and $u \propto M_w^{-1/4}$. u decreases linearly from 1.0 to 0.5, with the increasing polymer molar mass from 1 x 10^5 to 5 x 10^5 g/mol.

For the droplet evaporation, **Eq. 26** and **Eq. 27** enable us to estimate the total time for polymer dissolving in the solvent and reaching the overlap concentration by $<x>^2 = 6D/t$. Here, x is the diffusing distance and t is the diffusion time. The diffusion process is time dependent and can be quantified according to different diffusion kinetics.

The diffusion of solvent into a glassy polymer and the disentanglement of polymer in the actual dissolution step can be described by one phenomenological model, despite its different physical nature. The phenomenological model normally describes the dissolution process with Fickian condition and the moving boundaries in one system. The diffusion kinetic of solvent into polymer can be divided into three categories: Fickian (Case I) diffusion, non-Fickian (Case II) diffusion and anomalous diffusion[72, 79, 80]. Fickian law is valid for n = 0.5, Case II diffusion of n=1, and anomalous diffusion 0.5 < n < 1.

$$Z = At^n + Z_0 \qquad \text{Eq. 28}$$

Whereas Z is the one dimension distance of solvent penetration into polymer, Z_0 is the initial value, n is the exponent and t the diffusion time[79]. Fickian diffusion occurs at the very initial stage, where the diffusion rate is much lower than polymer disentangle rate[72, 81, 82], which is owing to mechanical, structural properties etc. The rate is limited by the diffusion of material from the surface of swollen polymer to solvent front and the ingress of solvent proceeds as the square root of time. Non-Fickian diffusion is rather rapid process comparing the disentangle process. The rate of ingress solvent is limited by a time-independent solvent front and it is linearly increasing with ingress time. The anomalous diffusion is a process, when both diffusion and disentangle rate are comparable. The rate is proportional to t^n, where n is between 0.5 and 1.

2.2.4 Instabilities during and after the evaporation process

As another major influence on the final shape of microstructure, the instability occurs either during the evaporation process of liquid leading a crust like structure (convex will be used later in this thesis, instead of crust), or after evaporation process leading cracks.

A mechanical instability induces pilling and bucking owing to the changes of liquid concentration and viscosity during the evaporation process[23, 35, 83]. Dynamically, the formation of the microstructures is mainly dominated by two effects during the drop evaporation (i) evaporation rate, (ii) coffee ring effect. These two effects are directly related to the solution viscosity and concentration. Several types of microstructures for instance, concave structure, Mexican hat like structure, dimple in the center and concave structure are observed after droplet evaporates (**Figure 14**). For low polymer concentration, less material is dissolved and thus gives rise to a fast evaporation rate. A concave structure will form due to the coffee ring effect. For the intermediate polymer concentration, the structure is formed as either a shape of Mexican-hat like or a dimple in center, since the coffee ring effect is competed with the evaporation rate during the evaporation. However, for the high polymer concentration, coffee ring effect become weak and evaporation rate becomes extremely lower due to increasing concentration and viscosity. Thus a convex structure can be resulted.

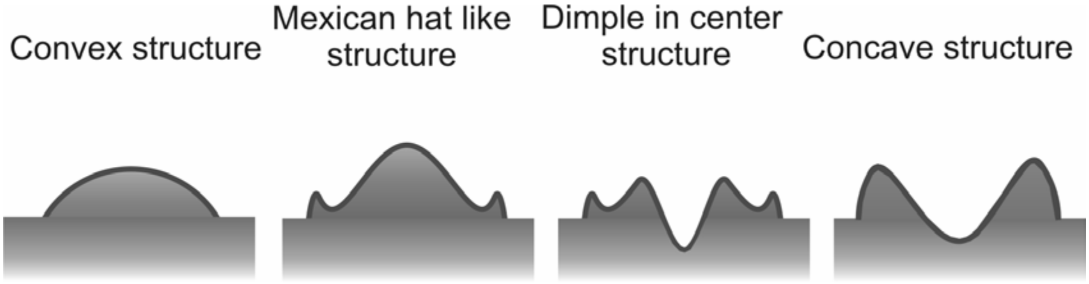

Figure 14 *Several types of microstructure formed by droplet deposition processes*

From another point of view, the mechanical properties of bending energy and stretching energy inside of polymer layers formed during droplet evaporation are found to be the reason for the piling of polymer material in the center of structures[26]. During droplet evaporation, the outer droplet surface becomes polymer-rich and a glassy skin forms. The evaporation is slowing down because solvent molecules have to diffuse through the polymer skin. Due to the glass skin formation, a bulking instability is leading, which in turn affects the concentrated solution drop shape.

Cracks take place after evaporation process, in a so called desiccation process. Since during the evaporation process the internal pressure is built up faster than the glassy matrix can relax through gradual swelling, this freezing-in energy at the glass transition temperature inside of the elastic shell results the formation of these structures as convex, Mexican hat like, dimple in the center[73]. This eventually caused crack formation, in fact, helps to release this stress. Cracks occur quite often for the low molar mass polymer.

2.3 Determination of interfacial tension

When a droplet is confined in 3D microcapillary, evaporation is no more important comparing to the surface properties influences (described in Chapter 1). As one of important parameters, hydrophilicity should be considered in this case.

If two immiscible fluids are contact, an interface is formed due to the interaction between molecules of each two phases. This requires energy owing to the lower interaction energy of the molecules in the interface. Thus the system tries to minimize the interfacial area. The work/area needed to form this interface is called interface tension.

Several methods can be used to determine the interfacial tension between two immiscible liquids, the lens, spinning-drop, ring (du Noüy) and the Wilhelmy plate method. In the lens method, a drop of liquid B, having a smaller density than liquid A, is placed onto the liquid A surface (**Figure 15a**). These two liquids will not mix. With **Eq. 29** derived from Young' equation**,** the interfacial tension can be calculated**.**

$$\gamma_A \cos\theta_3 = \gamma_B \cos\theta_1 + \gamma_{AB} \cos\theta_2 \qquad \text{Eq. 29}$$

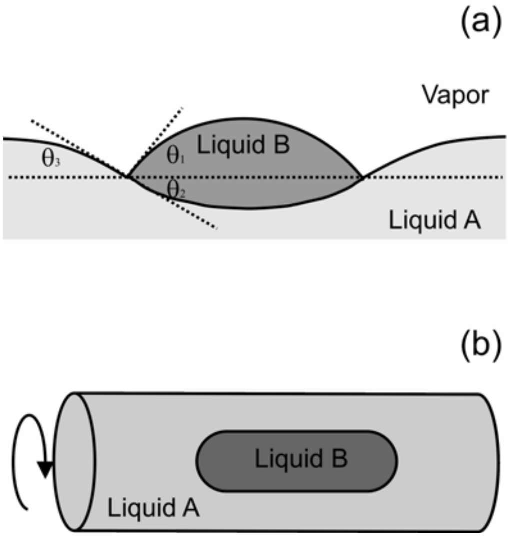

***Figure 15** Schematic descriptions of lens method and spinning drop method*

With γ_A, γ_B the surface tensions of the pure liquids and γ_{AB} the interfacial tension between liquid A and liquid B. θ_1, θ_2 and θ_3 represent the angles between the surfaces of liquid A and B and the interface of A in B on one hand and the dashed horizontal line on other hand, respectively. **Figure 15b** shows the principle of the spinning drop method. A liquid A with a higher density is filled into a horizontally placed capillary, and after that a drop of liquid B is injected into the center of the capillary. By rotating the capillary along the long axis, the liquid B forms a drop. Its shape is used to determine the interfacial tension.

Many literature values are obtained by du Noüy ring method (**Figure 16** left). In this method the wettability of the surface has little influence on the result, when the liquid is in contact with the ring and forms a liquid film. As a measurement starts, the ring is raised in order to contact with the registered liquid interface. The platinum iridium made ring is then lowered and the liquid film beneath the ring is stretched. The stretched film produces a maximum force F_{max} parallel to the direction of the ring movement and the contact angle approximately equals to zero. The force increases with the distance between the ring and the surface, and drop after F_{max}. The film breakage is avoided since the result is actually an average of many time measurements. Since the weight of the liquid F_v raised by ring is contained in the maximum force, it must be subtracted. According to

$$\gamma = \frac{F_{\max} - F_v}{L \cdot \cos\theta} \qquad \text{Eq. 30}$$

Here L is the circumference of ring.

The Wilhelmy plate method (**Figure 16** right) is a method suitable for surface tension and interfacial tension measurement over long time intervals.

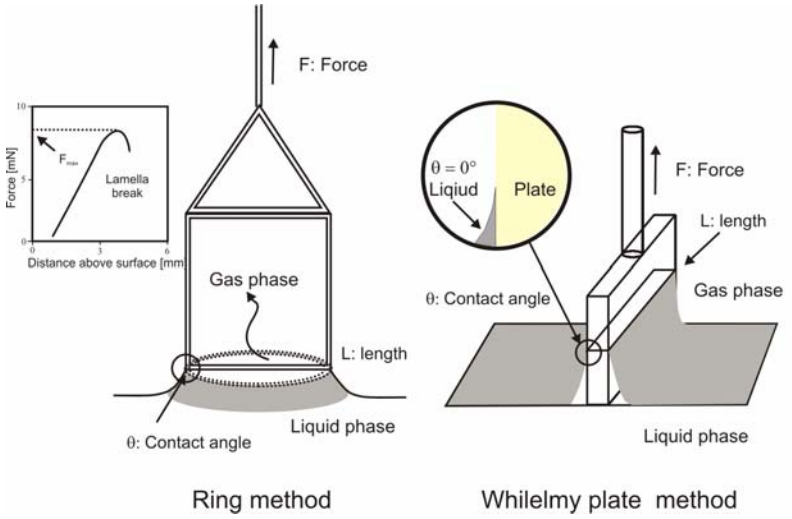

Figure 16 *Schematic description of du Noüy's ring method (left) and Wilhelmy plate method (right) for interfacial tension determination.*

The platinum plate surface is rough thus an optimized wetting is expected. The vertical plate with a known length L is attached to a balance. Due to wetting the force is measured. The liquid is raised until the contact between the surfaces or interface of liquid and the plate is registered. The contact angle becomes zero when the maximum force is reached providing a simplified equation for the measurement force exerted on the Wilhelmy plate.

$$\gamma = \frac{F}{L \cdot \cos\theta} \qquad \text{Eq. 31}$$

3 EXPERIMENTS

3.1 Chemical and Materials

3.1.1 Cleaning of glassware/substrates

The following chemicals were mainly used for the cleaning of glassware and the substrates. Glass apparatus such as syringe, beaker, Teflon tube, microcapillary etc. were cleaned in a solution of 5% Tickopur in ultrapure water in a supersonic bath for 15 minutes, and then rinsed with ultrapure water ten times for a crude removal of the detergent. Additionally, the glassware was supersonicated in a solution of 20% isopropanol in ultrapure water for 15 minutes to remove the residue of detergent. Finally, they were rinsed again with ultrapure water ten times and dried with a pure N_2 flow.

- Isopropanol, HPLC, Merck, Darmstadt, Germany
- Tickopur R33, detergent concentrated, Dr.H.Stamm GmbH, Berlin, Germany
- Ultra-pure water, 18.2 MΩ·cm, Arium 611 VF, Sartorius Germany (either for cleaning or for the droplet evaporation experiment)

For the experiment of droplet evaporation, exclusively ultra-pure water was used.

3.1.2 Self-assembled monolayer (SAMs)

3.1.2.1. Chemicals

The chemicals below were used for the preparation of SAMs on gold mica and polymer sample preparation.

- Methanol, HPLC, Merck, Darmstadt, Germany
- Dichloromethane, HPLC, Merck, Darmstadt, Germany
- Ethanol, HPLC, Sigma-Aldrich Chemie GmbH, Germany
- Dodecanethiol 98%, Merck, Darmstadt, Germany

- 11-mercapto-undecanol, 97%, Aldrich, Germany
- Gold 99.9%
- Chloroform, proanalysi, Merck, Darmstadt, Germany
- Hexane, proanalysi, Merck, Darmstadt, Germany

3.1.2.2. Synthesis of asymmetric dialkyl disulfides SAMs

In this thesis, the synthesis of asymmetric dialkyl disulfides was performed by Chandrasekhar Vavilala in the group of Prof. Michael Schmittel at University Siegen.

All reactions were carried out under nitrogen using freshly distilled anhydrous solvents. Diethyl ether and dichloromethane (DCM) used for synthesis were distilled from sodium/benzophenone and calcium hydride, respectively. Dodecanethiol (+98%, Merck) and 11-mercapto-undecanol (97%, Aldrich) were used as received. All disulfides used in this study were prepared according to a standard, two-step procedure[84]. In the first step, the corresponding alkylthiol RSH ($CH_3(CH_2)_{11+m}SH$)(1.0 eq) was treated with diethyl azodiacarboxylate (DEAD) (1.0 eq) in dry diethyl ether at room temperature for 3 days to furnish the diethyl N-alkanesulfenylhydrazodicarboxylate adduct (I).

$$\mathbf{RSH + C_2H_5O_2CN{=}NCO_2C_2H_5 \longrightarrow \underset{(I)}{C_2H_5O_2CNH{-}N(SR)CO_2C_2H_5}}$$

$$\mathbf{\underset{(I)}{C_2H_5O_2CNH{-}N(SR)CO_2C_2H_5} + OH(CH_2)_{11}SH \longrightarrow \underset{(II)}{OH(CH_2)_{11}SSR} + C_2H_5O_2CNH{-}NHCO_2C_2H_5}$$

In the second step, the hydrazodicarboxylate adduct (I) (1.0 eq) was treated with 11-mercapto-undecanol (1.0 eq) in DCM at reflux temperature for 2 days to provide the asymmetric disulfide (II). The resulting disulfide was purified by column chromatography using chloroform as the eluent. Further purification by plate-thin layer chromatography was occasionally performed before preparation of the solutions used for self-assembly.

R and m in the asymmetric disulfides are listed in table 1.

m	R
+6	$CH_3(CH_2)_{17}$-
+4	$CH_3(CH_2)_{15}$-
+2	$CH_3(CH_2)_{13}$-
0	$CH_3(CH_2)_{11}$-
-2	$CH_3(CH_2)_9$-
-4	$CH_3(CH_2)_7$-
-6	$CH_3(CH_2)_5$-

Table 1 *Asymmetric disulfides prepared via diethyl N- alkanesulfenylhydrazodicarboxylate*

3.1.2.3. Preparation of self assembled monolayer on gold-mica substrate

The preparation of SAMs on gold mica substrate surfaces was conducted by Dr. Susana Moreno Flores, polymer physics group in Max Plank Institute for Polymer Research.

Au (111) surfaces were prepared by thermal evaporation onto freshly cleaved, tempered mica. The mica was preheated at 650°C for 3 minutes under a nitrogen stream to prevent water condensation and contamination just prior to the gold evaporation. 60-70 nm of gold were deposited under a chamber pressure of $1\text{-}2\times10^{-6}$ mbar by thermal evaporation (Edwards FL400 model Auto 306, UK). Subsequently, surfaces were annealed at 650°C (Heraeus Instruments) for 1 minute under nitrogen gas. The treatment was preceeded/followed by a gradual increase/decrease of the sample temperature to/from the annealing temperature. Self-assembly was performed immediately after preparation of the gold substrates.

SAMs of with only one type of chain, i.e. dodecanethiol (DDT) and mercapto-undecanol (HUT) were prepared by immersion of gold-mica substrate in 1 mM ethanol solutions of the corresponding thiol for 12-24 hours. The samples were rinsed with pure ethanol and dried under filtered nitrogen. Asymmetric dialkyl disufites SAMs with different type of chains were obtained by immersing the gold-mica substrates in a 0.5-1 mM dichloromethane solution containing the corresponding disulfide for 24-48 hours. The samples were rinsed with pure dichloromethane and dried in air. For comparison, at least two samples were prepared for each kind of SAMs. It is performed by immersing two pieces of gold mica in the same solution but in different beakers. A sketch of prepared SAMs samples are shown in **Figure 17**.

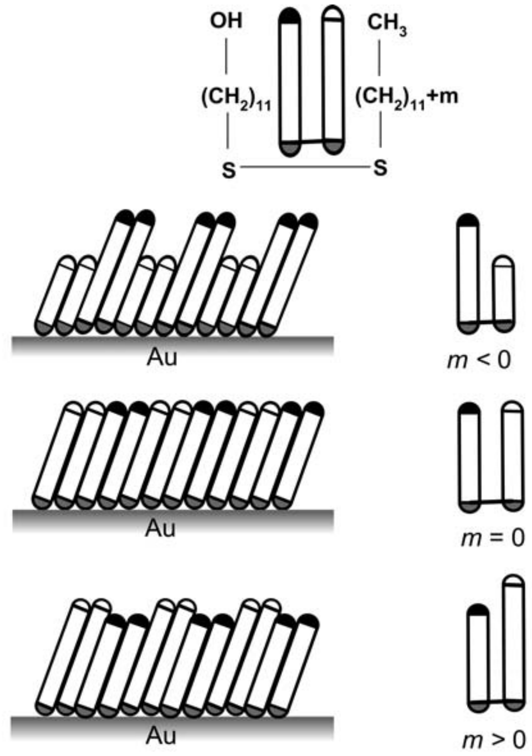

Figure 17 *Self assembled monolayers on gold surface*

The time for removing substrates from the preparing solution and cleaning with correspondent solvent took about 10 min before the droplet experiment started, in order to prevent any contamination when they are exposed to the air. Since fresh prepared gold-mica surface tends to be contaminated easily, especially for hydrophilic substrate surfaces. And then they were immediately placed on the substrate holder for the further drop experiments. Maximum of 6 droplets will be placed on different spots on each sample surface and after drop deposition the evaporation process was recorded. The total experiment time for recording more than 6 droplet evaporation processes on each substrate took roughly 40 min.

The chemisorption of either thiols or dialkyldisurfites on the Au (111) surface gives Au$^+$-thiolate (RS-) and releases H_2. The chain tends to form a hexagonal ($\sqrt{3} \times \sqrt{3}$) R 30° layer on the Au (111).

$$Au_n{}^0 + RSH \rightarrow \left[RSAu^{2+}H^-\right] \cdot Au_n \rightarrow RS^-Au^+ \cdot Au_n + \frac{1}{2}H_2$$

3.1.3 Polymer substrates and drop evaporation

3.1.3.1. Chemicals

- Extruded polystyrene (PS) plate (Weight average molecular weight Mw = 284 kDa and polydispersity PDI = 2.6) with 1.2 mm thickness, provided by Good fellow Ltd., UK. (The 150 × 150 mm PS plate was cut into substrate with a size of 25 mm × 25 mm prior to use)
- Polystyrene powder (in-house synthesis). With molecular weights M_W = 20.9, 24.3, 29.6, 62.5, 97.5, 210, 339, 643, 1102, 1445 kDa and polydispersity M_W/M_n = 1.03, 1.05, 1.03, 1.06, 1.04, 1.07, 1.07, 1.10, 1.09, 1.16, respectively.
- Poly (ethyl methacrylate) (PEMA) powder, PSS GmbH, Mainz, Germany. Weight average molecular weight M_W = 4.73, 7.49, 45, 142, 500 kDa and polydispersity of M_W/M_n = 1.08, 1.07, 1.05, 1.02, 1.11, respectively.
- Ethyl acetate, analytical grade, Sigma-Aldrich Chemie GmbH, Germany, surface tension at 25°C, $\gamma = 23.7$ mN/m
- Toluene, HPLC grade, Merck KGaA, Darmstadt, Germany, surface tension at 25°C, $\gamma = 27.9$ mN/m
- Trichloroctadecyl (OTS) silane, fur synthesis, Merck, Germany

3.1.3.2. Preparation of polymer substrate

For the experiment on evaporation of solvent drops on a soluble solid support, either extruded polymer substrates or polymer substrates prepared in-house from polymer powder with a narrow molar mass distribution were used. The polymer powder was compression molded above the polymer glass temperature at higher pressure with a hydraulic lab press (PW 40E machine) (**Figure 18, left**). For this, a piece of Kapton foil was cut into the size of mold and placed in it for getting a smooth polymer surface. Then ~600 mg polymer powder was placed into a stain steel mold sitting on a base plate. The base plate is connected with vacuum for removing the air inside of polymer melt. When polymer becomes mobile, a pressure is applied. In these processes the temperature of mold for getting polymer melt is set as 40°C above glass transition temperature of each kind of polymers and the pressure is 10 KN. The times used for the heating process and cooling process are 40 min and 30 min respectively, and the pressing process is hold for about 10 min. The polymer distributes inside of mold evenly and then a polymer plate can be obtained (**Figure 18, right**).

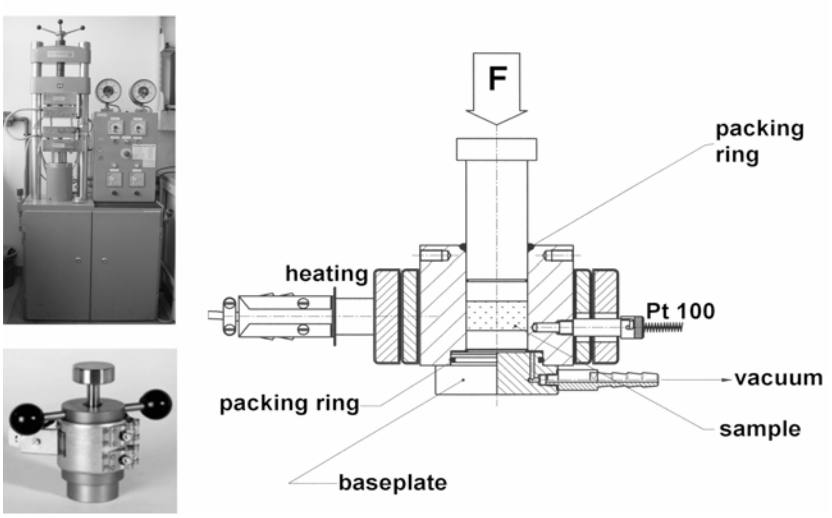

Figure 18 *Hydraulic lab press PW 40E machine and press mold*

In this work, PS or PEMA powder with different molecular weights were compression-molded in hydraulic Press (PW 40E) at 160°C or 100°C respectively, at 10 kN pressure into 1mm thick transparent disk (except for PS of 20.9 kDa, a opaque sample was obtained) with a diameter of 25 mm. Their density is about 1.0 g/cm^3 (for different length and size of polymer plate, the required weight of polymer material, the density of the polymer plate after compressed are listed in a table attached to the machine). PS plates were rinsed several times with methanol in an ultra sonic bath for15 min and then dried with a N_2 gas flow. The PEMA samples were rinsed with pure water several times and then dried with N_2 blow flow.

3.1.3.3. Preparation of OTS-silicon substrate

For better understanding the evaporation dynamics coupling with dissolution process, a comparison is made between evaporation process of toluene droplets on a soluble polymer substrate and evaporation process of toluene on a non-soluble substrate - OTS-silicon substrate surface. The silanization of silicon substrates with trichloroctadecyl (OTS) silane is performed in two steps. After hydrophilisation of the substrate surface, it is hydrophobized.

The silicon substrates with a size of 1.0 cm × 1.0 cm were immersed into a mixture of ultrapure water, ammonium hydroxids and hydrogen peroxide (vol 5:1:1) in a quartz beaker. The beaker is put in a water bath and heated up until the temperature of the mixture reaches 80°C. 10 minutes later the mixture is allowed to cool down. As the temperature lowers to 50°C, the mixture is diluted by adding ultrapure water into the beaker up to the rim. Then half of the solution is spilled and refilled again with ultrapure water. This process is repeated at least eight times in order to completely remove the chemicals. Afterwards, the beaker is emptied completely and filled with ultrapure water. The substrates are rinsed twice by immersing into ultrapure water. Finally the substrates are exposed to an ultrasonic bath for 5 min kept under ultrapure water and rinsed with water a final time.

To increase the hydroxyl group density on the silicon surface for better performance of the hydrophobization step, the substrates are put into a mixture of water and chloric acid (36-38%) (1:1) in a Teflon beaker and ultrasonicate for 15 minutes. After rinsing with ultrapure water eight times in order to completely remove the residue of acid, then substrates are consecutively washed with water-free methanol, methanol/chlorform (1:1) and chloroform in a teflon beaker for 5 minutes in an ultrasonic bath. Then substrates are left in chloroform.

In a different Teflon beaker a mixture of decaline : tetrachlorocarbon : chloroform (7:2:1) is prepared and 1% (vol.) OTS is added with a syringe. Hereby care is taken to avoid any contamination with water. The substrates are immersed into with their polished side up and left in there for over night.

After at least 12 hour, the substrates are taken off the mixture and placed in a beaker. Consecutively rinsing with a sequence of chloroform, chloroform/methanol and methanol in ultrasonic bath for 5 minutes finishes the hydrophobisation. Finally the hydrophobised substrates are moved quickly into a clean beaker containing ultrapure water. As a test the water meniscus should move with a straight over the substrate without any drop forming.

3.1.4 Microchannel experiments

3.1.4.1. Chemicals

- H_2SO_4, 95-97%, for analysis, Merck, Darmstadt, Germany
- 3-Aminopropyltriethoxysilane (APTE) 98%, ABCR GmbH & Co. KG, Karlsruhe, Germany
- Acetone, HPLC grade, Merck, Darmstadt, Germany
- Tetrahydrofuran THF, Acros, New Jersey, USA
- H_2O_2, 35%, for analysis, Merck, Darmstadt, Germany
- 0.2 µm PTFE filter (Millipore Cooperation, Bedford, USA)
- Pipette research variable 100-1000 µl, Eppendorf, Hamburg, Germany
- Universal capillary holder for Femtotip II, Eppendorf, Hamburg, Germany

3.1.4.2. Consumable materials

- Borosilicate glass (Hilgenberg GmbH, Germany)
- Femtotip II, diameter of opening tip 0.5 ± 0.2 µm, Eppendorf, Hamburg, Germany
- Fused silica tube (outer diameter 360 µm, inner diameter 20 µm), Upchurch scientific, Oak Harbor, WA
- Glass syringe, Fortuna, Frankfurt/Main, Germany
- Teflon tube, Hamilton, Germany

3.1.4.3. Preparation of glass capillary and chemical treatment

Two different chemical surface treatments of the inner glass surface are employed. First, the borosilicate surface was exposed to a solution containing sulphuric acid H_2SO_4 and hydrogen peroxide H_2O_2 in a mixture of 7:3 (v:v) for 2 days. After thorough rinsing with ultra pure water the capillary was kept in water until use. Prior to use it was kept in an ultrasonic bath for 15 min and rinsed again with ultra pure water. For the second treatment, the inner capillary surface was modified by chemisorption of 3-Aminopropyltriethoxysilane (APTE)[85]. An aqueous solution of 1% APTE was stirred for 20 min and after that filtered through a 0.2 µm PTFE filter. Afterwards, the glass capillaries were immersed into the pre-hydrolyzed solution for 30 min., washed with ultra-pure water and kept at 100°C for 1 h. After washing with acetone, ultra-pure water, acetone and THF by sequence, the capillaries were sonicated in acetone.

3.1.5 Optical parts

For the homemade camera system, various optical parts were used.

- Cold Light Lamp with flexible arms, Optometron GmbH, Munich, Germany
- 2×, 5× objective, Mitutoyo, Japan
- Universal capillary holder, Eppendorf, Hamburg, Germany
- Zoom objective, Navitar, Inc., NY, USA
- Ultrazoom tube, Navitar Inc., NY, USA
- Digital camera, Basleer Vision Technology, Ahrensburg, Germany
- Digital color camera, Evolution^{TM}MP, Media Cybernetics, USA
- Three-axis manipulator, Narishige, Japan
- Stepper motor, EC Motion GmbH, Germany
- Motor controller, Lang GmbH, Hüttenberg, Germany

3.2 Methods of investigation

3.2.1 Self-made double camera system

3.2.1.1. Experimental setup for evaporation of droplets on SAMs

To measure the evaporation of sessile drops on SAMs, a homemade experimental setup was used (**Figure 19)**. It consists of a movable capillary holder controlled by a micro-manipulator, to which a Femtotip is attached for deposition of droplets in the µm range. The droplets are placed on top of the substrate lying on a table (Owis, staufen, Germany), which can be adjusted manually in all three directions for access to different spots of the substrate. To minimize the movement of the Femtotip, the filling of it with the liquid is decoupled from the syringe by a Teflon tube. From behind the droplet a light source for bulk droplet contrast is placed. The optics consists of either a 5× objective or a 2× objective connected with a zoom objective with a magnification of 0.7, 1.0, 1.5, 2.0, 2.5, 3.0, 3.5, 4.0 or 4.5 respectively. A digital camera with a self-written Two-Cam-Capture program (Acesoft, Bonn, Germany) separated from the objective by a tube images the evaporating droplet and then displayed it on a monitor.

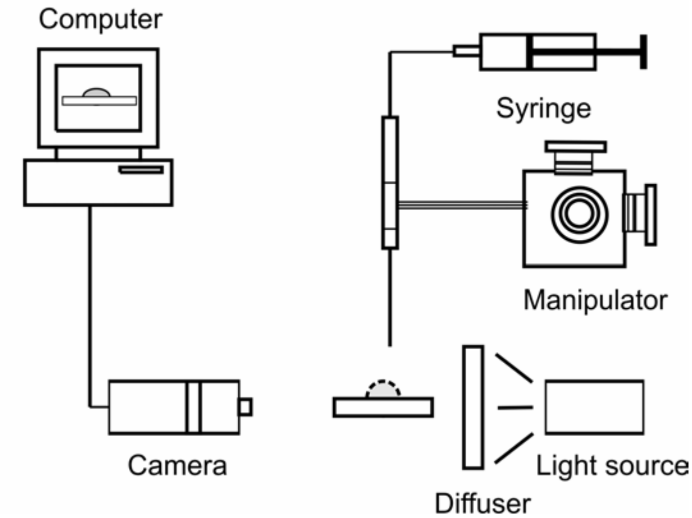

Figure 19 *Experimental setup for water droplet deposition onto SAMs surfaces*

After the cleaning process (shown in 3.1.1) and proper connection of syringe, teflon tube and Femtotip II, a 1.0 cm wide long syringe was rinsed several times with filtered ultrapure water. After that the investigated substrate was placed on the x- and y- movable platform. The syringe filled with filtered ultrapure water was placed above the substrate and the table was adjusted to get a sharp static image of the Femtotip. A water droplet was formed on the substrate surface and observed by a horizontally placed camera under angle of 1 ~ 2° versus substrate surface to get a reflected image of the droplet on the substrate for earlier analysis. The droplet deposition as well as the evaporation process was imaged and recorded with a highest capturing rate of 170 ms per frame (for double camera), 87 ms per frame (for single camera) and with a resolution of 640 × 480 pixels.

The different sizes of droplets are generated by two ways. For smaller droplets a Femtotip was used and for the bigger drop sizes, micropipette was used with a capacity of 0.5 µl to 10 µl. A 2× or 5× objective was used for droplet volume bigger than 0.5 µl and for droplet volume smaller than 100 nl, respectively.

Experiments were performed under temperature at 23 ± 2 °C, a relative humidity 45 ± 3 %, an ambient pressure 998 ± 2 mbar and with a camera magnification changing between 1.0 and 4.5. The characteristic droplet parameters as drop height and contact radius were extracted under assumption of a circular drop with a self-written analysis tool in Image Pro-Plus (Media Cybernetics, Inc., Maryland, USA) after the tip had left the droplet. The contact angle θ, the drop cap surface A_s, the drop volume V and the contact area were calculated from the received drop parameters using **Eq. 4 – 8**.

3.2.1.2. Experimental setup for evaporation of solvent drop on polymer substrates

An experimental setup is shown in **Figure 20**. The syringe system consists of a gastight glass syringe, a Teflon® tube and a fused silica tube as the tip with an outer and inner diameter of 360 ± 10 µm and 20 ± 2 µm, respectively. The piston inside the syringe is moved by a stepper motor with a speed range between 10 µm/s and 7 mm/s. The actuator for the substrate movement consists of a sample holder and of independently controlled linear x-, y-, z-stepper motors with a speed range between 10 µm/s and 11 mm/s. For microstructuring, droplets of toluene were placed on polystyrene (PS) substrates, either cut from commercial 1.2 mm thick extruded polystyrene plates, or compression molded 25 mm PS disk plates. To optically control the micro-structuring process, the pendent droplet and the moving substrate are illuminated by a cold light source with a diffuser for an optimal optical contrast. The actuator movement and the drop evaporation process were imaged with a camera system, including a 5x-objective, an ultrazoom tube and a digital camera, with a self-written Two-Cam-Capture program. After drop evaporation, the topology of the resulting microstructure in the polymer surface was imaged with a 3D confocal white light-microscope of the disk-scanning type.

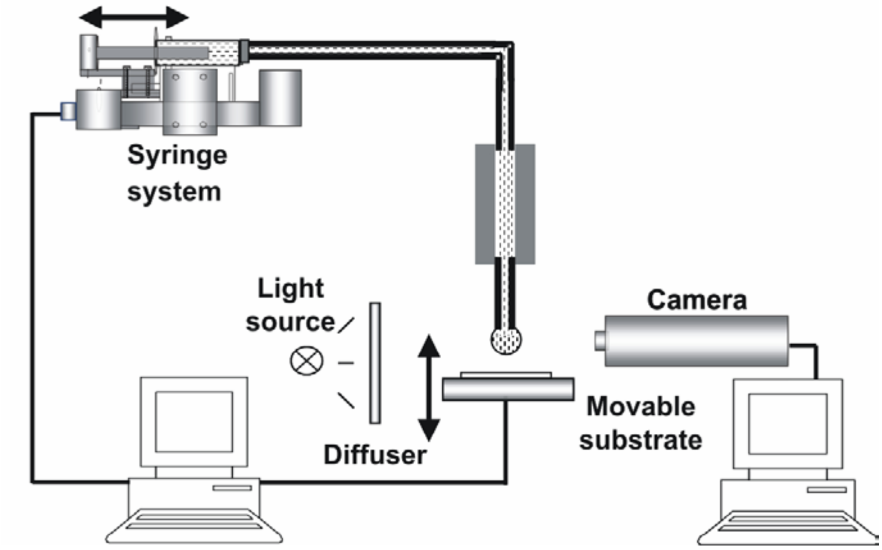

Figure 20 *Experimental setup for the microstructuring process.*

Figure 21 shows the two basic procedures to generate microstructures in the polymer surface. In non-contact mode the substrate is moved close to the pendent toluene drop without solvent-polymer contact. In contact mode the toluene drop is placed onto the polymer surface, forming a liquid bridge. The image reflected from the substrate surface is used to accurately control the distance between the droplet and the polymer. The approach speed, the delay time, and the retraction speed are independently controlled with a self-written software tool.

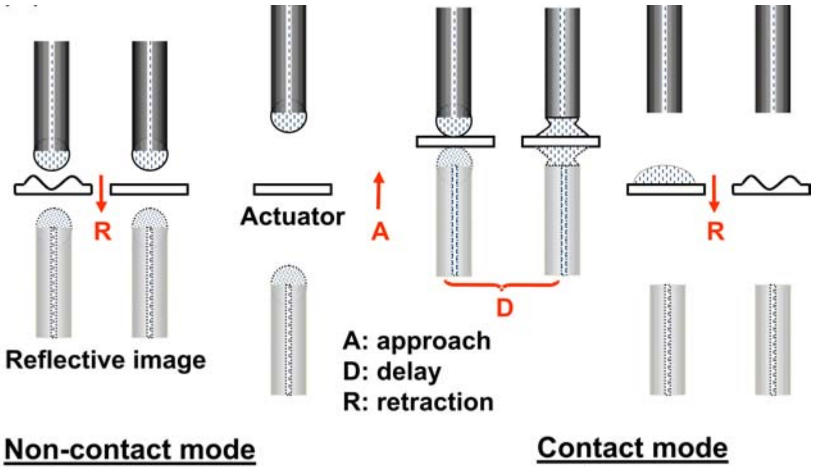

Figure 21 *With experimental setup from* **Figure 20**, *two basic procedures are performed to generate micro-topologies in a polymer surface. On the left, solvent vapor of a solvent drop diffuses into polymer surface with a distance of 30 µm between drop apex and polymer surface. On the right, a solvent drop is deposited onto the polymer surface through the contact of solvent drop and polymer substrate surface. Approach (A) and retraction (R) speed and the delay (D), i.e., the waiting time in contact, are variable.*

3.2.1.3. Droplets in microchannels - microfluidics setup

Here I use an alternative method to measure interfacial tensions between two immiscible liquids. For the purpose of measure interfacial tension, plugs of immiscible liquids are prepared. This is a novel technique especially developed for direct measurement of interfacial tension in microfluidics channel. A slightly modified experiment setup is shown (**Figure 22**).

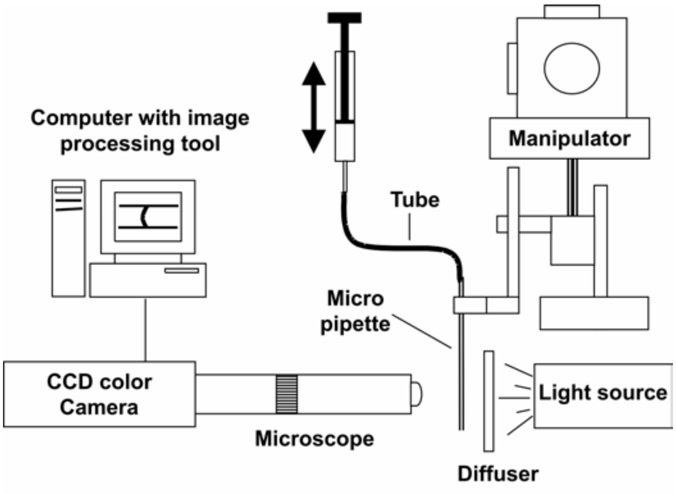

Figure 22 *Schematic of experimental setup for the measurement of interfacial tensions between two immiscible liquids in contact in a microchannel. The micropipette is arranged horizontally, i.e. parallel to the table (unlike the syringe in Figure 18)*

This experimental setup is developed, based on the experimental setup shown in **Figure 19**. Instead of manually controlling the liquid movement, a program is applied for controlling the liquid with lower speed down to the 10 µm/s.

The experiment was carried out by the following four steps: first soaking up air, secondly soaking up liquid 1 (L1) for contact between liquid 1 and air, thirdly soaking up liquid 2 for contact between liquid 1 and liquid 2 (L2), and finally soaking up air again for contact between liquid 2 and air. Thus three interfaces are generated in the microchannel (**Figure 23**). The contact angles between the interface of each component versus air, liquid 1, and liquid 2 can be measuring directly.

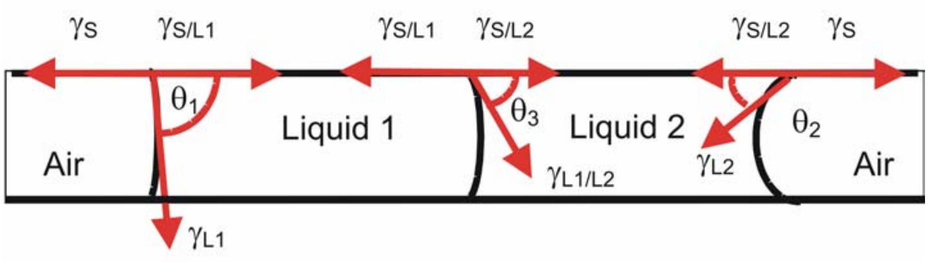

Figure 23 *Denotation of contact angles, surface and interfacial tensions of two immiscible liquids in contact in a microchannel. From the three contact angle and the surface tensions of the pure liquids, the interfacial tension* $\Delta\gamma_{L1/L2}$ *can be calculated.*

The projections of the menisci were visualized by a zoom objective at once or sequentially. The projected menisci are fitted with a circle running through the apex of the meniscus and the three-phase contact points between the liquids Li and the glass walls, i.e. the solid surface. This is marked with a straight line to rule out artifacts from optical refraction. The contact angle is determined from the intersection of the fitted circle and this line. Alternatively, it is determined from the height of the meniscus apex and the inner radius of the glass capillary. As resulting contact angle I took the average of the two angles from the lower and the upper wall of the microchannel. The measurements were carried out at room temperatures.

To calculate the interfacial tension $\Delta\gamma_{L1/L2}$ between the two liquids L1 and L2, I derived its dependence on three contact angles θ_i. For the simplest case of equal surface tensions γ_S at the solid-air interfaces close to liquid L1 and liquid L2, respectively, I can write the Young equation for each observed interface in equilibrium as:

$$\gamma_S = \gamma_{S/L1} + \gamma_{L1} \cos\theta_1 \qquad \text{Eq. 32}$$

$$\gamma_S = \gamma_{S/L2} + \gamma_{L2} \cos\theta_2 \qquad \text{Eq. 33}$$

$$\gamma_{S/L1} = \gamma_{S/L2} + \gamma_{L1/L2} \cos\theta_3 \qquad \text{Eq. 34}$$

γ_i are the interfacial tensions of the corresponding interfaces denoted by indices (S: solid, L1: liquid 1, L2: liquid 2) and θ_i the corresponding contact angles. In particular, γ_{L1} and γ_{L2} are the surface tensions of the liquids in contact with air. After combination of **Eq. 32 - 34** the interfacial tension between L1 and L2 can be expressed as:

$$\gamma_{L1/L2} = \frac{\gamma_{S/L1} - \gamma_{S/L2}}{\cos\theta_3} = \frac{\gamma_{L2}\cos\theta_2 - \gamma_{L1}\cos\theta_1}{\cos\theta_3} \qquad \text{Eq. 35}$$

Therefore, from measurement of the contact angles at the three different interfaces and the surface tensions of the liquids, I can calculate the interfacial tension of the two liquids in contact. Please note that the corresponding interfacial tensions with respect to the solid interface cancel out. Consequently this novel technique for determination of interface tension in combination of pure waters in contact with either toluene, or chloroform, or n-hexane, respectively is observed.

For the measurement of contact angles a homemade experimental setup (**Figure 22**) is utilized. It consists of a motor-driven syringe, to which a micro glass pipette is attached via a PTFE (Teflon®) tube. The pipette is made of borosilicate glass and has an outer and inner diameter of 1.5 mm, 0.5 mm respectively. With a round diameter wetting artifacts from wedges are avoid [86]. The pipette was horizontally adjusted in the focus of a digital color camera with a three-axis manipulator. The velocity of the liquid was controlled with a stepper motor and a motor controller with flow speeds between 10 μm/s and 900 μm/s for withdrawing air and the liquids.

Throughout all procedures ultra-pure water is used. The syringe and the PTFE tube were cleaned by a routine procedure, as shown in 3.1.1, the teflon tube was connected to the syringe and the chemically modified borosilicate glass capillary.

3.2.2 Laser scanning confocal microscopy

For the investigation of the optical properties of the microstructures in soluble material surfaces, the three dimensional images of microstructure are required. To this end, a modified laser scanning confocal microscopy (LSCM) is applied, which is in principle developed on the basis of the confocal microscopy.

The confocal microscopy is originally called as double focusing microscopy. As an imaging technique the confocal microscopy is different from the conventional microcopy which provides a wide-field image due to the conservation of the light intensity. In this technique a point illumination and a spatial pinhole are coupling into an optical plane in the front of the detector to eliminate the out-of focus signals or the flare in the specimens which are thicker than the focus plane. The focus plane is set at the plane of interest in the specimen. Only the light in the focus plane can pass through the pinhole before the detector. The contrast of specimens is recorded and the sharp 2D or 3D images are reconstructed by scanning point by point of specimen at various z-axis plane. The principle of confocal microscopy is shown **(Figure 24**).

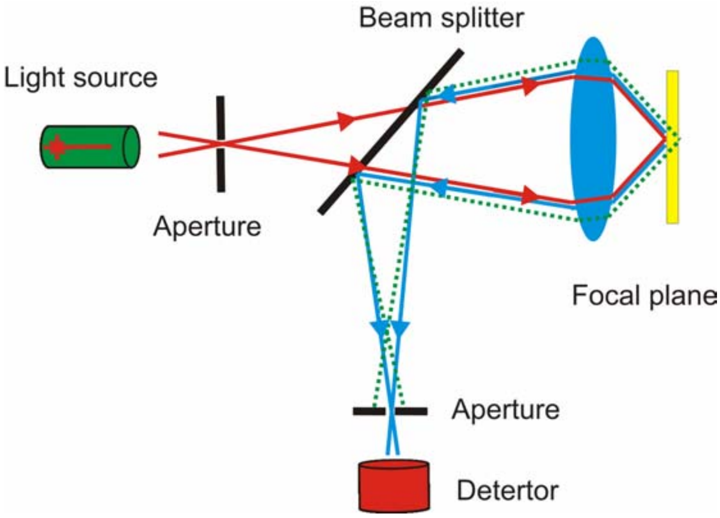

Figure 24 *Principle of the confocal microscopy*

There are commonly three types of confocal microscopy, laser scanning confocal microscopy (LSCM), spinning-disk (Nipkow disk) confocal microscopy and programmable array microscopy (PAM). The second one will be introduced after this section.

Here a commercial laser scanning confocal microscope (**Figure 25**) manufactured by Carl Zeiss (Göttingen, Germany) consisting of the module LSM 510 and the inverted microscope model Axiovert 200M is used. A slight of changes is performed by adding a transmitting light, in order to identify the up surface and back surface of specimens.

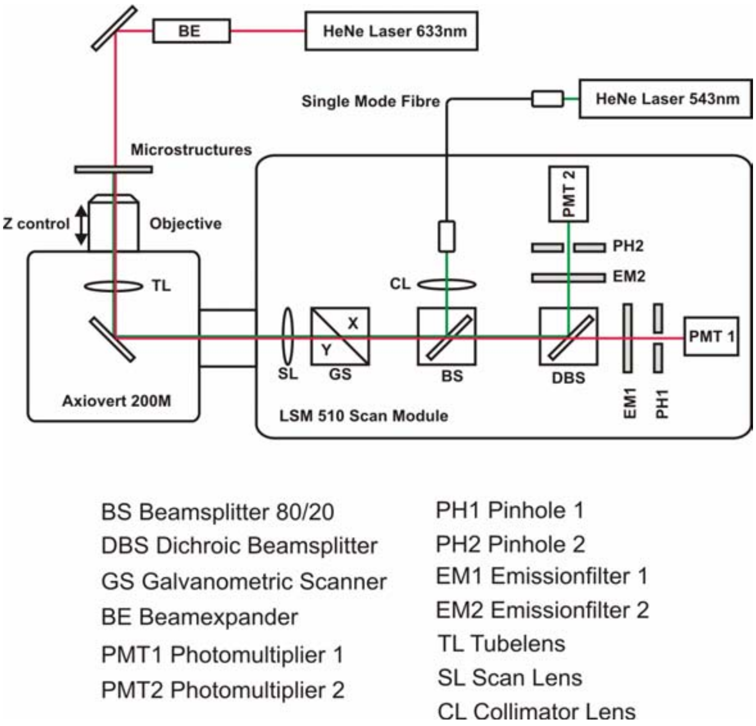

Figure 25 *Scheme of the modified laser scanning confocal microscopy setup in order to measure the transmitted and reflected light simultaneously [from handbook of Zeiss]*

For the present experiments, a Plan-Neofluar 10× objective with a numerical aperture of 0.3 and a working distance of 5.6 mm is used. The optical system was modified by coupling an external 5 mW helium-neon laser working at 633nm, aligned perpendicular to the x-y scanning plane of the microscope and collinear to the objective lens. In order to generate a plane wave front the laser beam was expanded 10 times using a beam expander working in Keplerian mode. This modification allows illumination of the samples in transmitted light configuration. For the reflected light configuration, the 543 nm line of a 1 mW helium-neon laser is used. The transmitted and reflected light collected from the objective were separated by a dichroic mirror and routed to two independent channels. In one channel a bandpass filter transmitting in the range from 500 nm - 550 nm was chosen to detect the light at 543 nm. In the second channel a longpass filter with a cut-off wavelength at 560 nm was applied. For detection, photomultipliers were used. By using pinholes with a diameter of 71 µm for the green light and 78 µm for the red light in the confocal position in front of the corresponding detector, light from thin optical slices with a thickness of about 12 µm can be collected from the focal plane.

3.2.3 3D confocal white light surface microscopy

The µsurf^{TM} microscopy station (NanoFocus AG, Oberhausen, Germany) consists of a compact confocal module (**Figure 26**). The confocal module is fixed on a precise stepper motor driven linear axis mounted on a bridge stand. The confocal module is allowed to move in z direction, whereas the sample is positioned by precise x-, y- slides. The whole station is controlled by a software. This special type of confocal microscopy serves to visualize and analyze a surface topology as that prepared in this thesis. Using a 20× or 50× objective the resolution was 1.5 µm and 0.6 µm laterally and 5 nm and 2 nm in height, respectively.

For x, y-scanning, the µsurf^{TM} confocal microscope uses a Nipkow spinning-disk, which consists of an array of pinholes arranged in a spiral shape. The rotating disk acts as either a multiple point source illuminated by a plan wave, or as its own detector pinhole. Similar to an acquisition device, the x, y section of the sample is acquired and then imaged through a real-time video and a frame-grabber. By moving it in z direction, a stack of depth information is acquired. Finally a 3D topography can be constructed.

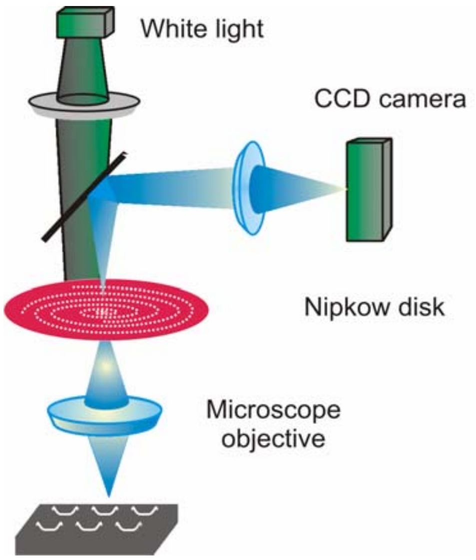

Figure 26 *Principle of 3D confocal white light surface microscopy µsurf*^{TM} [87, 88]

3.2.4 Scanning electron microscopy

Differing from normal light microscopy, SEM uses an electron beam produced by an electron gun mounted at the top of the microscope (**Figure 27**). The electron beam travels in vacuum in a vertically path through electromagnetic, lenses through which it is finally focused onto the sample. The condenser is used for focusing the beam into a very fine focal spot sized as 1 nm ~ 5 nm and then deflected by a scanning coil into a raster fashion over the sample. When the beam reaches the samples, the energy is transferred into the sample. Backscattered electrons, second electrons, Auger electrons and X-ray radiation are ejected from samples. The secondary electrons having low energy (~20 eV) are closed to the sample surface. Thus they are collected by a nearby detector i.e. photomultiplier and their signals are rendered into a two dimensional intensity distribution, which is then displayed and saved as a digital image.

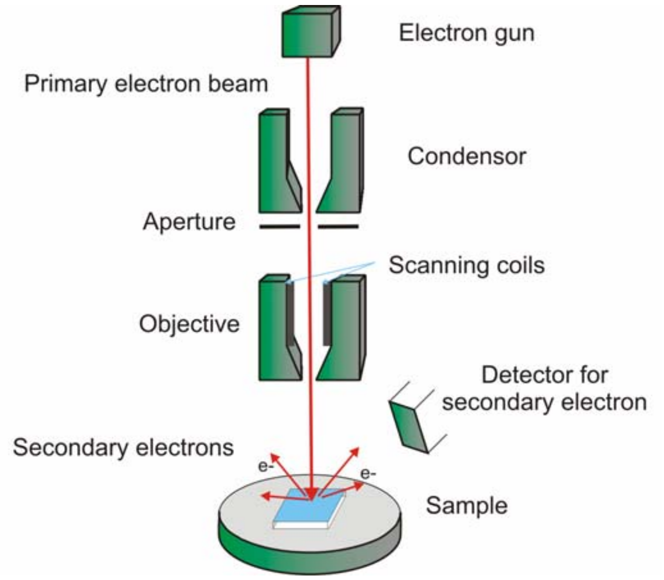

Figure 27 *Redraw of schematic of a scanning electron microscopy (SEM)* [50, 89]

3.2.5 Tensiometer

The surface tension of a liquid and the interfacial tension between two immiscible liquids were directly measured with a du Nöuy ring tensiometer (K11, Krüss GmbH, Hamburg, Germany). In principle, the tensiometer measures the pull-out force when a platinum ring or plate is pulled out of the liquid. The surface tension or interfacial tension is measured from the force with **Eq. 30** or **Eq. 31**.

To measure the interfacial tension, a several steps procedure is followed. First fill the beaker with a dense liquid, and then move down the cleaned ring into the liquid. The platinum ring is cleaned by placed into fire to get ride of organic contamination and then put on to the holder, prior to use. Afterwards a light liquid is carefully deposited on the dense liquid surface by a pipette to get another layer with thickness of ~2 millimeter. The ring was then moved up to the immiscible liquid interface and when it was moved into the top layer, the maximum force is measured. Such measurement is performed back and force ten times and finally a mean value is obtained.

4 RESULT AND DISCUSSION

4.1 Evaporation dynamics of pure water droplets on self assembled monolayers

In this chapter, the study is focus on the evaporation dynamics in an ideal liquid/solid system – water/self assembled monolayer on gold mica surfaces. A detail description of evaporation processes is given by the changes of the contact angle, contact radius, drop volume, and drop cap radius with drop evaporation time in single droplet for each SAM system. Moreever the studies on these varied parameters, especially on the drop initial volume will be extended into multiple drops with different initial drop sizes and then performed by a multidroplet analysis in order to have more accurate and confidential evaluation of surface properties.

4.1.1 One droplet experiment

Commonly the study of evaporation dynamics is performed on the investigation of parameter changes with evaporation time such as contact angle, contact radius, surface area, drop cap area and volume in a single drop. From these changes, the surface properties can be directly evaluated and understood.

4.1.1.1. Evaporation mode in dependence of surface hydrophilicity

The evaporation dynamics i.e. the contact radius and the contact angel versus time is shown in **Figure 28** for all SAMs. Basically three regimes as described in Chapter 2 are observed for nearly all SAMs. First the droplet is pinned and thus evaporates in the constant contact radius mode (CCR). After that, the drop shrinks with constant contact angle (CCA), while the contact line moves radically inward which can be seen as a kink in the plots.

Finally, both contact radius and contact angle decrease simultaneously (mixed mode). Normally, the duration in mixed mode takes about 10% of the total evaporation time. The hatched areas in the plot indicate the scattering of the kinks for all measurements performed on the different substrates and on different spots.

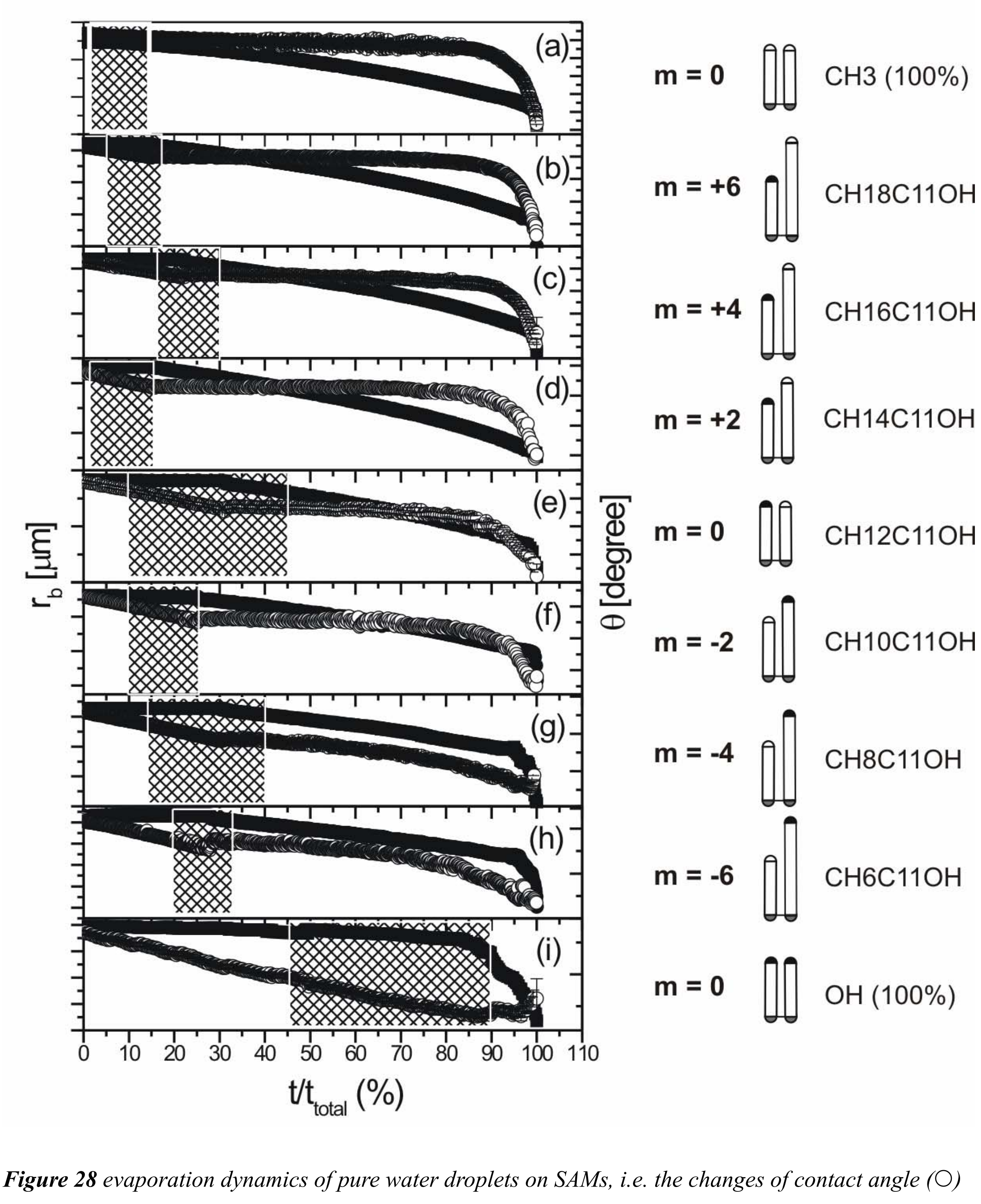

Figure 28 *evaporation dynamics of pure water droplets on SAMs, i.e. the changes of contact angle (○) and contact radius (●) with* t/t_{total} *(the real evaporation time divided by total evaporation time). The hatch area indicates the average value of transition from CCR to CCA plus/minus standard deviations. (a) - (i) for SAMs surfaces* CH_3*100% (DDT), C18C11OH, C16C11OH, C14C11OH, DDT/HUT(1:1), C10C11OH, C8C11OH, C6C11OH and HUT. The tick distance indicates 100 µm for contact radius and 20° for contact angle*

Transition point is plotted versus m and X_{HUT} (**Figure 29**). Transition point decreases slightly with m for m ≠ 0, until a jump to a much higher value is found for the hydroxyl-terminated gold mica surface (**Figure 29a**). However the transition point increases linearly with X_{HUT} values (**Figure 29b**).

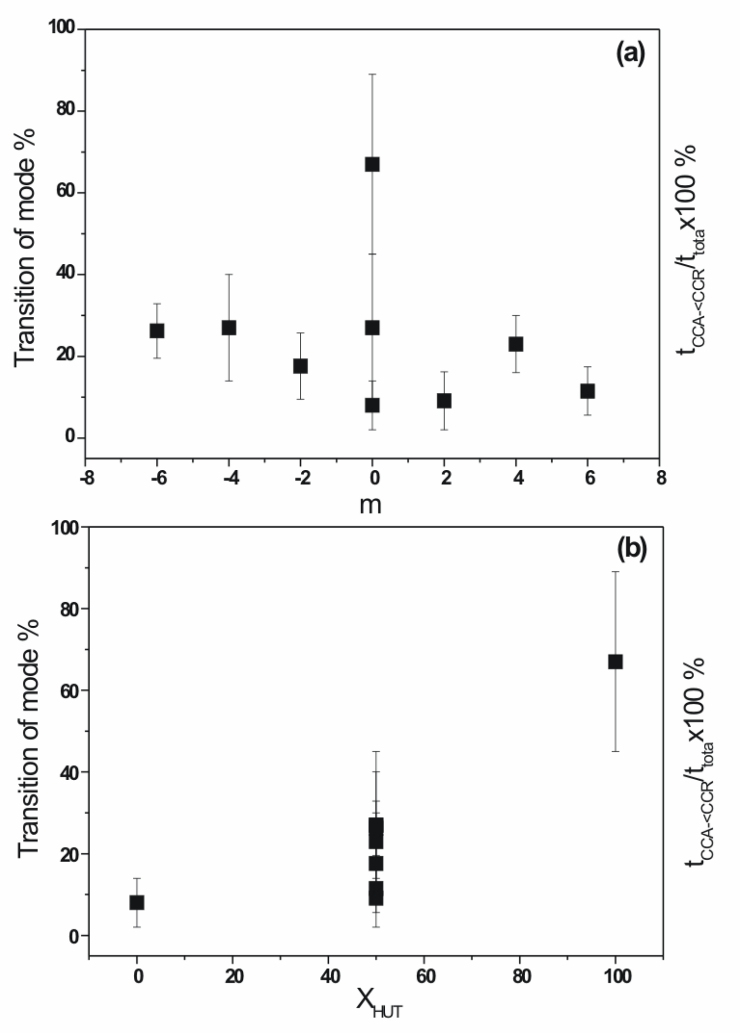

Figure 29 *Transition of evaporation (the values are taken from the middle point in the hatch area, in Figure 28) for CCR to CCA mode versus m and* X_{HUT}.

4.1.1.2. Advancing contact angle in dependence of surface hydrophilicity

To illustrate the role of the surface hydrophilicity of the SAMs, the advancing contact angles are plotted versus m and versus X_{HUT}, the mole ratio for m = 0 (**Figure 30**).

The advancing contact angle of the hydrophobic DDT, the hydrophilic HUT and the 1:1 mixture are 113 ± 2°, 21 ± 1° and 67 ± 3°respectively. These data shows linear decreases and thus can be described by Cassie equation $\theta = X_{DDT}\ \theta_{DDT} + (1-X_{DDT})\ \theta_{HUT}$ with $\theta_{DDT} \sim 113°$ and $\theta_{HUT} \sim 20°$, the corresponding contact angle on the pure surfaces. For $m \neq 0$, the θ_A is either lower or higher than the expected value, with a small deviation of ~3°. The differences between DDT and m = 6, and between HUT and m = -6 are almost as same as 24°. Roughly, θ_A decreases linearly for $m \neq 0$ with increasing influence of the hydroxyl group, i.e. the more it is exposed to the droplet. The slope indicates a change of ~ 7° per ethylene group.

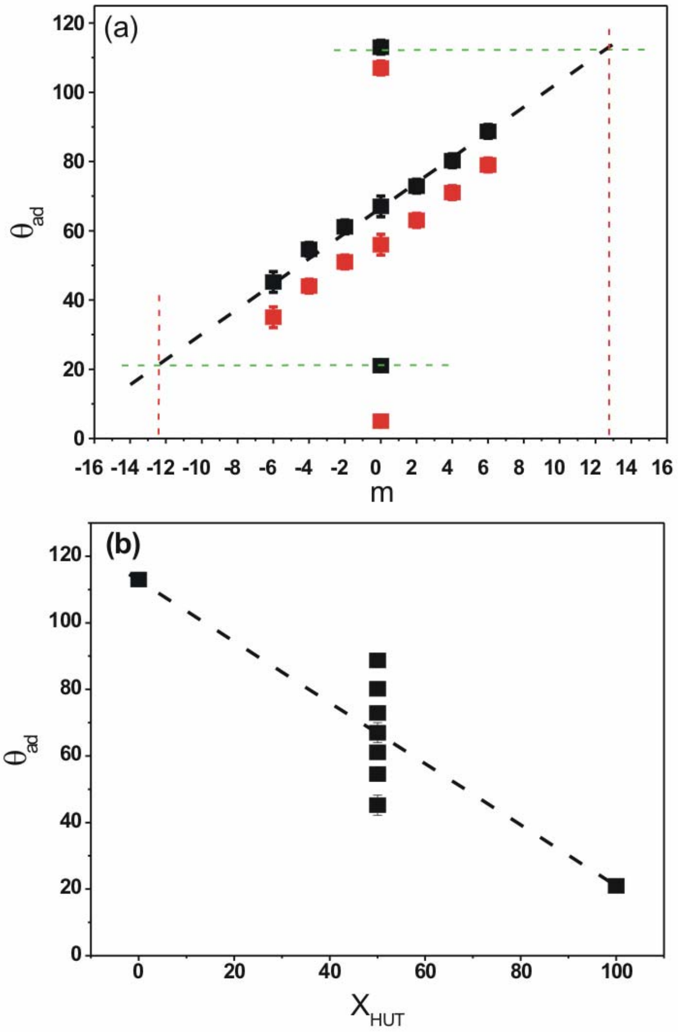

Figure 30 *The advancing (■) /receding contact angle (🟥) of pure water droplets on SAMs surface is in dependence on the variable m and X_{HUT} respectively. The larger differences 24° are found for SAMs containing only one functional group to its neighbor for m = 0. The contact angle difference of 7° is found when the difference of m is 2 for $m \neq 0$.*

Assuming the alkyl chains in SAMs m ≠ 0 can still be increased/decreased experimentally, then a further more hydrophobic/hydrophilic surfaces can be obtained. The advancing contact angle will then increase/decrease until a maximum value in DDT and a minimum in HUT are reached. To this end, a extrapolating linear line (in black) for m ≠ 0 into two opposite directions are drawn and the line is allowed to meet the two green dash line drawn for DDT and HUT. And then two kinds SAMs are observed with m ≈ ±12.5°, indicated by red lines.

4.1.1.3. Dependence of drop volume and volume$^{2/3}$ on evaporation time

In principle the evaporation rate for a given liquid/solid system is determined by the corresponding solid surface hydrophilicity. And the evaporation rate can be derived from the changes of drop volume versus evaporation time. This means that the surface hydrophilicity can be evaluated from the drop volume changes. To this end, drop volume or volume$^{2/3}$ versus evaporation are plotted and shown (**Figure 31**). The droplet volume typically decreases non-linearly with time. However, the droplet volume$^{2/3}$ declines linearly with evaporation time for m >0 SAMs. For m ≤ 0 SAMs, the curve of drop volume via evaporation time appears non-linear and the divergence from the linear line becomes more and more apparent as m continuously decreases.

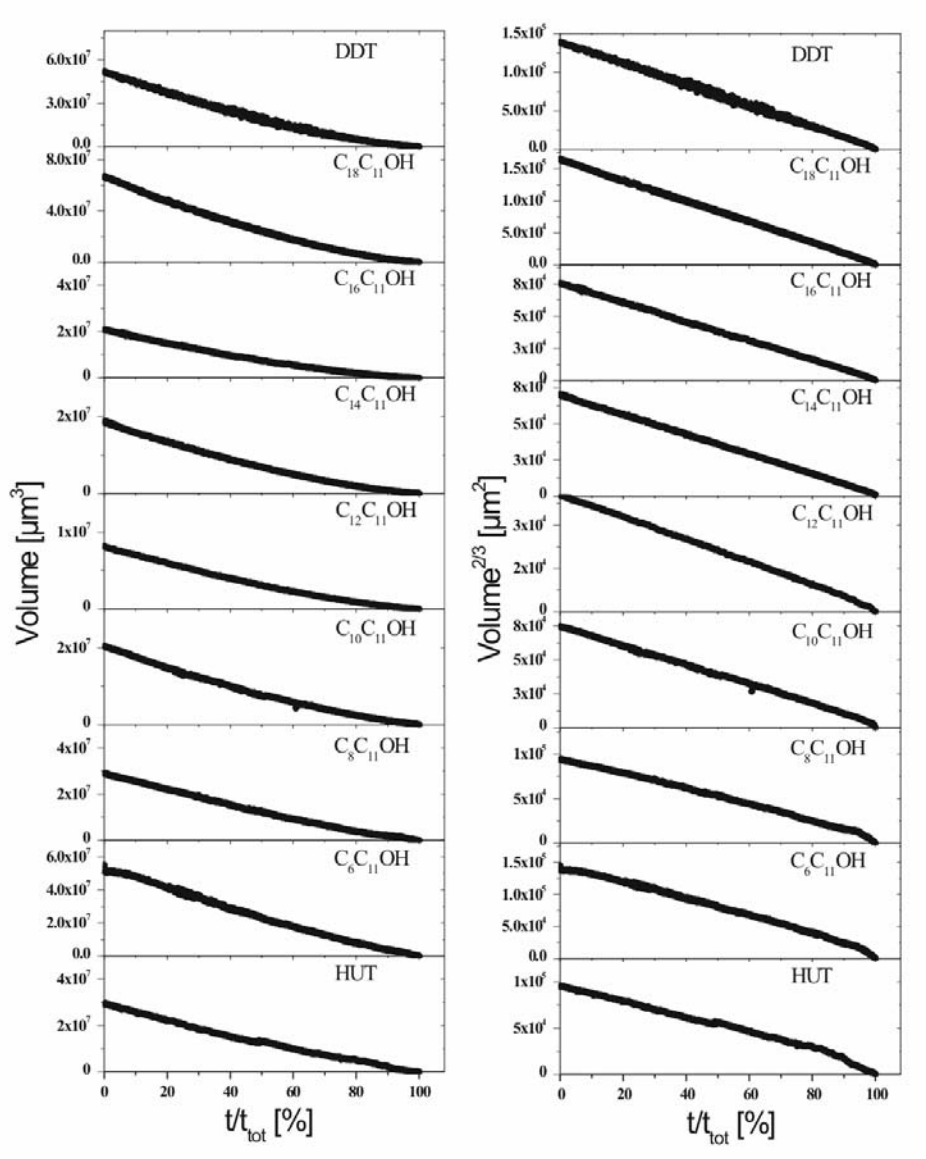

Figure 31 *Drop volume (left) and volume*$^{2/3}$ *(right) change with evaporation time in a single drop evaporation process for all SAMs surfaces.*

4.1.1.4. Dependence of drop cap radius on evaporation time

When plotting drop cap area via evaporation time, different curve shapes are found (**Figure 32**). For m > 0 SAMs, it shows linear, whereas for m < 0 SAMs, one or two kink appears in the middle of plot.

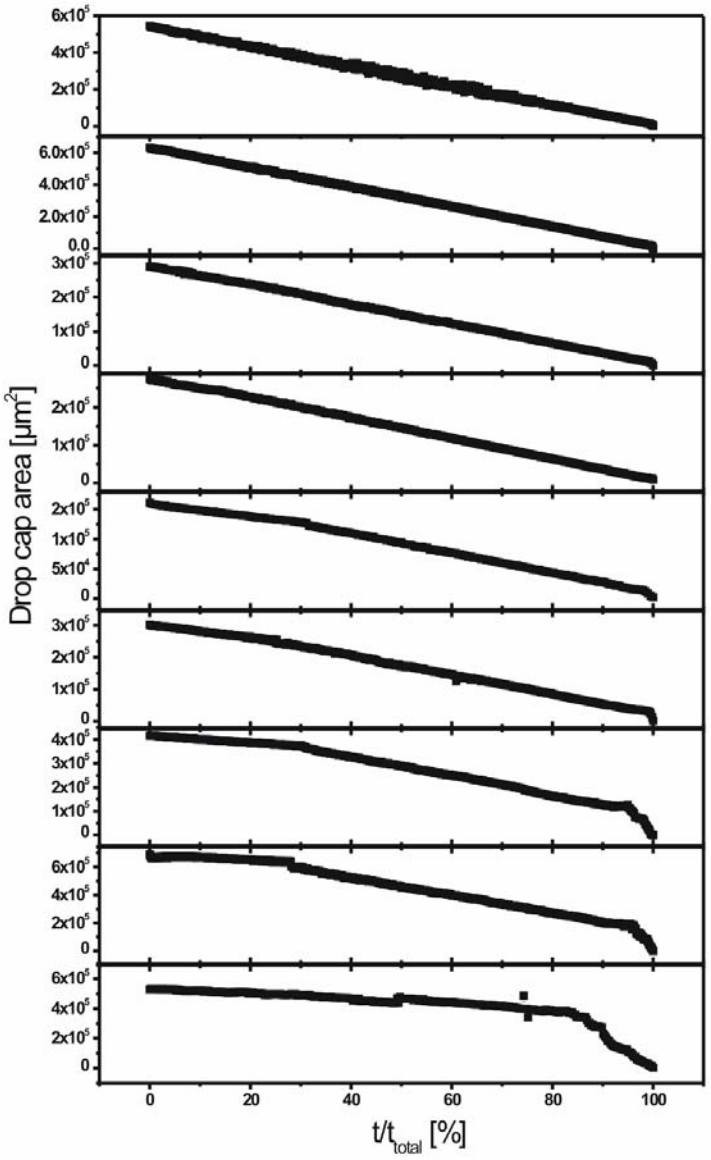

Figure 32 *The drop cap areas versus the evaporation time for all the SAMs. From top to the bottom there are DDT, C18C11OH, C16C11OH, C14C11OH, C12C11OH, C10C11OH, C8C11OH, C6C11OH and HUT surfaces, respectively.*

4.1.2 Multi-drop evaporation dynamics

Despite in a single drop the deviation of $V^{2/3}$ versus evaporation time from a linear line can be clearly seen in **Figure 31**, especially for hydrophilic surface i.e. HUT, this has not been noticed up to now. Theoretically $V^{2/3}$ via time should be always linear regardless of the surface properties. To reveal this a multi-drop analysis is taken. This approach allows us to study the influences of surface properties of different kinds SAMs on the total evaporation time, t_{tot}.

4.1.2.1. Volume changes with total evaporation time

For this purpose the total evaporation time for different initial volumes is measured on each SAM surface (**Figure 33**). As a reference volume, the evaporation time is received for a 5 nl drop from a fit with the scaling relation in **Eq. 17**.

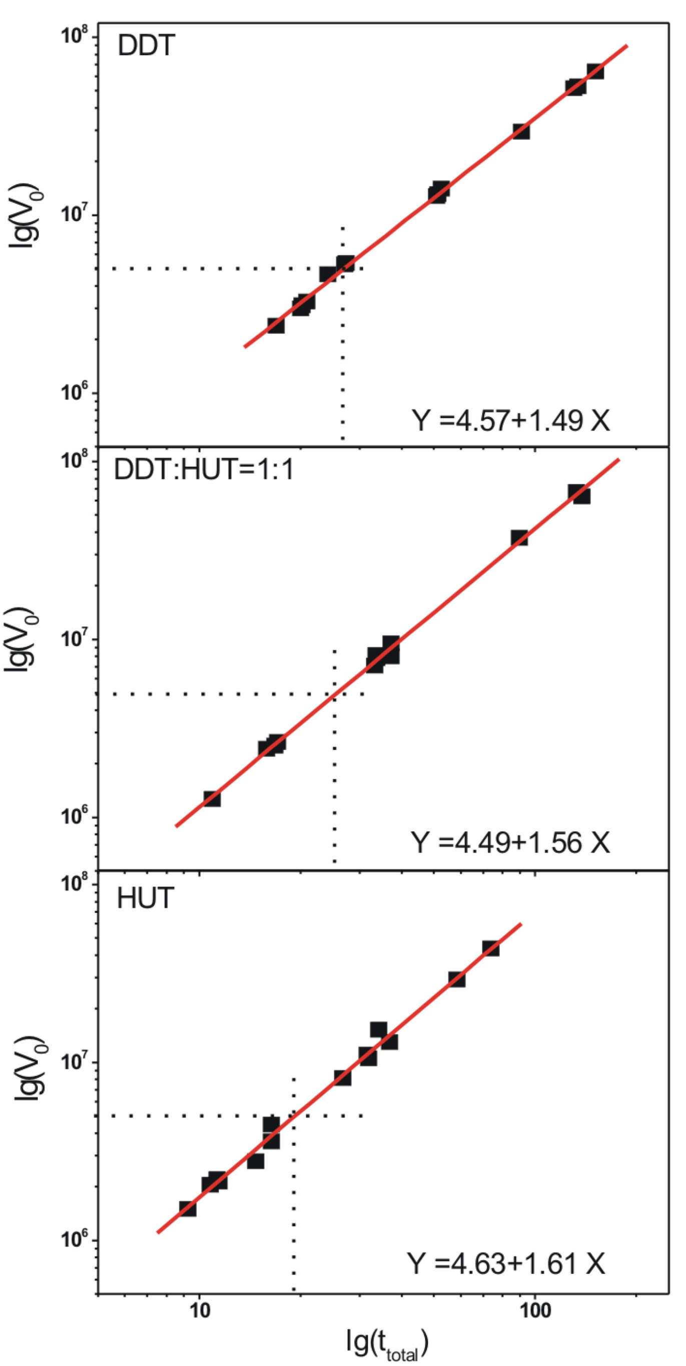

Figure 33 *Double logarithm of Initial drop volume versus total evaporation time of each single droplet for DDT, DDT:HUT (1:1) and HUT surfaces. The total evaporation time for a drop volume of 5 nl is obtained with a fit of the scaling relation in* ***Eq. 17****.*

Here the plots are shown only for three kinds of SAMs, DDT, DDT: HUT (1:1) and HUT. The total evaporation time for a 5 nl drop can be directly read from the dash lines on x-axis.

By extracting these values for all SAMs, the total evaporation in dependence of m and X_{HUT} was obtained (**Figure 34**). The total evaporation time decreases with increasing X_{HUT} for the SAMs with m = 0. For $m \neq 0$, there are two constant values. For m > 0, the total evaporation time is ~ 30s for a 5 nl water drop. For m < 0, t_{total} is ~ 24s. Thus the total evaporation time decreases with increasing hydrophilicity and roughly with increasing influence of the hydrophilic chain for $m \neq 0$.

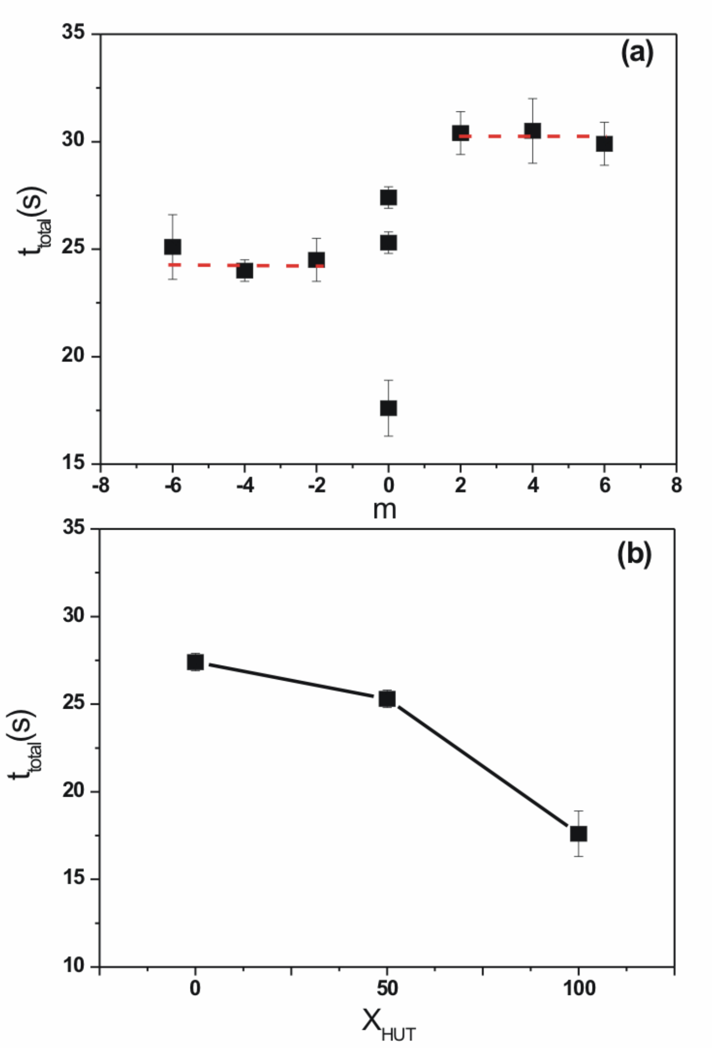

Figure 34 *The variable m in dependence of the total evaporation time of 5nl droplet changes with surface hydrophilicity for all SAMs surfaces (a). And the variable* X_{HUT} *in dependence of the total evaporation time of 5nl droplet changes with surface hydrophilicity for m = 0 (b)*

In the double logarithm of initial drop volume versus total evaporation time, the linear fit provides both a and b values in the equation of Y = a + bx. For DDT, 1:1 DDT: HUT and HUT SAMs, b values change from 1.49, 1.58 to 1.61 and a value from 4.57, 4.49 and 4.63.

4.1.2.2. b in dependence of surface properties

The double logarithmic plots of initial drop volumes versus total evaporation time reveal a linear dependence for all SAMs samples (**Figure 33**). A fit of the plots with a scaling law of type $V_0 = a \times t_{tot}^{b}$ provides an exponent b. The changes of b via m and X_{HUT} are plotted (**Figure 35**).

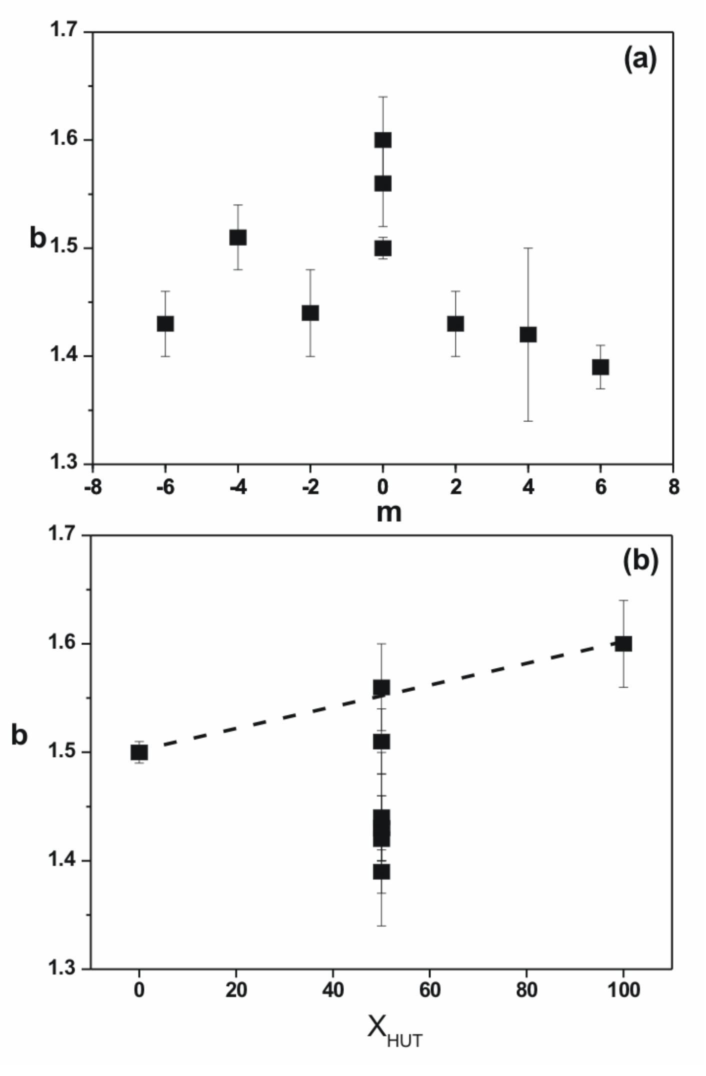

Figure 35 *Dependence of the scaling exponent b on m and* X_{HUT}. *For SAMs with* $m = 0$ *and* $m \neq 0$

The dash lines are a guide to the eyes. The most striking observation is that for m = 0, the scaling exponent increases from 1.5 for hydrophobic SAM to ~1.6 for the hydrophilic one. Moreever, the SAMs with m ≠ 0 show a constant value of ~1.43 if the value for m = - 4 is taken as insignificant.

4.1.3 Investigation of evaporation dynamics of pure water droplets on SAMs

4.1.3.1. Static contact angle measurement

Despite for m = 0, the intermediate SAM between DDT and HUT – C12C11OH is not prepared by simply mixing of HUT and DDT [90, 91], the θ_A shows a linear dependence on mixing ratio X_{HUT} of two different alkyl chain length of DDT and HUT. And it follows the Cassie-Baxter equation $\theta = X_{DDT}\ \theta_{DDT} + (1-X_{DDT})\ \theta_{HUT}$[15]. The slope of this curve (**Figure 30b**) is about ~0.9 degree/percentage of X_{HUT}. Therefore the surface hydrophilicity can be tuned by just varying the two alkyl chain length in this case.

For m ≠ 0, θ_A can also be considered as a linear dependence of m with a slope of 7° for each ethylene group. The longer is the hydrophilic chain, the more hydrophilic becomes the SAMs surface. Surface hydrophilicity can be tuned either by varying the mixing ratio or by modulating the length of an alkyl chain length with respect to the each other if mixing ratio is kept constant (50%/50% in this case).

The linear dependence of θ_A on m can be extrapolated to m ≈ -12. Chemically, this is a postulated disulfide C0C11OH, i.e. a disulfide with a hydrophilic chain only. The resulting advancing contact angle of ~ 20 ° indeed was measured for HUT, received from a thiol with a hydrophilic end group. Therefore, it can be announced that an influence of differences in the molecules density between thiol and disulfide coupling is neglectable. In extrapolation $\theta_A \sim 113°$, the value for the hydrophobic DDT surface provides m ≈ 12. That means the hydrophobic alkyl chain in the disulfide has to be much longer than the investigated ones to show no influences of the hydrophilic hydroxyl group anymore. The hydrophobic alkyl chain completely hides the lower positioned in plane thiol with the OH group. In contrary, for the shorter hydrophobic alkyl chain used here (m = ± 6, 4, 2) an influence from the arrangement of this chain on the contact angle can be expected.

4.1.3.2. The influence of surface roughness and heterogeneity on evaporation dynamics

Usually the hysteresis is an important criterion for evaluation surface hydrophilicity. In this study the surface hydrophilicity of SAMs is not only dependent on the alkyl chain length but also on the hysteresis which is resulted from surface roughness, heterogeneity and contamination.

For $m \neq 0$, the hysteresis is $10 \pm 0.5°$, and the surface roughness is mainly dominated by the underlying gold mica surface[92]. Whereas for m = 0, the hysteresis of DDT and 1:1 DDT/HUT SAMs is quite similar to the value for $m \neq 0$ SAMs. Commonly, it can be expected that a hydrophobic surface as that of DDT is less subject to hysteresis than a hydrophilic one as that for HUT since the HUT surface is highly sensitive to the tiny changes caused by contamination, when its surface is exposed to the air.

To learn more about the origin for hysteresis, it is necessary to look closely at the drop evaporation dynamics (**Figure 36**), especially the changes of contact angle versus drop evaporation time. The fluctuation of the drop is named as slip-stick. In slip-stick due to a small deviation from the equilibrium contact angle, a energy is imposed into the drop meniscus. When the drop contact angle is too small comparing to the equilibrium, a force is induced. The force is proportional to the difference between $(\cos\theta - \cos\theta_{eq})$[93]. The droplet starts to move when the forces reach a certain value. Slip-stick can be observed when the plot of contact angle versus evaporation time is enlarged by zooming in a small area. A typical zig-zag slip-stick behavior is found for m = 0 SAMs as DDT and HUT (**Figure 36**). However, in DDT SAMs the drop moves as a regular saw teeth, whereas it moves irregularly in HUT SAMs surface. For the other SAMs the same slip-stick was observed, however the magnitudes become smaller.

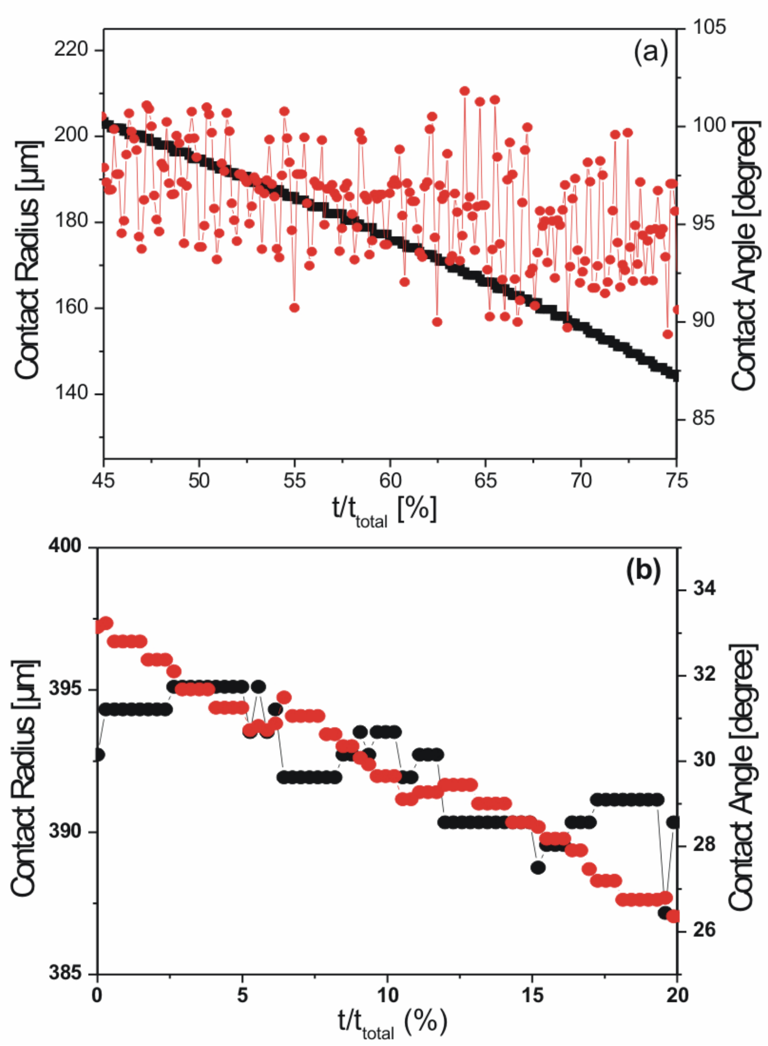

Figure 36 *Contact angle (●) and contact radius (■) versus evaporation time. The slip-stick behavior is observed in DDT (a) and HUT (b) SAMs surfaces.*

4.1.3.3. Drop size influences on the evaporation dynamics

To cross-check the drop size influences for comparing the results obtained from micro-liter bigger droplet evaporating on the SAMs[13, 14], the study on the droplet size influences on the evaporation process was performed. Two extremes, for instance of DDT and HUT, are selected and drop volumes ranges from micro-liter to nano-liter. When the double logarithm of volume versus evaporation time is plotted, it turns out that the influences of drop sizes are observed only for the hydrophilic surface rather than hydrophobic surface (**Figure 37**). The results for hydrophobic surface are in consistence with literatures. In contrary, for HUT surface, a divergence of line made by micro-liter drops from the line by nano-liter droplet can be observed. This again shows the hydrophilic surface is a non-ideal system and could result a deviation from ideal case.

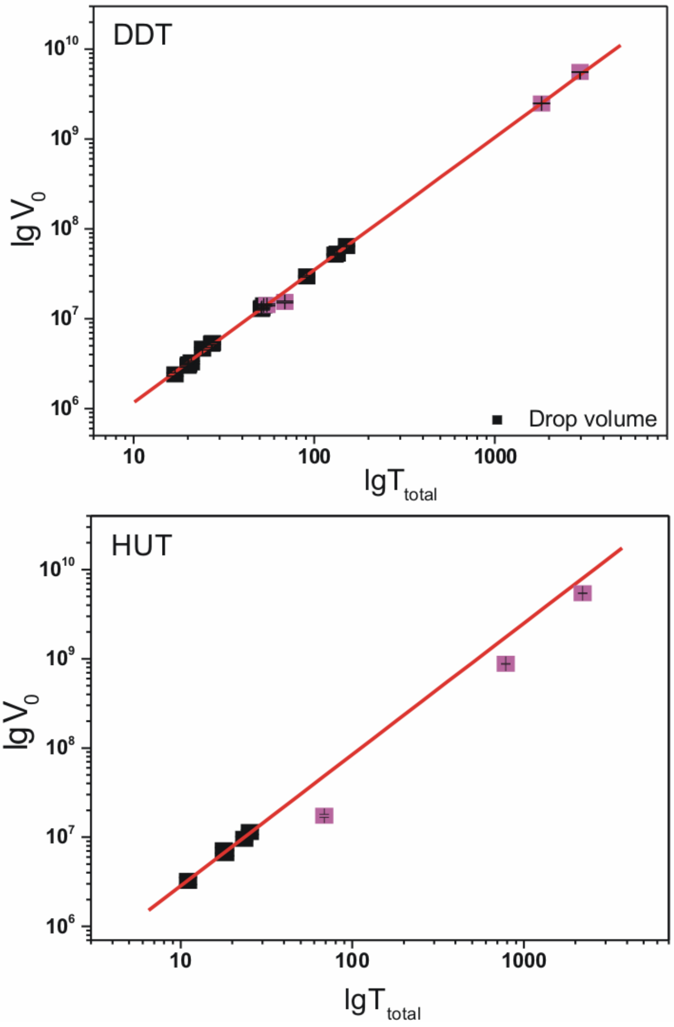

Figure 37 *The influences of drop sizes on the linearity of the initial volume versus the total evaporation time. The size of droplet ranges from nano-liter to micro-liter*

4.1.3.4. Influences of Pined three phase line on the evaporation dynamics

Based on above static measurement, the further profound studies of surface hydrophilicity can be achieved by looking at how the evaporation mode changes with different SAMs. It is shown in **Figure 28, 29** that an increasing tendency of pinning with X_{HUT} for m = 0 and the same for m ≠ 0.

However the effect of pinning is more pronounced for m = 0. The hairy surface for m ≠ 0 can counteract with pinning, maybe due to the flexibility of the long alkyl chain, no matter whether it is hydrophobic or hydrophilic. Thus the surface can arrange more favorable to the sessile water droplet to avoid generically unfavorable pinning effects.

Since pinning is more pronounced for hydrophilic surfaces as that of HUT, another pinning at the very end for HUT can be observed. For the other SAMs, a simple mixed-mode evaporation is found. For HUT it looks more complicated.

The plots of drop cap area and volume$^{2/3}$ versus evaporation time show such significant differences (**Figure 31**, **32**). Suppose that the pinning effect plays important role in the divergence of b value, a plot of A_s/V versus evaporation time is drawn (**Figure 38**). A_s/V is obtained from dividing drop cap area by drop volume$^{2/3}$. It is interesting to find that the slope of curves vary with surface hydrophilicity in the plots. At both end there are DDT and HUT SAMs curves, in between all the other SAMs curves arrange according to the increasing hydrophilicity.

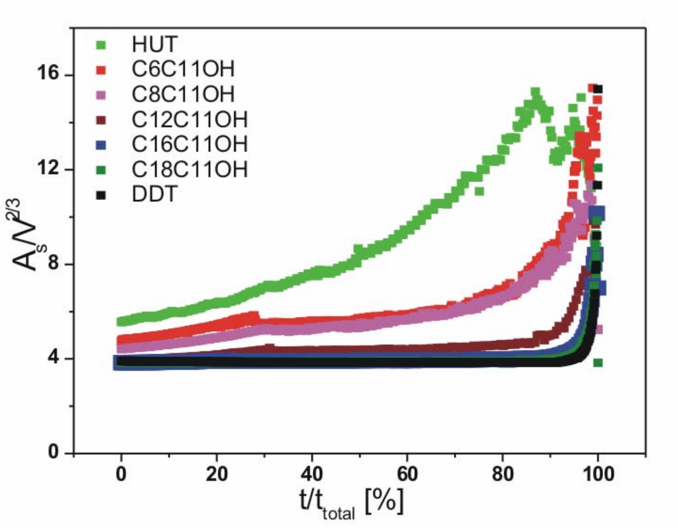

Figure 38 *A_s/V changes with evaporation time in 7 kinds of SAMs. The plots are for HUT (in bright green), C6C11OH (in red), C8C11OH (in magenta), C12C11OH (in dark read), C16C11OH (in blue), C16C11OH (in green) and DDT (in black)*

Theoretically, A_s and V can be can be derived from basic equations from **Eq. 4, 5,** and **7** as

$$A_s = \frac{2\pi a^2}{1 + cos\,\theta} \qquad \text{Eq. 36}$$

$$V = \frac{\pi a^3 (2 - 3 cos\,\theta + cos^3\,\theta)}{3 sin^3\,\theta} \qquad \text{Eq. 37}$$

Based on above two equations and A_s/V can be derived as a function of θ as

$$A_s / V = \frac{6.03}{(1 - cos\,\theta)^{1/3} (2 + cos\,\theta)^{2/3}} \qquad \text{Eq. 38}$$

For hydrophilic surface i.e. HUT, the pinning leads to the actual area (through which molecules evaporated) stay longer larger. The increased ratio – the actual area over the area of the evaporating sphere with the same volume enhances the evaporation rate. Area/volume becomes bigger which enable fast evaporation. For hydrophobic, i.e. DDT, the droplet radius decreases all the time and drop evaporates without pinning. The contact angle stays constant. This case can be explained by an evaporating sphere.

Quite often a fast decreasing of contact angle and contact radius with evaporation time in the rest of 10% of the total evaporation time is observed. So far this part is still an unsolved problem, because it is very complex and hard to find explanation. In trying to give a reasonable interpretation of this, assuming that the speed of the three phase line is affected by the surface properties, then a plot of speed of rim via contact angle in DDT and HUT SAMs is drawn in order to find the speed of rim dependence on the surface properties (**Figure 39**).

For the hydrophilic surface for instance HUT surface, at the very end of the evaporation process, the droplet pinned with three phase line. Due to the higher evaporation speed the droplet seems to be distorted. The drop evaporates with decreasing contact angle and the surface becomes more and more flat. The increasing cos θ against the surface tension and induces a big inward force. The drop starts to move and a higher rim speed is resulted. For hydrophobic surface like DDT, the contact angle is sensitive to the surface properties. At end of evaporation process the contact angle and contact radius decrease simultaneously without pinning. The movement of three phase line is induced by a dynamic contact angle which deviates from equilibrium state. The rim speed is slightly higher than zero, but quite steadily comparing to the case in HUT.

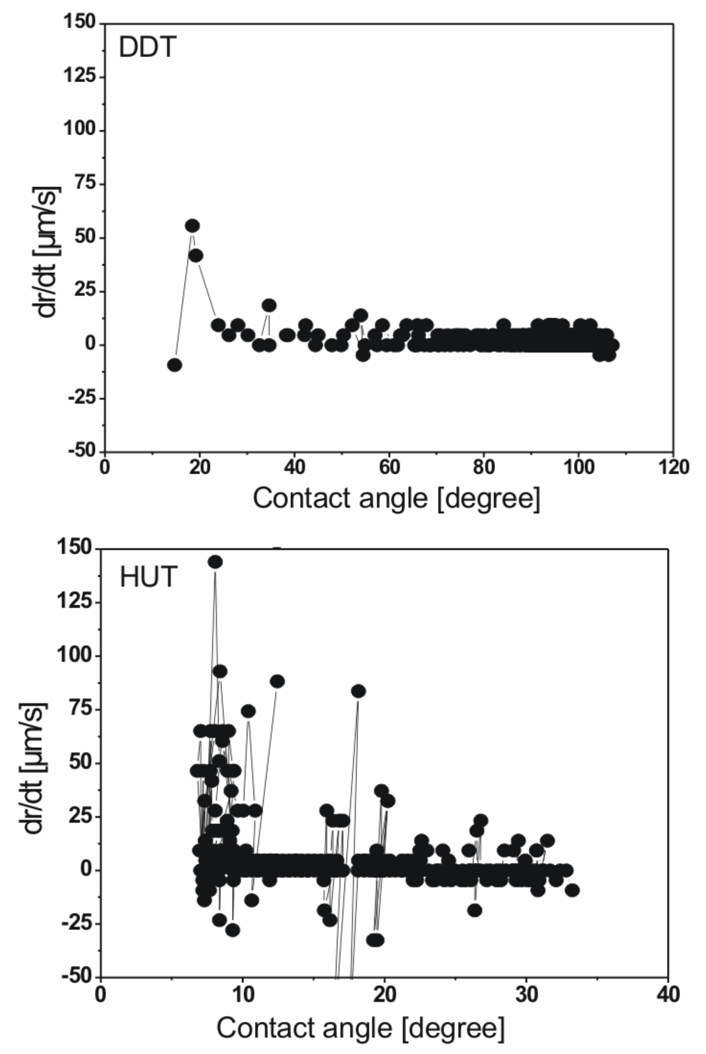

Figure 39 *Speed of rim versus contact angle in DDT (a) and HUT (b) SAMs*

4.1.3.5. The influence of droplet cooling effects on exponent b values

The fit of a single droplet actually is not able to provide sufficient information concerning the scaling exponent b values, despite a deviation can be clearly distinguished from the linear fit lines. Therefore a different analysis procedure was used to determine the exponent b. First, the droplets evaporate with different initial volume, thus different total evaporation time is obtained. The corresponding total evaporation time, t_{tot} was plotted in double logarithmic versus the initial volume (**Figure 33**). The resulting curve was fitted with a scaling law of the form $V_0 = a \times t_{tot}^b$, which follows the integration of the master **Eq. 9**. As a result the values of b are plotted versus m and X_{HUT} in **Figure 35** and presented in Chapter 4. A deviation of b from 1.5 is confirmed.

Assuming there is indeed an environmental influence to the drop evaporation. The changes of room temperature and humidity should be considered. In this studies, the maximum temperature changes was $\triangle T = 4°C$, which leads to $\triangle C = 0.0004\ Kg/m^3$ for pure water droplets. Assuming $f(\theta)/\beta^{1/3}$ is constant and using **Eq. 9**, the changes of a is as smaller as 0.5%. This implies that the temperature influences on a is only 0.1%/°C. Since the change is so small, the influence can be excluded.

This is also proved by the simulation results performed by Friedhelm Schönfeld at IMM, Mainz, who assumed a cooling effect in the droplet by the heat of evaporation takes place, including a Marangoni effect. The results show that the Marangoni effect is not significant and can be neglected. This is in good agreement with the other studies[62]. Furthermore the simulation suggests that the evaporation rate dV/dt decreases due to the cooling effect, suppose the temperature lower only 0.7 K. As a result the scaling exponent can be larger than 1.5. But the effect on b is much smaller than the determined value from the fits and it does not show a dependence on the surface energy (hydrophilicity) of the SAMs, i.e. the chemical properties of the surface. There must be another effect to explain the dependence for b on the surface density.

If the assumption of the $f(\theta)/\beta^{1/3}$ being as constant as 0.4 is questionable, the influence of it can be estimated by considering a hydrophiclic surface HUT SAMs. Since during droplet evaporation, the contact angle change from 40° to 20° and these values are far away from the angle where the $f(\theta)/\beta^{1/3}$ is constant. Therefore a calculation is made in assumption of $f(\theta)/\beta^{1/3}$ is equal to 0.52, $\triangle a$ is obtain as 0.14 comparing to taking $f(\theta)/\beta^{1/3}$ as 0.4. A higher deviation as 25% is resulted. Therefore this assumption is not realistic in this case.

4.1.3.6. The influence of the surface chemical compositions on evaporation dynamics

Either there might be air entrapped for m ≠ 0 or there might be a water film formed depending on the hydrophilicity of the surface, or there might be an influence of the rearrangement of alkyl chains[90, 92]. It was proved that such minute changes in surface functionality or roughness have profound influences on the droplet evaporation process, which dimension is many orders of magnitude larger than those of the changes.

For SAMs with $m > 0$, the long terminated-methyl group can protrude over the shorter in plane hydroxyl-terminated chain, thus the stretching of methyl chain is possible when surface is covered by solvent. The water layer will preferentially form on the surface, because the surface is covered by hydroxyl group whose alkyl chain is comparably longer than the alkyl chain containing methyl group. The water molecules bind the OH group by the means of hydrogen bond to form a continuously water layer on the whole area, thus a prewetting water layer is generated[90] (**Figure 40**). If air is entrapped the heat exchange becomes worse and the cooling of droplet is stronger and this leads a slower evaporation rate.

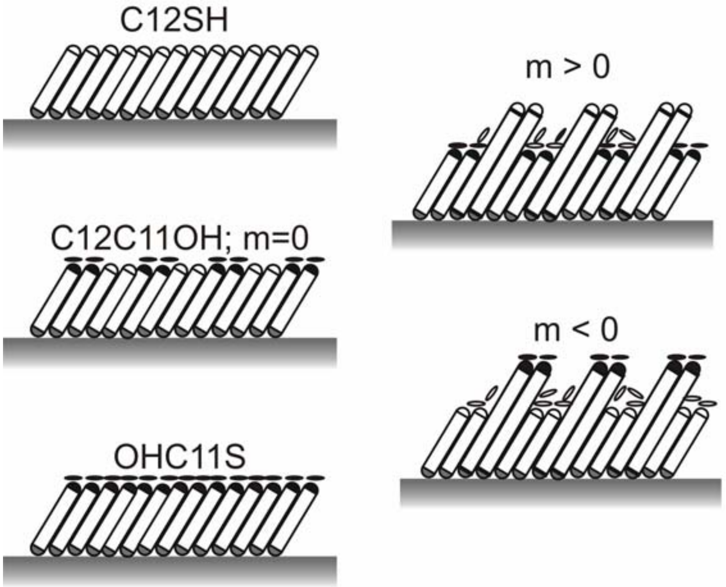

Figure 40 *A water layer tends to cover on the self-assembly monolayer surface due to the hydrogen bond formation. The more OH group exposure to the air, the more water molecular can bind onto the surfaces.*

Whereas for m < 0, the long hydroxyl-terminated chain prevents the stretching of methyl-terminated chain and it is called cage effect. Air is trapped inside of void between these two terminated groups. If there is a water film, it can be expected to be more pronounced on a more hydrophilic surface, as for HUT, for example. The evaporation model must be modified as indicated in **Figure 40**.

Comparing the classic model the evaporation rate of droplet may increase due to the water layer (**Figure 41**). The thin water film might affect the evaporation rate close to the meniscus and thus might lead to a different scaling.

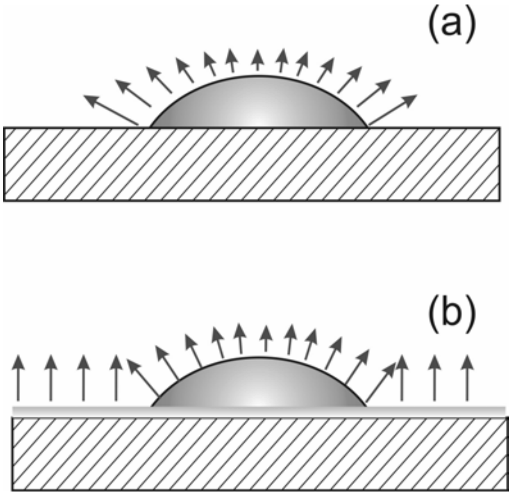

Figure 41 *Principle effect of water film on the evaporation rate (b) compared to the classical evaporation model*[33] *(a)*

4.2 Microstructure formation of polymer surfaces by deposition of solvent droplets

In order to understand how many potential influences affect the microstructures formation, in this section two kinds of techniques –syringe deposition and ink-jet technique are used. With these techniques the studies of microstructure formation are carried out by the investigation of two types of parameters – process parameters (speed of deposition, delay and initial volume) and intrinsic material parameters (molar mass and different polymer/solvent combination). The experiment with syringe system and ink-jet technique can be found in the section of 4.2.1~4.2.2.2 and respectively.

4.2.1 Influence of process parameters on the structuring

In principal two types of microstructures as U-shaped and V-shaped microstructures can be obtained by using syringe deposition (sessile drop)[65] and ink-jet deposition (falling drop)[39]. From these results one can assume that the kind of the deposition of a droplet on top of the polymer surface has a big influence on the microstructuring. The ink-jet technique deposits the droplets fast without contact between surface and delivery system. In contrast, the syringe technique manipulates the drop sizes, while it is already in contact with polymer surface. This offers the possibility to influence the initial drop formation prior to evaporation. Usually, the drop is deposited on the polymer surface with increased size, and finally the syringe tip is removed from the droplet. By changing the approach speed, the retraction speed and the duration during the drop formation, the relevance of the initial drop formation process for the microstructuring of the surface can be evaluated with the syringe deposition. The changed initial drop volume leads to different kind of microstructures shape due to the different evaporation process governing by the surface area/volume ratio. Subsequently different dissolution time scale dominates the polymer dissolution, swelling process etc.

With the syringe technique, the process parameters can be investigated by a reconstructed homemade experimental setup. This allows a movement of substrate stage. Three major influences as speed of deposition, delay and initial volume will be studied and elucidated individually.

4.2.1.1. Dependence of microstructures on drop initial volume

Here the influence of initial volume on the formation of microstructures is studied. Different drop volumes were generated at syringe tip, while the drop height – distance between drop apex and syringe tip was varied accordingly. The evaporation was then balanced by a continuous flow out of syringe, controlled by a motorized syringe pump. After the pendent drop has been formed, the substrate is approached until drop is placed on the polymer surface. After drop deposition, the substrate is retracted to its original position. Both approach and retraction speeds are set to the same value of 11 mm/s here. First the droplet spreads on the polymer surface within the first 87 ms and then evaporates with a pinned rim until it dries.

The initial contact angles are between 30° and 40°. The total evaporation time of a droplet is ~5 seconds. Finally, the dried microstructures are obtained in the range between 360 µm and 750 µm. The height profiles show either V- or U-shaped crater-like structures (**Figure 42a**). Typically, the microstructures with diameter bellow 600 µm are V-shaped and those above 600 µm U-shaped. The height profiles obtained after keeping samples in vacuum for 7 days are shown (**Figure 42b)**. The microstructures sink into the flat substrate surface with persistence of the initial shape and aspect ratio owing to solvent evaporation from inside the polymer.

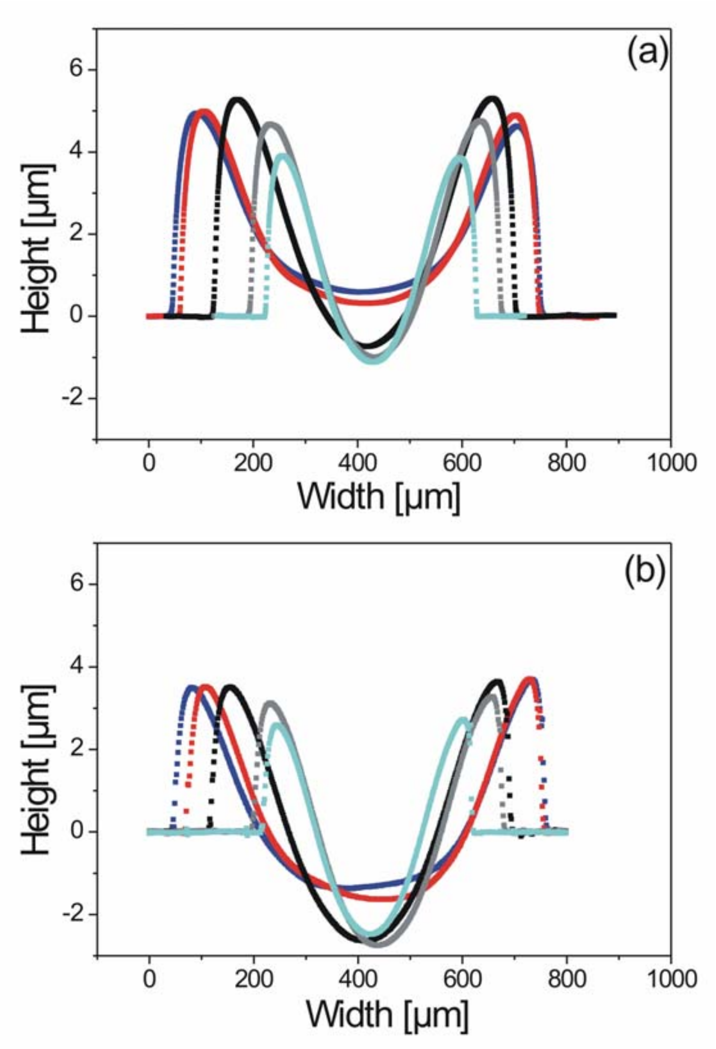

Figure 42 *Representative height profile of convex microstructures in PS surface after evaporation and deposition of a toluene drop after 2 h under ambient conditions (a), after 7 days in vacuum (b). The drop deposition was performed with the approach and retraction speed of the substrate being 11µm/s.*

The removed net volume is calculated, assuming that the net volume is the difference between a cylinder part and a parabolic part in the plane images (Sketch in **Figure 43**). The removed solvent volume is derived from the volume difference before and after drying. A linear relation between the removal of solvent volume and microstructure width can be found (**Figure 43a**). Apparently the larger the microstructure width is, the more solvent can be removed. However, the percentage of removed solvent volume declines non-linearly with width of microstructures (**Figure 43b**).

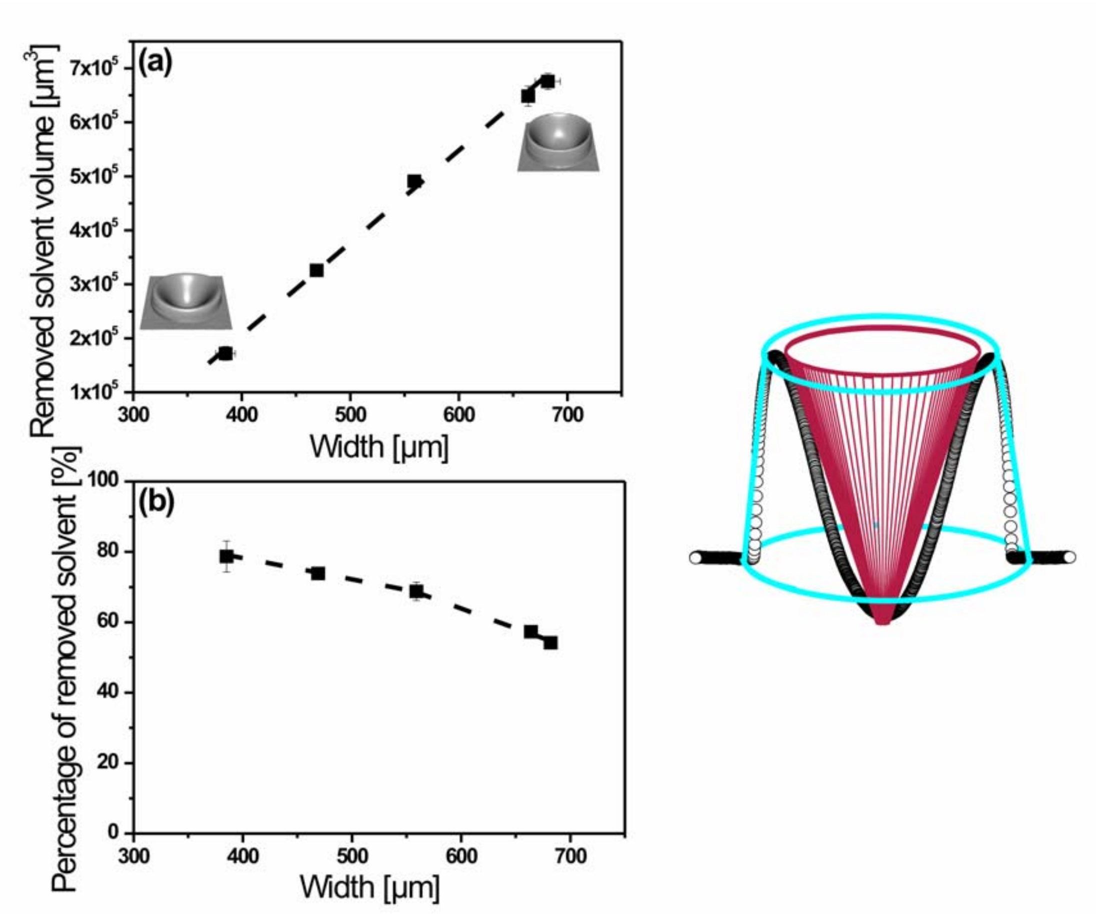

Figure 43 Removed net volume (a) and percentage volume changes (b) of the microstructures. The volume is calculated as described in the text and a sketch on the right side of this figure. The two 3D images represent two different microstructure sizes with V-shape (left side in a) and U shape (right side in a). The percentage of removed solvent volume is obtained by dividing the removed solvent volume with the volume of the non-dried microstructure.

4.2.1.2. Dependence of microstructures on approach and retraction speed

The shape of resulting microtopologies depends on the approach speed and retraction speed of the substrate and the delay between the two movements. To investigate the influence of these process parameters, two different approach and retraction speeds, 10 µm/s and 9 mm/s, were chosen with a delay time of 0 s. For the highest speed of 9 mm/s, the rim of microstructures forms above substrate surface whereas the middle part of microstructures is below the flat surface. A deep concave structure as V-shaped is formed. At the lowest speed of 10µm/s, a convex structure is found **(Figure 44)**. Consequently, by simultaneously decreasing, both the approach and retraction speed, the microstructures can be tuned from concave structure into convex structure.

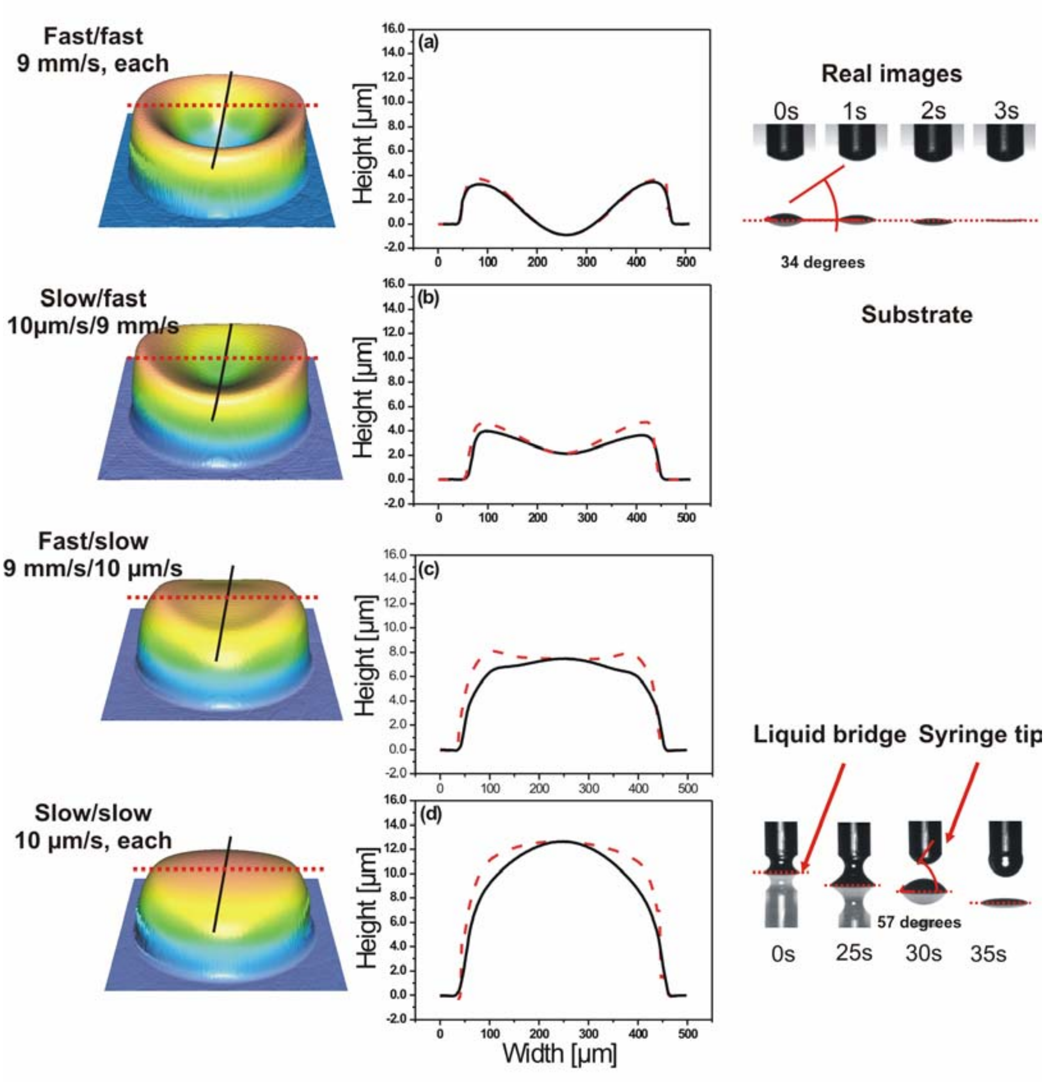

Figure 44 Microstructures in PS surface after deposition for a toluene drop from a syringe tip and after evaporation as described in Chapter 3 (experiment section) for different approach and retraction speed of the substrate (delay time = 0 s in all cases). The speeds are indicated on the left column. The height profiles along the 3D topologies were taken and plotted for fast/fast (a), slow/fast (b), fast/slow (c), and slow/slow (d) process speeds. On the right two representative optical images are shown. For fast speeds the time resolution was too poor to image the liquid bridge between tip and polymer substrate.

The total time needed to obtain convex structures is about 35 s, of which the first 25 s is used to form a liquid bridge and the rest 10 s for drop evaporation time, whereas only 3 s evaporation time is needed to obtain concave structure formation. The initial contact angle after syringe tip leaves the droplets is 34° for highest speed**,** 55° for slowest speed. A liquid bridge is found for the slowest speed.

4.2.1.3. Dependence of microstructure formation on delay time

So far the delay time, i.e. the waiting time between approach and retraction, was kept as short as possible. Its influence on the microstructure is studies by changing it from 0 to 1000 ms (**Figure 45a**). Delay time larger than 1000ms leads to a sticking of polymer. Subsequently, thin PS fibers are created after the separation of tip and polymer substrate.

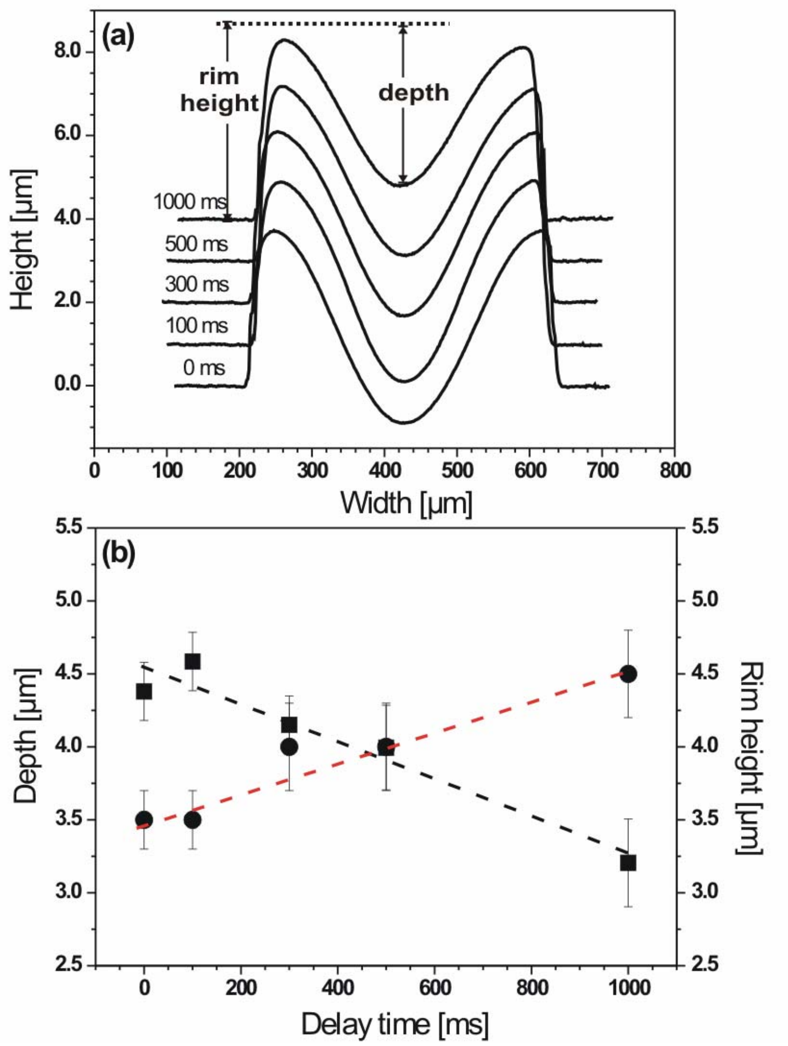

Figure 45 Height profiles of micro-topologies in a PS surface after evaporation of deposited toluene droplets (contact mode) for different delay times between approach and retraction, both with 11 mm/s, and (a). The corresponding depth (■) and rim height (●) as defined in (b) versus delay time. The black and red dash lines are used to guide the eyes.

With increasing delay, the topologies move upward away from the polymer surface, while maintaining their original concave shape. The rim height varies with 3.5 µm, 3.5 µm, 4 µm, 4 µm and 4.5 µm respectively. The depth decreases from 4.6 µm to 3.2 µm with increasing the delay (**Figure 45b**) from 0s to only 1 s.

4.2.1.4. Discussion of influences of process parameters

As described in Chapter 2, the concentration of polymer solution affects significant on the microstructure formation. It was confirmed that the concentration changes will lead to the transition of microstructure shape from convex structures to intermediate structures and then to concave structures (**Figure 14**). L. Pauchard found that the convex structure formed at a higher concentration solution of 0.4 g/g, whereas the concave structure formed at a lower concentration of 0.2 g/g for Dexane aqueous solution. However M. Doi observed the convex structures for a more dilute concentration and the concave structures for a higher concentration, when the concentration of silica solution increased from 0.05 wt% to 0.25 wt%. These results show the concentration dependence of microstructures formation despite the results are somehow contradictive [24, 35]. In this work, the effort is made to understand how the concentration influences the microstructure by process parameter changes.

The convex structures are already found on the no-dissoluble substrates by the deposition of polymer solution drops and the formation is attributed to the concentration effect and evaporation rate as well. The influence of initial contact angle and humidity on shape of microstructures can be explained as a slower evaporation rate. The convex structure arising from the higher contact angle can be due to the lower evaporation rate since the surface area/volume is smaller for a higher contact angle. For the humidity, the increasing humidity leads to a lower evaporation rate, thus a convex structure formed[26].

In this study the most astonishing observation is that the convex can be achieved by decreasing either approach and retraction speed simultaneously, or the retraction speed alone. The convex structures observed here occurs owing to an increased polymer concentration, which leads to gelation. When the retraction speed is lower, polymer will dissolve into the droplet. The concentration can be increased by keeping the polymer surface longer in contact with liquid prior to the evaporation. Therefore, the convex structure occurs especially if the retraction speed is decreased. In contrast to the approach, there is a liquid bridge between syringe and polymer surface during the whole retraction. Thus, the amount of dissolved polymer is sensitive to the changes of the retraction speed.

With the technique presented here, the contact time between liquid and polymer can even be increased more elegantly by the delay time between substrate approach and retraction. Thus by controlling the delay, the shape can be tuned in a more refined way. The reason for this might be the dynamics of the liquid bridge. When the actuator is moved, the liquid bridge is compressed during the approach and stretched during the retraction. This might impose an additional flow in the liquid, leading to a higher dissolution rate. Thus, a gel-like state and therefore a convex topology after solvent evaporation are more likely. In contrast, imposing a static delay without moving the liquid bridge decreases the dissolution rate of polymer and a fine-tuning of the micro-shape can be achieved. These ideas suggest that it is reasonable to distinguish between a static and a dynamic contact time.

Due to changed initial drop volume, two types of microstructures as V- and U-shaped are formed. A V-shaped surface topology in the polymer is generated by the flow of the toluene at the tip of the syringe[94]. If the diameter of drop is larger than 600 µm, more solvent are added on to polymer surface and solvent instantly spread over a larger surface area, a higher area/volume is leading. Basically the duration of the evaporation time after the drop deposition is longer and solvent are able to distribute evenly inside of initial formed well. Despite the long evaporation time, the mass transfer of higher viscous liquid from center to the far away rim by coffee ring effect becomes impossible because of the increasing length scale. This finally gives rise to a lowered rim height and depth comparing to V-shaped structures. Conclusively the artifacts from the formation of the droplet are more readily smoothed out, providing a U-shaped structure.

Drying process has no significant influences on the principal microstructures shape, since the shape and aspect ratio of these microstructures did not show any differences before and after drying. For V-shaped and U-shaped microstructure, after drying the trapped solvent is removed partially and the removed solvent volume increases linearly with the width of microstructures from 360 µm to 750 µm, whereas the percentage of removed solvent volume decreases from 78% to 53% with increasing microstructures width. The bigger droplet was, the more difficult is the removal of the solvent from the polymer (**Figure 43**).

The rest of toluene is most likely to remain inside of the swollen polymer. Thus it can be concluded that only partially trapped toluene can be removed by any drying process since the solvent uptake is an irreversible process.

The reason for resulting concave structure in most of cases can be due to the major three effects. (i) concave structure from a similar effect like that for coffee ring effect. First there is softening of the polymer below the droplet, away from the polymer surface directly below the apex of the droplet, simultaneously, the evaporation rate is faster. (ii) There is distortion of the rim. This might come from entropic contribution of the oriented polymer chains owing to the extrusion process. As a test, polystyrene with a narrow molar mass distribution was stretched 150%. 200%, 250% and exposed to a droplet of toluene (**Figure 46**). Again a rim –modulation occurs together with ripple in the microstructure. This is a typical structure occurring for stretched polymers if the surface properties are different from the bulk polymer and a relaxation of previously oriented polymer chains is initiated, e.g. by exposure to solvent or by annealing.[95-99] (iii) extraordinarily, the high rim leads to diffusion of solvent into polymer surface while concave structure in forming. First the solvent leads to softening, then to concave structure formation, then to swelling of the center for the structure, which is close to the apex, and finally more and more swelling of the rim, which is exposed more to the pendent drop.

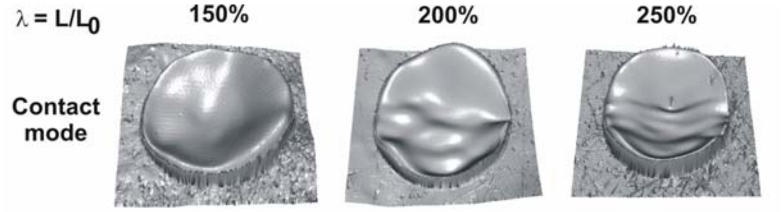

Figure 46 *Toluene drop deposited on the stretched PS surface with stretching ration of 150%, 200%, 250%. λ is the stretch ratio, L and L_0 are the length before and after stretching.*

4.2.2 Influences of intrinsic material parameters on microstructuring

Generally, the shapes of microstructures are all in concave in the results of section 5.2.1. To obtain other types of microstructure it is not realistic to rely only on changing process parameters. Since the formation of microstructures is also dependent of several other intrinsic parameters, for instance concentration. The different solution concentration can significantly alter the microstructures shape from concave into convex in no-soluble system[24, 35]. This concentration dependence of microstructure is confirmed on the soluble system as well. To vary the concentration on the soluble material surface can be achieved by dissolving the material into the solvent when drop is in contact with substrate. There are several possibilities for instance, to vary kinds of polymer, polymer molar mass, solvent etc. The concentration in this case will increase all the time due to the initial dissolution process and solvent evaporation process. Consequently, dissolution process and swelling process becomes important. In this section, the influence of three intrinsic parameters, kind of polymer, molar mass and solvent are studied.

4.2.2.1. Influence of polymer molar mass on microstructures

In this chapter the influence of polymer molar mass on the microstructure are investigated. The molar mass can affect different steps in the structuring of the polymer substrate, for instance the dissolution and gelation process, because they are solvent penetration rate and disentanglement rate dependent (Chapter 2). The diffusion coefficients of the polymer chain movement inside of solvent are dominated by the polymer chain length- the polymer molar mass. Therefore I used PS substrates with a narrow molar mass distribution (Chapter 3).

To understand the influence of the molar mass on the final structure, PS with different molar mass from 20.9 kDa to 1,400 kDa were studied by deposition of toluene droplets in contact mode. The approach and retraction speed of the substrate were fixed at highest speed, with no delay between these two movements. The droplet diameter is around 400 µm. After droplet deposition, the samples were allowed to dry at ambient conditions for 2 hr before imaging their 3D topology with µsurf microscopy. The microstructures change with the molar masses (**Figure 47**).

A pile-up of material appears for a low molar mass below or equal to 24.3 kDa. For 29.6 kDa, a dimple occurs in the center of the pile-up. These structures have been found for process parameter studies in section 4.2.1 due to a higher polymer concentration. However the simple case of concave structure due to coffee ring effect is found on the PS with molar mass between 90 kDa and 210 kDa. Asymmetric concave structures are found for PS with molar mass above 339kDa, whereas random roughness surface are observed for the one with molar mass above 1,000 kDa.

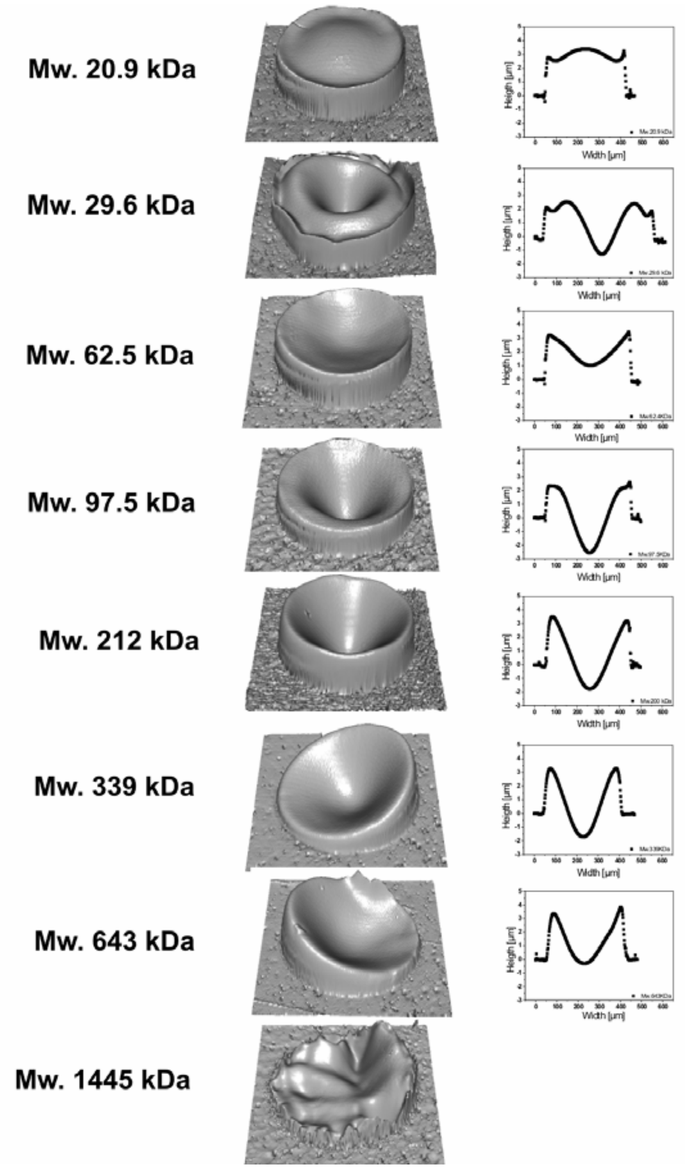

Figure 47 *Typical surface plots (left) and cross-sections (right) of microstructures left by toluene drops on polystyrene substrate with different molar masses 1-2 h after evaporation. The drops were deposited on the polymer substrate with a syringe and the resulting microstructures were imaged with a confocal white-light microscope. The height profiles are shown. y- axis is in the range of 2 ~ 5 µm and x- axis in the range of 50 ~ 650 µm*

The surface structures left by evaporating sessile drops on a polymer surface showed a steep ridge at the periphery after drying (**Figure 47**). Typically, this ridge was 3 µm high. On low molar mass PS ($M_W \leq 24.3$ kDa) an evaporated toluene drop left a protrusion or dot-like structure in the center, which filled the inner part of the ridge and rose to roughly 3-4 µm height. Between the ridge and the dot a depression was observed.

With increasing molar mass the center of the dot decreased in height and a central depression for 29.6 kDa or molar mass higher than this value was formed. For $M_W = 97.5$ kDa the bottom of the crater was even below the original surface and reached a depth of up to 3 µm. When further increasing the molar mass, the depth of the craters decreased until at 1445 kDa they disappeared completely. In addition, a new characteristic feature was visible: the craters became asymmetric. With increasing molar mass the degree of symmetry and the length scale, on which the asymmetric feature appeared, decreased. At $M_W = 339$ kDa the outer ridge typically showed a height modulation; it was significantly higher on one side than on the opposite one. The length scale of the asymmetry is of the order of 400 µm. At $M_W = 1445$ kDa the crater is filled with an irregular pattern of small depressions and protrusions with a width of typically 50 µm.

To relate the droplet parameter within the evaporation process, I investigate now the evaporation process which normally takes ~5 s. During this period, the toluene evaporated, with constant contact radius and decreasing contact angle (**Figure 48a-b**). A spreading of drops is observed at the initial evaporation for all the cases.

To get rid of the influence from the dissolution and the polymer in the droplets, I placed toluene drops on a non-soluble, hydrophobic silicon surface silanated with trichlorooctadecyl silane (OTS). In this case the toluene drops evaporated with a constant contact angle of $\theta = 32°$ and diminishing contact radius. The evaporation rate, that is the decrease in solvent volume per unit time, $\left|dV/dt\right|$, on the silicon wafer was higher than on the polymer surface. The plot of $V^{2/3}$, with V being the volume of the toluene drop, versus the evaporation time t, provides a straight line (**Figure 48c-d**). This linear decrease of $V^{2/3}$ with time is well known[10, 52, 54, 58].

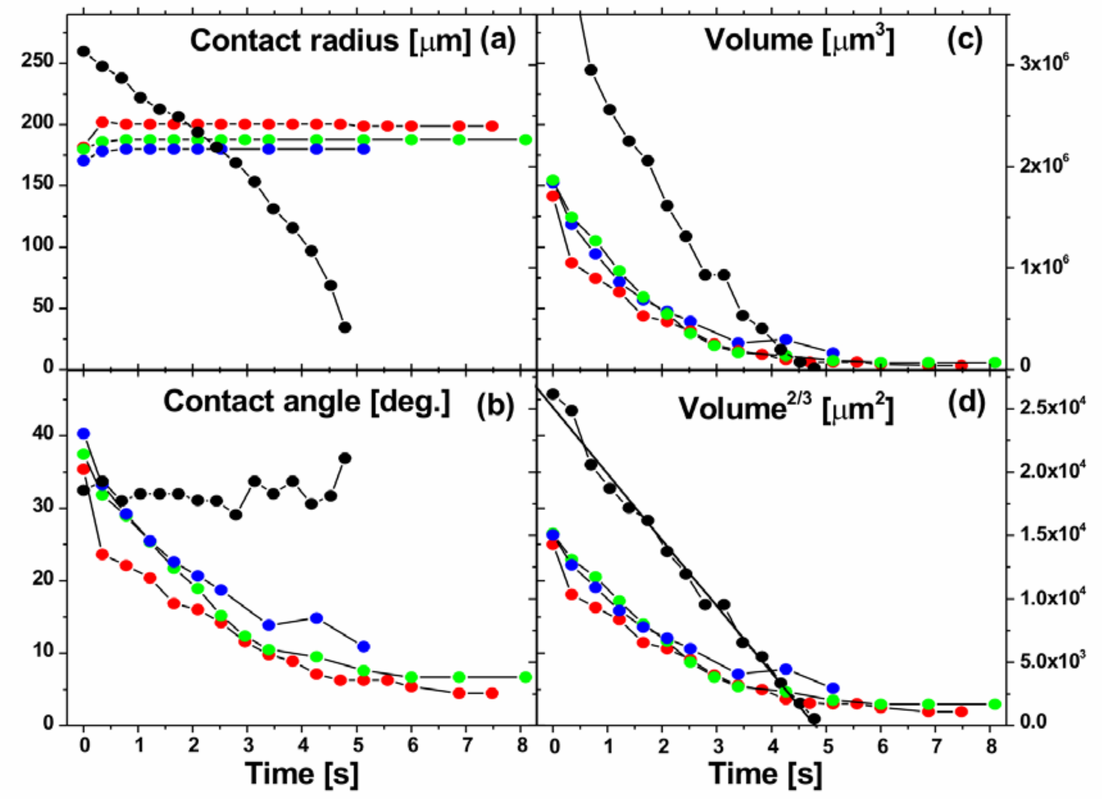

Figure 48 *Contact radius, contact angle, drop volume V, and $V^{2/3}$ versus time for a toluene drop evaporating on a polystyrene surface with MW = 20.9 kDa (red), 210 kDa (bright green), and 1445 kDa (blue). For comparison the results obtained with a silanized silicon wafer are shown (black).*

4.2.2.2. Cracks formation in the low molar mass PS

In some samples a crack formation was observed. This observation might lead to a better understanding of the desiccation process during the microstructure formation. In this study, toluene drop was placed on compressed PS sample surface in a syringe system. Micro-size droplets are placed on a PS substrate, which has a molar mass from 20.9 kDa to 29.6 Da. The Mexican hat shape microstructure is found for molar mass from 20.9 kDa to 24.3 kDa, whereas the dim in the center is found for 29.6 kDa. Cracks were observed one day after preparation under ambient condition for the molar mass below 24.3kDa. No cracks were found on the sample with molar masses above 29.6 kDa even after keeping sample for 2 month. The SEM images show that the cracks appear either in the middle of structures or along the structure rim, especially for molar mass of 20.9 kDa sample (**Figure 49**).

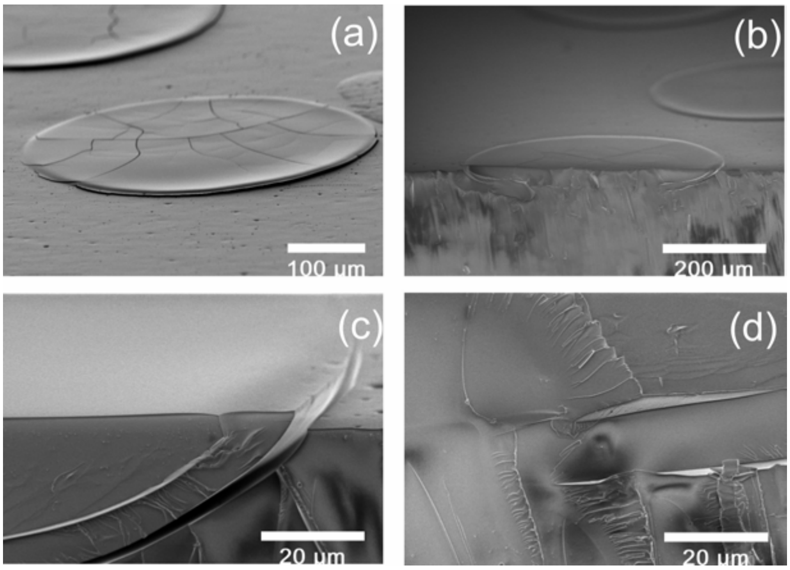

Figure 49 *SEM images of microstructures of toluene drop in polystyrene (M_W=20.9 kDa) 4h after the drop was placed on the surface. A original cracks occurs inside of dried drop (a). To see the lateral structure, the substrate was cut vertically (b). A enlarged side views are shown in (c) and (d).*

In some samples the whole part of dried material inside of the structure could be removed from the PS bulk substrate instead of irregular crack formation (**Figure 50**).

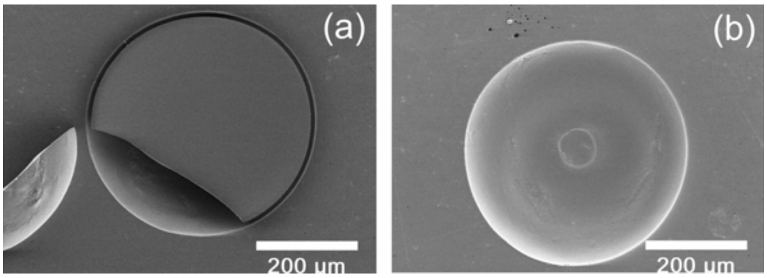

Figure 50 *Ring-shaped crack in PS 20.9 kDa after one day at ambient condition. With a cover (a) and after removal of the cover (b)*

4.2.2.3. Microstructuring of polymer surfaces with ink jet technique – molar mass dependence

In the previous section the study of microstructure in dependence of PS molar mass was carried out by a syringe system. As mentioned before the microstructures can be also influenced by using different techniques [39, 65]. In this part, the experiment is performed with ink jet technique, as a reference, PS/toluene system was used. Furthermore a second system PEMA/ethyl acetate was selected for the investigation.

When depositing solvent drops on polymer surfaces by a nozzle in the ink jet technique the optically visible evaporation process typically takes 0.3 s. During evaporation the contact radius is constant and the contact angle changes (**Figure 51**).

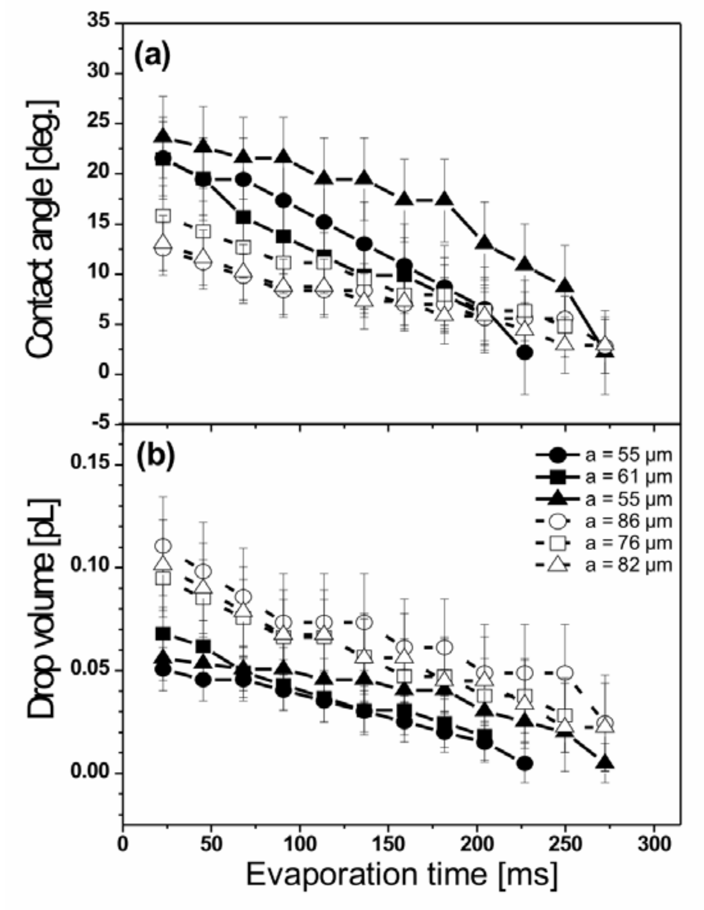

Figure 51 *Contact angle (a) and drop volume (b) versus evaporation time from three toluene drops evaporating on PS (M_W = 210 kDa, open symbols) and three ethyl acetate drops evaporating on PEMA (M_W = 142 kDa, filled symbols). The respective initial contact radius a are indicated in the legend in (b). They stay constant throughout the whole evaporation.*

The contact angle of toluene on PS of initially 14° is lower than the contact angle of ethyl acetate on PEMA ($\theta = 23°$). Accordingly the contact radius of toluene on PS is larger ($a \approx 80$ µm) than that of ethyl acetate on PEMA ($a \approx 56$ µm). The initial volume is ~0.1 pL for toluene on PS and ~0.06pL for ethyl acetate on PEMA. Each experiment was repeated three times under same conditions. The derivation of the contact angle is 3° for both systems.

For PS a predominate dependence of polymer structures on the PS molar mass and the numbers of solvent droplets are found (**Figure 52**). PS molar mass ranges from 20.9 kDa to 1444 kDa.

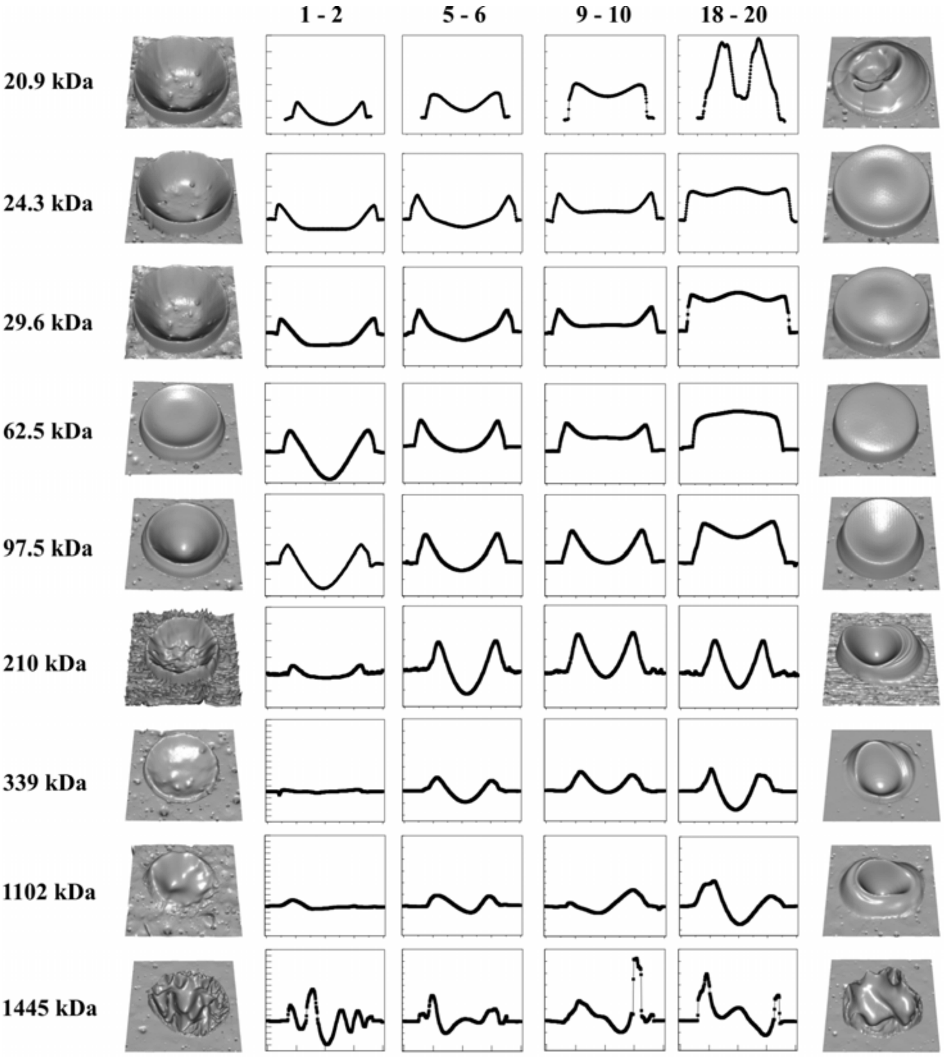

Figure 52 *Surface topology (left and right) and cross-sections (middle) of microstructures left by toluene drops deposited by the inkjet on polystyrene with different molar mass 1-2 h after drying. For the cross-sections the ticks are spaced 1 µm vertically and 50 µm horizontally. The four columns of cross-section of microstructures were produced with 1-2, 5-6, 9-10, and 18-20 drops deposited at intervals of 0.5 s on the same spot. The topology on the left and right are produced with 1-2 drops and 18-20 drops, respectively.*

The more droplets are continuously placed on the same spot, the higher becomes the rim of the structures and smoother appears on the surface of the polymer which came into direct contact with liquid.

The surface topologies on the left are concave structures for PS molar mass below 1102 kDa. A modulated structure is found only for 1444 kDa PS surface. However the surface topologies on the right changes with slightly changed PS molar mass. For PS with a molar mass of 20.9 kDa, a structure with a dimple in the center is found. For PS with molar mass of 24.3 kDa and 29.6 kDa, the convex structure is observed. The concave structures are found for a wide range of PS molar mass from 62.5 kDa to 210 kDa. As the PS molar mass rises above 339 kDa, the asymmetric irregular structure appears.

For all molar mass PEMA, the flat box-shaped structures are formed irrespective of PEMA molar mass. However these structures become much smoother with increased number of drops deposited (**Figure 53)**.

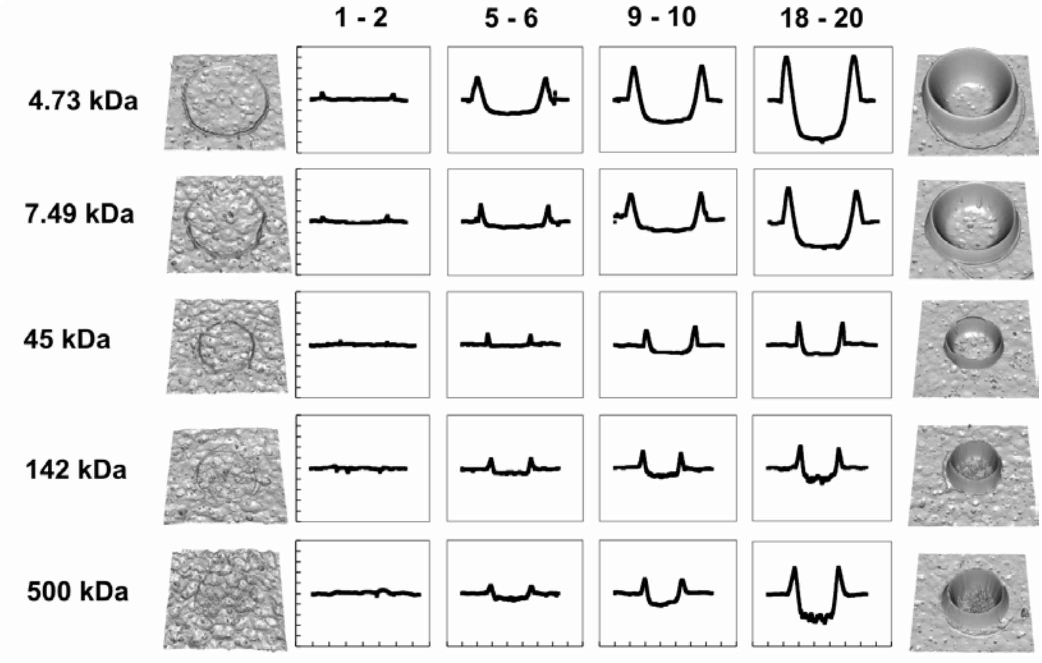

Figure 53 Surface plots (left and right) and cross-sections (middle) of structures left by ethyl acetate drops deposited by the ink-jet on poly (ethyl methacrylate) with different molar mass 1-2 h after drying. For the cross-sections the ticks are spaced 1 µm vertically and 50 µm horizontally. The four columns cross-section of microstructures were produced with 1-2, 5-6, 9-10, and 18-20 drops deposited at intervals of 0.5 s on the same spot.

In cross-sections on evaporation structures in PEMA this appears as a “noisy” line at the bottom of the craters for M_W= 142 kDa and 500 kDa. For lower molar masses the bottom of crater appears smooth.

The depth of the craters (as counted from the mean height of the rim) first decreases with increasing molar mass (Figure 54a) for molar mass lower than 45 kDa and then increase for molar mass higher than 45 kDa. In addition the width of crater in PEMA shows a dependence of molar mass (Figure 54b). The width decreases with increasing molar mass below 45 kDa, whereas keeps as constant for the molar mass above 45 kDa.

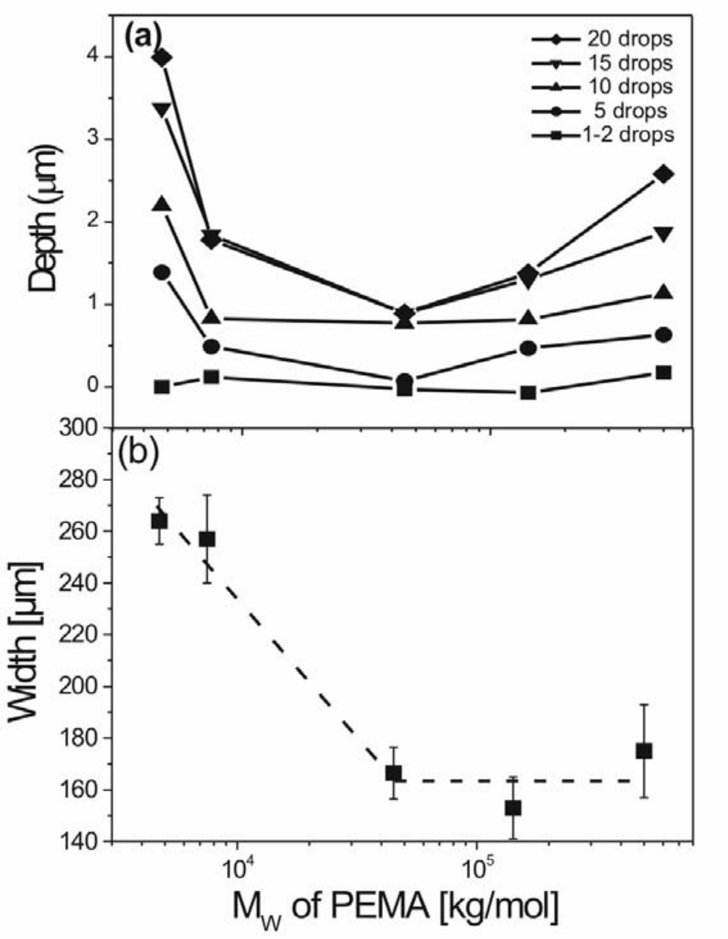

Figure 54 Depth (a) and width (b) of craters left on PEMA after evaporation of different numbers of drops of ethyl acetate. The depth is the height difference between the depression in the center of the crater and the mean height of the rim. Dependence of width of craters on molar mass for PEMA after drying of ethyl acetate droplets. The dashed line is a guide to the eyes.

With the depth and width as an additional criterion all five samples could be discriminated and the molar mass could be determined. The depth is sensitive to low molar mass. The accuracy is, however, not as good as that of other methods. Based on the variation of the parameters from experiment to experiment the molar mass can be estimated with an accuracy of a factor of two.

Comparing the evaporation structures left by different combinations of solvent and polymer some characteristic features are generally observed, while others are qualitatively and quantitatively different and depend on the specific combination. One characteristic features generally observed from toluene drops evaporating from PS (**Figure 52**) and ethyl acetate evaporating from PEMA (**Figure 53**) are crater-like rings with a depression in the middle. To discriminate the higher molar masses another characteristic feature, which is observed for PEMA and PS, can be utilized: the evaporation structure becomes asymmetric and irregular. Morever a rough surface is found in the center of most of the PS and PEMA structures for molar mass higher than 1,000 kDa and 45 kDa, respectively.

4.2.2.4. Discussion of influences of intrinsic material parameters

In addition to process parameters studied in the previous section, the intrinsic material polymer parameters as the molar mass of polymer and the polymer/solvent system have an influence on the final microstructure formation.

4.2.2.4.1. Evaporation dynamics of toluene on PS and silicon substrates

The wetting property of PS by toluene is observed. A further spreading of the three phase line is observed 87 ms after the toluene drop is deposited on the PS surface. The contact radius of droplet increases ~25 µm (**Figure 48**), thus the spreading time can be calculated by $\tau_s = \rho \cdot V^{2/3}/\eta$. Here, the volume of the drop is around 3.2x10^{-12} m^3. ρ is the density of solution and η is the viscosity of toluene. Assumed that ρ is the density of toluene 865 kg/m^3, whereas η is 0.59 m·Pa·s. Thus τ_s is ~32 ms[32, 39]. After that the pinned droplet evaporates with constant contact radius. Subsequently polymer dissolves into solvent and accumulates at the three phase line, which leads to a rim formation Usually a concave structure is formed[36, 39].

The formation of microstructures can be understood in the study of evaporation dynamics as shown in section 4.2.2.1 (**Figure 48**). A comparison of the evaporation process of a toluene drop evaporating on a hydrophobic non-soluble substrate OTS grafted silicon and a soluble substrate PS is performed. Therefore, an influence of the dissolution process can be excluded from the solvent drop evaporation on non-soluble surface. A CCA mode is observed despite the contact angle is as lower as 30°. This is not surprising since the pure water drop evaporation on OTS-si surface has CCA mode as well. The dissolved material, however, changes the type of evaporation mode. A CCR is observed for all of PS with different molar mass. The linearity of $V^{2/3}$ versus t is again confirmed in pure toluene evaporation but not for the latter case. As evaporation of pure solvent and polymer solution are such different process, the evaporation rate should change accordingly. Thus an influence of the different vapor pressure changes should be considered.

For pure toluene evaporating on the OTS-si surface under a known experimental condition, the diffusion coefficient can be calculated. β and $f(\theta)$ as functions of the contact angle θ can be calculated with **Eq. 10** and **Eq. 11** and obtained as $\beta = 0.0658$ and $f(\theta) = 0.376$ for $\theta = 32°$ in the evaporating of a toluene on silicon wafer surface. From the slope of $V^{2/3}$ versus t and by inserting $P_0 = 3.79$ kPa, $M = 92.13$ g/mol, $\rho = 866$ kg/m^3 at 25°C into **Eq. 12** a diffusion coefficient $D = 8.1\times10^{-6}$ m^2/s is obtained. This agrees well with a value of 8.0×10^{-6} m^2/s measured previously in tube and sessile drop evaporation experiments[56].

The reduction in the evaporation rate on PS as compared to that on silicon can be understood with **Eq. 9** [10], R_s is the radius of curvature of the drop, which depends on the contact angle and contact radius. The reduced rate of evaporation on PS is attributed to a decrease in the vapor pressure. The vapor pressure P_0' of the solution depends on the amount of dissolved PS. The relative vapor pressure, that is the vapor pressure calculated with **Eq. 12** divided by the vapor pressure of pure toluene (P_0 = 3.79 kPa), is plotted versus evaporation time in **Figure 55**.

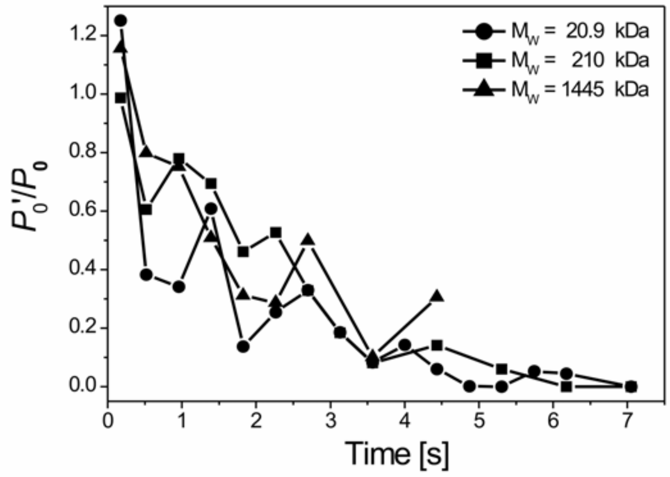

Figure 55 *Vapor pressure of toluene drops evaporate from polystyrene surfaces with different molar mass versus time.*

As more and more PS is dissolved in the toluene, P_0' decreases[100]. It goes to zero as the volume fraction of toluene in the toluene-PS mixture tends to zero. At the end of the evaporation process little toluene is dissolved in a lot of PS and the volume ratio of PS is almost one. In fact, some toluene will remain in the PS and not evaporate even after days. One should, however, consider that the distribution of PS in the drop is not homogeneous and thus the vapor pressure varies locally. The evaporation is high at the rim and thus the value of P_0' is dominated by the concentration of PS at the periphery.

First a qualitative interpretation for the formation of the concave structures is given. The crater-like structures formed at intermediate molecular weights can be understood by a vertical averaged radical flow model used for the interpretation of the coffee ring effect. For this the flow velocity profiles after three evaporation times (0 s, 1 s and 2 s) are calculated from **Eq. 21** (**Figure 56**).

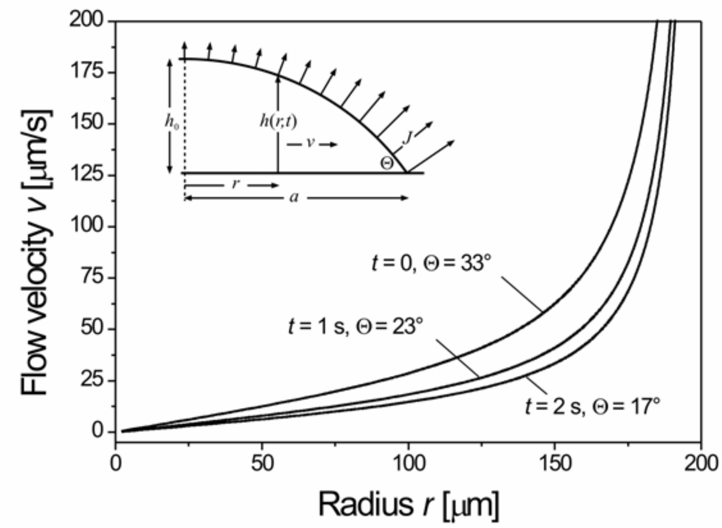

Figure 56 *Radial flow velocity in an evaporating drop calculated with* ***Eq. 21*** *at the beginning, 1 s, and 2 s after evaporation has started, for a toluene drop with an initial volume of 2 nL and an initial contact angle of 33° at room temperature*

The parameters used here were estimated from experiments of toluene drops evaporating on PS. We used $h_0 = 60$, 40, and 30 µm, $\theta = 33°$, 23°, and 17°, $\lambda = 0.39$, 0.43, and 0.45, $J_0 = 0.0044$, 0.004 and 0.0038 $\mathrm{kgm^{-2}s^{-1}}$, and $dh_0/dt = 26$, 15, and 11 µm/s, for $t = 0$, 1, and 2 s, respectively. To estimate J_0 from experimental results the integration of the flux is made over the whole drop surface: $\rho \cdot dV/dt \approx 4\pi\lambda J_0 a^2$. A value of $dV/dt \approx 10^{-12}\ \mathrm{m}^3/\mathrm{s}$ was taken from the experiments. At the top left a schematic of an evaporating drop illustrates the parameters. The extra volume in air at the drop rim leads to a higher evaporation rate, since the evaporating solvent molecules leave a larger diffusing space there. However, the total change in volume is limited at the pinned contact line. In the center, on the other hand, the evaporation rate is lower but the volume changes stronger.

The radial flow supplies the dissolution of polymer from the center to the drop periphery to compensate the difference. As a result there is an enhanced deposition of dissolved material in the edge region. The flow velocities are sufficiently high to transport a significant amount of material to the rim of the drop. Finally this leads to the formation of the concave structures observed.

4.2.2.4.2. Dependence of microstructures on the molar mass of PS in PS/toluene system

An influence of the molar mass on the resulting microstructures has been found for both, PS and PEMA. For PS, when the molar mass varies from 20.9 kDa to 1,400 kDa, the microstructure first shows a convex shape, then a dim in the center is formed, then a symmetric concave structure, then to asymmetric concave structures and finally locally protruded structures (**Figure 52**). The rim height increases with increasing molar mass of PS.

A slight shifting in the series microstructures between syringe technique and ink-jet technique can be observed (**Figure 47** and **Figure 52**). In the syringe system, Mexican hat like structures are found in 20.9 kDa and a dimple in the center is found for 62.5 kDa. However with ink-jet technique, the Mexican hat like structures are observed for both, 24.3 kDa and 29.6 kDa, a pile-up structure is found for 62.5 kDa.

To better understand why the evaporation structures vary with the molar mass of the polymer it is instructive to first analyze the time and then the length scales of different processes involved. As soon as the drop has spread on the surface, polymer starts to dissolve into the toluene. Polymer dissolution is slowed down by entanglement with increasing length of the polymer chain length. The entanglement molar mass of pure PS is M_e = 18.1-19.1 kDa[101, 102] Thus a disordered structures are resulted.

After dissolution the polymer diffuses in the liquid drop. Within $\Delta t = 1$ s, a characteristic time scale for the evaporation, a typical diffusion length is $\sqrt{6D\ \Delta t}$, where D is the diffusion coefficient of PS in toluene. It can be estimated from the phenomenological scaling law **Eq. 26**[78] and **Eq. 27** [76] (M_W in g/mol). For PS in toluene, $u = 0.65$, and $\alpha = 15$ [75]. The diffusion coefficient in the dilute regime is 1.2×10^{-10} m^2/s for M_W = 20.9 kDa and 1.1×10^{-11} m^2/s for M_W = 1445 kDa. Within one second a 20.9 kDa PS chain typically diffuses 27 µm. This is in the same order of magnitude as the height of drops (typically 60 µm at the beginning), but is significantly smaller than the radial extension of ≈200 µm. Thus, concentration gradients in vertical direction are at least partially equilibrated.

For a 1445 kDa PS molecule the diffusion length is 8 µm. In this case only little PS will reach the top of the drop by diffusion and strong concentration gradients can persist even in vertical direction. At the same time toluene will diffuse into the polymer, which leads to a swelling of the polymer. The diffusion of toluene in PS depends critically on the amount of toluene present. With increasing volume fraction of toluene and thus increasing degree of swelling of PS the toluene molecules become more and more mobile. At a polymer weight fraction of 0.7, the diffusion coefficient of toluene, as determined by NMR is 10^{-10} m^2/s[103]. For higher weight fractions, the diffusion is much slower. Extrapolating the experimental NMR results from higher temperature to room temperature a value of $D = 1.6\times10^{-13}$ m^2/s is estimated at a weight fraction of 0.89. Toluene molecules diffuse only a typical distance of ≈1 µm within one second. This corresponds to the length scale of the depth of craters.

The dependence of the microtopologies on the molar mass of PS can be also be understood if the overlap concentration C* is calculated for different molar mass (see the Chapter 2.2.3, **Figure 13**). PS with a low molar mass dissolves and diffuses faster than high molar mass PS. More polymer is dissolved in the toluene and it quickly diffuses to the top of the drop. As a result the overlap concentration, where polymer chains in solution overlap, is quickly reached. This critical concentration can be estimated from **Eq. 25,** where the radius of gyration is given by **Eq. 24** [75]. For 20.9 kDa PS we have C* ≈ 0.1 g/mL corresponding to a volume fraction of roughly 10%. The difference of the surface tension between pure toluene and the polymer solution remains nearly unchanged about ~ 2mN/m. Thus a Marangoni type effect is not significant to drive the polymer material to the drop wedge in order to form a rim. For a molar mass PS of 64.7kDa and 97.6 kDa, C* ≈ 0.035 g/mL, and the difference of the surface tension rises up to ~3 mN/m [104-106]. For 640 kDa, C* becomes only 0.006 g/mL, and a surface tension difference as higher as ~ 6 mN/m can be resulted[104]. Local Marangoni effect can be induced in higher molar mass. At this concentration, the overlapping PS chains start to become immobile and form a network. Further dissolution and diffusion of PS is hindered. At the same time the toluene molecules can still diffuse freely in the PS network; their diffusion coefficient is only reduced by 20% with respect to the value of pure toluene[103]. This will diminish or even stop the radial flow of polystyrene.

This can be proved by deposition of different numbers of droplets onto one spot of polymer surface. The more solvent onto polymer surface, the more polymer dissolves. For low molar mass PS, the dissolution is diffusion rate limiting process, significant solvent volume dependent of solvent penetration can be found, for the intermediate PS, the depth of microstructure increases, while for the high molar mass PS, since the dissolution rate is polymer chain disentanglement rate dependent, a roughness surface can be found and it declines with increasing solvent volume. The more droplets are placed, the higher the rim height of the structures and the smoother the surface structures become.

4.2.2.4.3. Crust formation

As a further conformation for the discussion mechanism of the formation of convex microstructures, especially for the lower molar mass PS, the convex structure turns into cracks after drying. It has been found that a crust should occur for sessile evaporating droplets containing polymer at higher concentration[24, 35, 83]. Similar crust like deposits were also observed when solvent mixtures, containing one low- and one high-boiling solvent evaporates on the soluble PS surface [34].

At low molar mass a high concentration of polymer appears owing to higher dissolution rate. For higher concentrations a convex microstructure after evaporation drop of polymer solution on insoluble substrate has been found. Characteristic for the formation of convex microstructure seems to be a crust formation on the top of the drop surface in an early shape of the evaporation. Therefore, the time needed for crust formation is estimated in comparison with the total evaporation time. The evaporation time τ_{ev} is much higher than crust growth time τ_g, since $\tau_{ev}/\tau_g \cong 2\times10^4$ [83, 107]. That means that the crust grows very fast in a short time scale. And the drop top surface becomes more and more polymer rich during the evaporation process and a gel-like shell forms thicker in the center and thinner in the periphery.

Cracks are discussed as the causes for an enhanced the polymer dissolution, when the polymer molar mass is below a certain value[72, 108, 109, 110]. In this case the dissolution rate of polymer is inversely proportional to the polymer molar mass. The cracks form as follows: the swollen polymer inside of the crust at the drop surface dries during the solvent evaporation, which finally leads to a decreasing solvent volume fraction. Simultaneously, the pinned drop tries to keep the original film shape and thus a tensional stress induced cracks formation. Thus one can summarized that for a low molar mass, the diffusion of solvent into the polymer network is rate-limiting, whereas a disentanglement of polymer determined the microstructure at the higher molar mass. Since polymer with higher molar mass has entangled chain, thus only a sufficient swelling will lead to dissolution[111].

4.2.2.4.4. Microstructuring of PEMA by drops of ethyl acetate

For the system of ethyl acetate on PEMA, higher roughness in the center of the concave microstructure is observed for all molar mass of PEMA. The roughness decreases with increasing drop numbers. This can be interpreted as: when many droplets are deposited onto the same spot of the polymer surface, the amount of solvent increases. The solid surface becomes soft due to the entrapped solvent inside of the polymer matrix after first droplet. The polymer changes from glass state into rubbery state by the first deposition of solvent drop. The second droplet can easily and quickly diffuse into this soft polymer and dissolution rate of polymer is enhanced with the increasing drop numbers. This additionally enhances the dissolution process of polymer into solvent.

Apparently, the dissolution behavior of the first deposited droplet for PS/toluene system proceeds as the same as the normal dissolution being described before[72, 79, 82], but a different dissolution process occurs in PEMA/ethyl acetate system . However, for both cases, a change of polymer from glass state into rubbery state can be announced.

When the drop dries with a pinned contact line a radial flow occurs to compensate the difference in volume change and evaporation rate across the drop shows a radius dependent for two kinds of systems. The radial flow supplied the dissolution of polymer from the center to the drop periphery. As a result there is an enhanced deposition of dissolved material in the edge region. The flow velocities are sufficiently high to transport a significant amount of material to the rim of the drop. Finally this leads to the formation of concave structure.

A first understanding of the difference to the system PS/toluene can be made by comparison of the flow velocity in the droplet with ink-jet technique. For PEMA/ethyl acetate, an initial height of h_0 = 11 µm, a typical contact radius and contact angle of a = 56 µm, and $\theta = 23°$, respectively, (known from the diameter of evaporation structures), and an initial volume of $V = 6\times10^4$ µm^3 (calculated from **Eq. 5**), leads to $\lambda = 0.427$, dh_0/dt = 36 µm/s and an evaporation time of $\Delta t \approx 0.27$ s. For PS/toluene system, the corresponding values were h_0 = 10 µm, a = 80 µm, $V = 10^5$ µm^3, $\theta = 14°$, $\lambda = 0.458$, dh_0/dt = 46 µm/s and $\Delta t \approx 0.35$ s. With a density of 900 kg/m^3 for ethyl acetate and 866 kg/m^3 for toluene, J_0 can be estimated as 0.012 kgm^{-2} s^{-1} and 0.0067 kgm^{-2} s^{-1} respectively. The reason for the higher evaporation rate of ethyl acetate is that the vapor pressure of ethyl acetate 12.6 kPa is higher, compared to the vapor pressure of 3.79 kPa for toluene (25°C). This leads to a higher flow velocity inside the drop (**Figure 57**).

In principle a higher flow velocity leads to a higher and sharper rim[33, 64]. For PEMA/ethyl acetate, the system has a higher flow velocity and lower dissolution rate. Thus PEMA has less time to dissolve and thus the concave structures form. The rim becomes higher at very higher molar mass because swelling is enhanced compared to dissolution. Overall, this leads to an extension of the range, in which concave structure can occur towards higher molar mass. Whereas for a lower dissolution rate, the possible to obtain a convex structure is less due to the slower penetration /diffusion rate of ethyl acetate into PEMA. A more extended swelling lead to a concave structure at higher molar mass.

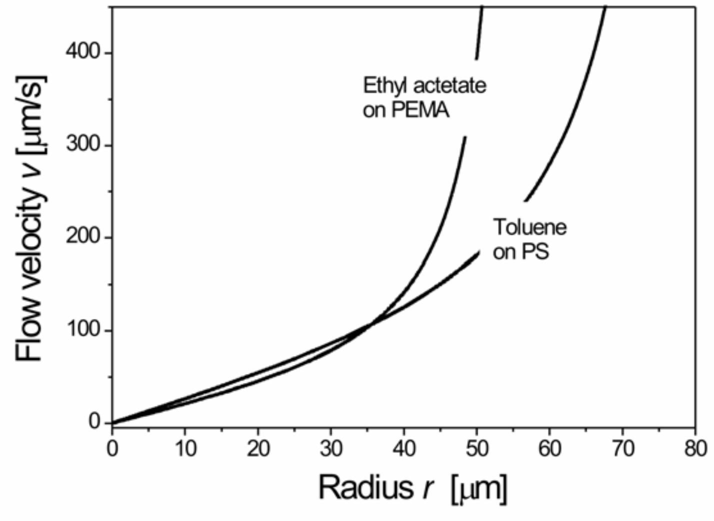

Figure 57 *Radial flow velocity in an evaporating drop calculated for the initial stage with* ***Eq.21*** *for toluene/PS and ethyl acetate/PEMA*

4.2.3 Microstructuring of polymer surfaces by evaporating solvent droplet in non-contact mode

The PEMA results have shown that an irreversible uptake of solvents might lead to an increase in the rim height for concave microstructures. To check this, I need a system with which I may vary the exposure time to the solvent without incorporating all the other processes in an evaporation droplet like dissolution and internal flow, leading to coffee ring effect. An ideal system to study this is the non-contact mode of the syringe system.

Commonly, the microstructure formation depends on the interplay of polymer dissolution, swelling, solvent evaporation and in additional, the way of drop deposition. However a microstructuring can be observed even if the droplet evaporates in the vicinity of the polymers surface without any contact between liquid and surface. In detail, the volume of a pendent drop is kept constant, while the solvent vapor diffuses through the air gap between droplet and polymer surface. This leads to a local softening of the polymer and a microstructures in form of a craters is found after the droplets is vanished.

The distance between droplet apex and polymer surface is maintained at 30 μm by adjusting the substrate position. The images in **Figure 58** show how the microtopologies vary with solvent exposure time of ~0 s, 15 s and 30 s, respectively. An increasing swollen polymer height can be clearly seen.

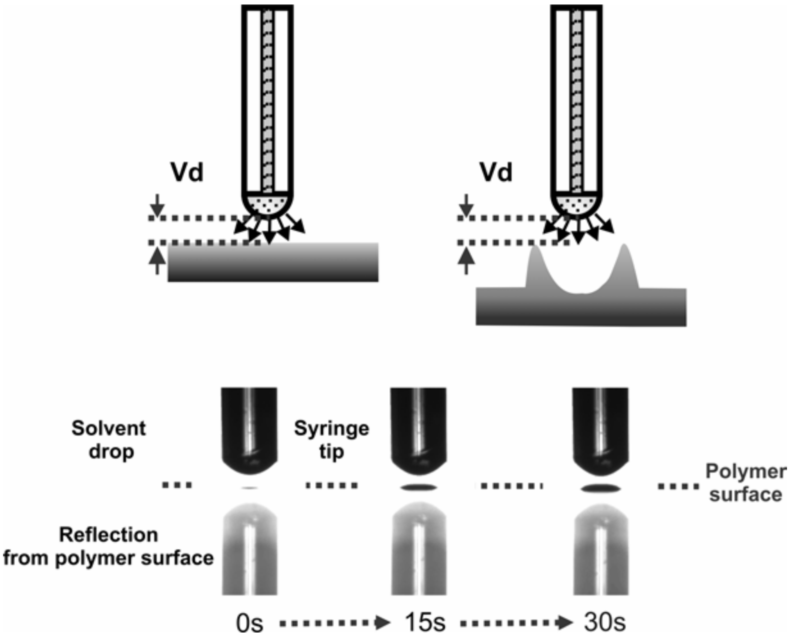

Figure 58 The sketch for describing the microstructure formation process by solvent vapor from pendent drop. Vd represents a distance of ~30μm between drop apex and polymer surface visualized by a optical microscopy. The optical images elucidate the generation process at interval of 0 s (the beginning), 15 s (the middle stage) and 30 s (the end).

The increases of the rim height of the microstructure with exposure time between 0.5 min and 20 min are shown (**Figure 59a)**. Typically three dimensional topologies after an exposure time of 2 min and 20 min are shown in the inset of **Figure 59a**. The cross section profiles of these microstructures are shown in black line. The maximum rim height and depth of the structure is about 33 μm and 12 μm respectively. The two inset images show an entopic structure is resulted with varies rim height in two perpendicular directions and it becomes more and more pronounce with increasing exposure time. **Figure 59b** shows the height profiles after keeping the substrates in vacuum for 7 days. Apparently, drying leads to a change of rim height and aspect ratio. Though the rim height decreases after drying, the aspect ratio increases. The drying is nearly completed after 1day.

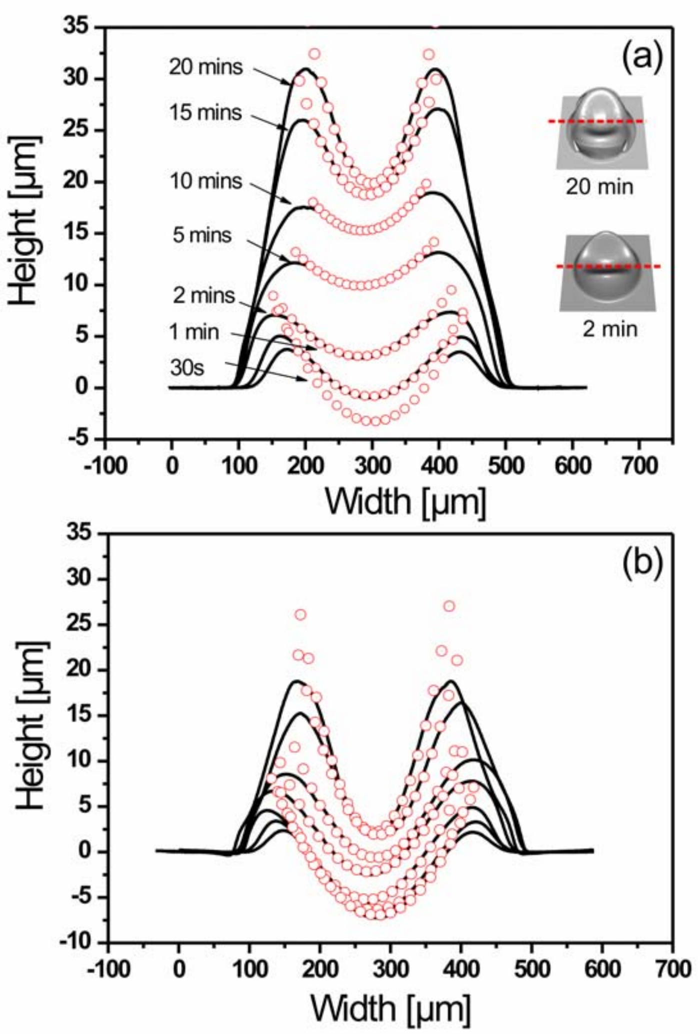

Figure 59 *Height profiles of micro-topologies in a PS surface after exposure to vapor of a toluene drop (non-contact mode) for different exposure times. The microstructures dried at ambient condition for 2 hours are shown in (a) and after 7 days in vacuum (b). The 3D topologies formed after an exposure time of 2 min and 20 min are shown as an inset in (a). The microstructures can be fit with parabolic lens shape (open circle).*

The rim height of dried microtopologies still increases with exposure time in spite of the diminishing rim height by drying in **Figure 60a**. The higher rim height reduces much more than the lower one. Although the aspect ratios level off at the exposure time between 0.5min and 10 min, the whole plot of the aspect ratio via exposure time shifts up, which is parallel to the line in non-dried condition **(Figure 60b)**. The influence of drying time after 1 day and 7 days shows no significant differences.

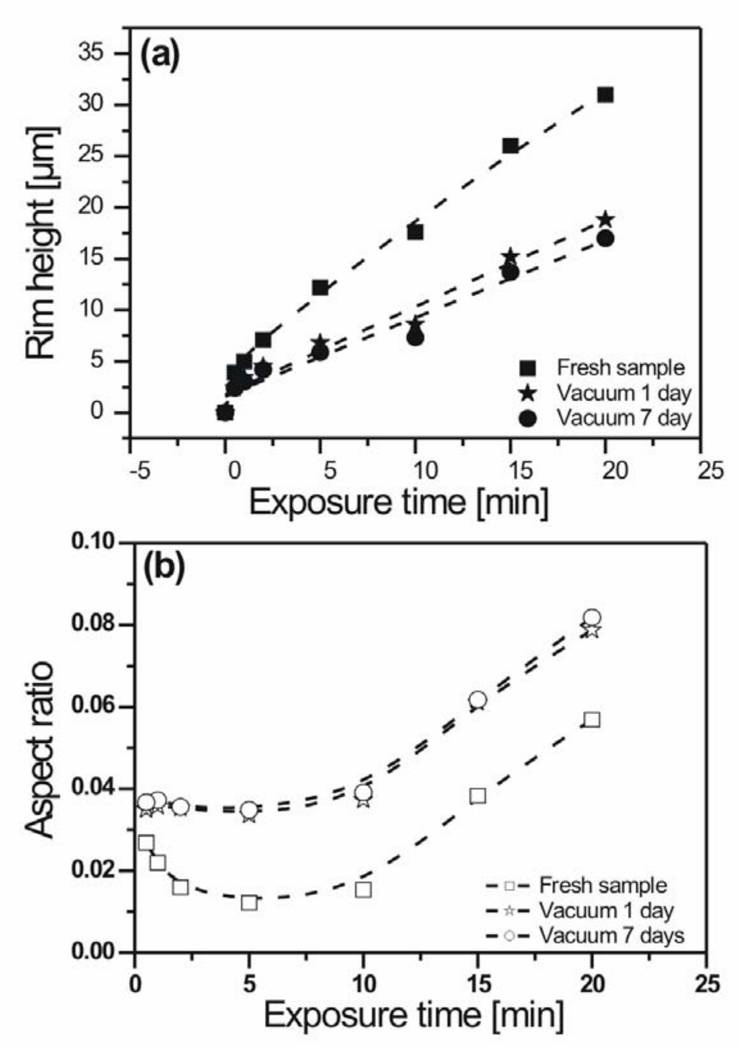

Figure 60 *Rim heights (a) and aspect ratio (b) of the correspondent microstructures versus exposure time to toluene vapor. The dashed lines in (a) are fit, based on diffusion laws as described in the text. The dash line in (b) is used for showing a tendency of the changes.*

Both fresh and dried microstructures can be fitted with a parabolic function than by circle function. The fit results including the χ^2 –parameter are compared for parabolic and circular line fit (**table 2**). All the structures can basically fit with a parabolic lens shape thus a potential application as a parabolic lens is possible.

χ^2	Circle fit	Parabolic fit
20 min	0.47	0.23
15 min	0.12	0.019
10 min	0.019	0.019
5 min	0.050	0.019
2 min	0.097	0.078
1 min	0.138	0.037
30 s	0.215	0.088

***Table 2** Comparison χ^2 with circle fit and parabolic fit*

To investigate what the effect of solvent uptake is, the heights of the structures obtained from non-contact mode were analyzed. Here solvent molecules diffuse through the air between droplet apex and polymer surface. This leads to polymer swelling. The resulting surface topology is similar to that for the contact mode but shows that it is uptaken permanently. The longer is the exposure time, the higher is the rim height. The dependence of rim heights (**Figure 60)** on the duration of exposure time to solvent could be described with an equation of the form $r_h \sim (t_e)^n$, which was derived from diffusion law as shown in **Eq. 28**, with r_h the rim height, t_e the exposure time and n an exponent between 0.5 (Fickian diffusion) and 1 (Case-II diffusion)[79, 81, 112, 113]. An exponent of n between 0.5 and 1 is regarded as anomalous diffusion. The exponent in this experiment was 0.46 and 0.65 for the higher and the lower rim height, respectively. This proves that, indeed, solvent diffusion into the polymer is relevant.

The structures show pronouncing differences before and after drying, despite the structure still remain entropic. For exposure time less than 10 min, the aspect ratios are nearly the same. This can be a cause of the reversible swelling process. After 10 min the entrapped solvent molecules are not able to leave the polymer network, thus a continuous increasing of aspect ratios is observed.

Accordingly, comparison between contact and non-contact mode reveals that the uptake of solvent in the polymer is about 15 times faster when a droplet is present. This can be concluded from the rim height. A height of 5 µm is reached after 4 s in contact mode, while it is reached after ~1 min for non-contact mode. In non-contact mode the solvent molecules have to diffuse through the air gap of ~30 µm. The time needed is $<X^2>/6D \approx 0.02$ ms. In this time the solvent molecules traveled. Here a diffusion coefficient of toluene D is 8 x10^{-6} m^2s^{-1}

4.2.4 Optical properties of microstructures

The microstructure with either concave or convex can be used as microlenses. The different shapes of the microstructure lead to a different the focus length (**Figure 61**). The structures can be used as a plano-concave microlens. It is found that V-shaped structures have a much smaller focus spot than U-shaped structures. The focus length, measured by shining a parallel light through each structure and then imaged by a camera system, varies from 3.4 mm to 8.5 mm from smaller structure with diameter of 360 µm to bigger structure with diameter of 760 µm. The dependence of the focusing length on the width & depth of the microstructures leads to the idea that the focal image can be used to analyze the surface topology of the microstructures in a simple way.

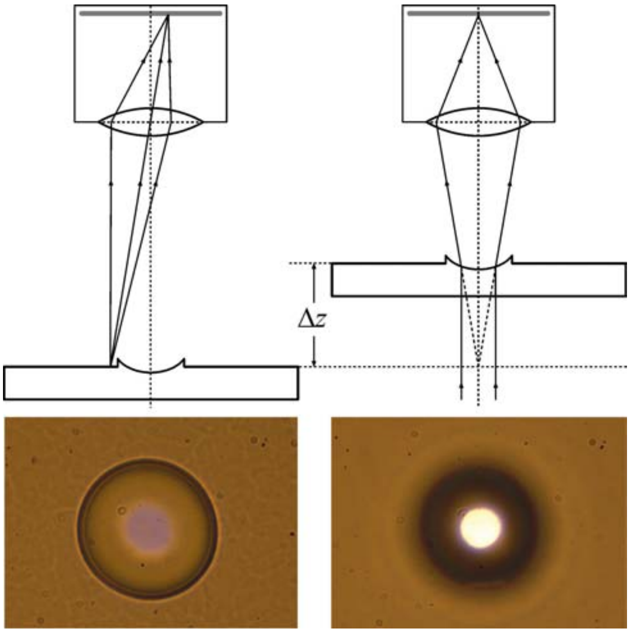

Figure 61 *Beam path for illuminating the optical diffraction properties of the microstructures in PS. Optical set-up for characterizing the shape and focus length of evaporation structures.*

For the polymer with different molar mass, the changes of microstructures give rise of the changes of optical properties. Here the microstructures are created by ink-jet technique on PS/toluene system.

Since the microstructures are created on transparent substrates one can investigate their optical properties acting as lenses. For observing the optical properties of the microstructures on PS, a modified laser scanning confocal microscopy (LSCM) was used (Chapter 3). **Figure 25** shows the modified system used to study the structures in transmitted and reflected light configuration simultaneously. LSCM has the ability to collect light from thin optical slices. By moving the focal plane perpendicular to the sample surface, a stack of slices can be created in order to extract three-dimensional images or cross-sections from different planes.

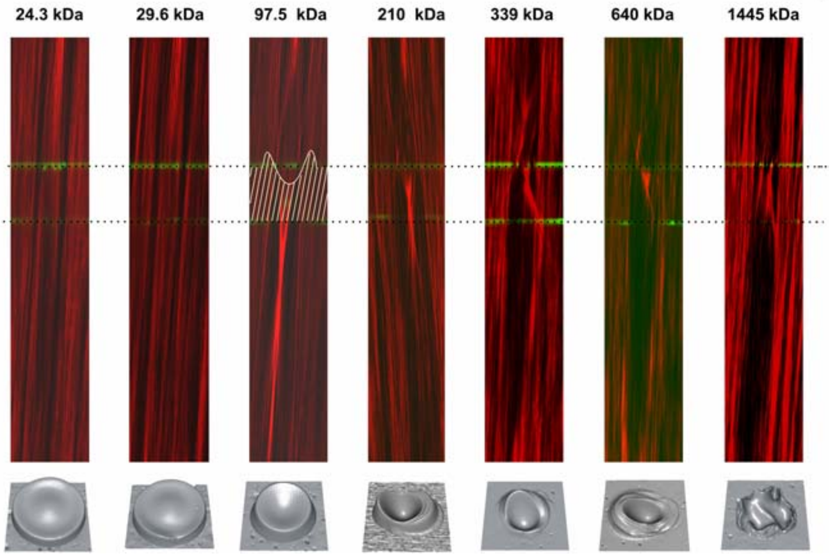

Figure 62 *The confocal images of the microstructures in polystyrene surface with molar masses ranging from 24.3 kDa to 1,445 kDa with correspondent three-dimensional topologies. The images represent X-Z sections from the center of merged stacks measured in transmission and reflection. The green horizontal lines indicate the reflected light from the upper and lower surface of the substrate, whereas the red light indicates the transmitted light.*

The substrates are placed into a motorized x-y stage above the objective with the microstructures facing down. For every structure studied, a stack with the volume of about 460 × 460 × 5600μm^3 was created starting from about 2.5 mm below the surface. The distance between the measured slices is about 35 µm. For each plane the red light and in the same time the green light was detected. From each stack a cross-section in the X-, Z- plane at the center of the microstructure was taken as shown (**Figure 25)**. The position of the upper and lower surface of the substrate, determined from the reflected light, is indicated in the figures and can be used as reference. For a better comparison with the correspondent three-dimensional topologies, cross-sections are displayed with the structure facing up for 97.5 kDa. As can be seen from **Figure 62** the complex shape of the microstructures that depends on the molar mass of the polymers and the number of droplets deposited results in a complex light propagation pattern. It should be emphasized at this point that the LSCM is a unique tool that allows this pattern to be recorded with micrometer accuracy.

4.3 Determination of Interfacial tensions in a microcapillary

In this section, I will show the determination of the interfacial tension in a microcapillary with a novel technique as described in Chapter 3.

4.3.1 Interfacial tension measurement between two immiscible pure liquids

In the following, the concerned liquids are assumed in the equilibrium state during the experiment, thus all obtained contact angle are static ones. As a cross-check interfacial tension were also calculated from dynamic contact angles. But physically unreasonable values were received in contrast to those from the static contact angles. **Figure 63 and Figure 64** show photographs taken for toluene, n-hexane, and chloroform in contact with water for acidic pre-treatment of the microchannels and aminosilanized ones, respectively.

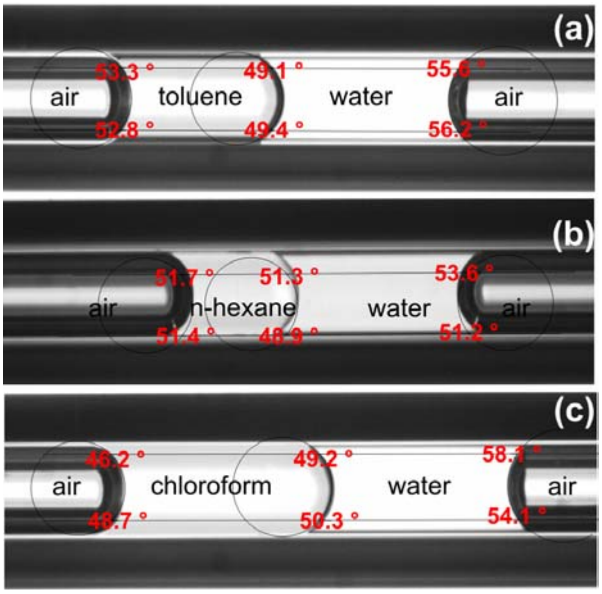

Figure 63 *Contact angle measurements for different liquids in contact in an acidic treated borosilicate microcapillary. (a) Air/toluene/water/air, (b) air/n-hexane/water/air, (c) air/chloroform/water/air (the two black lines shows the capillary diameter as 500 µm).*

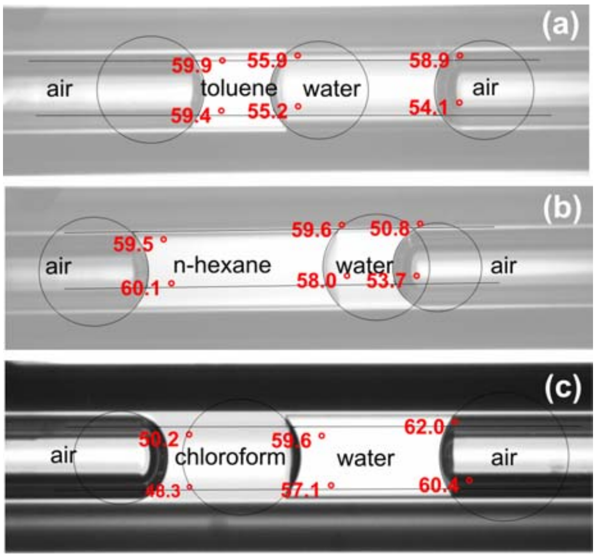

Figure 64 *Contact angles measured for different liquids in contact in an aminosilanized borosilicate microcapillary. A) Air/toluene/water/air, b) air/n-hexane/water/air, c) air/chloroform/water/air (the two black lines shows the capillary diameter as 500 µm). The contact angles of θ_1 θ_2 θ_3 for each solvent/water systems are obtained within one capillary.*

In each image the sequence of the media from left to right is air, organic solvent, water, and air. The right side is connected with the PTFE tube and the left side is open to air. The measured static contact angles for each system are shown in **table 3**.

Θ in acidic pre-treated microcapillary	Toluene	n-Hexane	Chloroform
θ_1 [deg.]	53.0	51.5	47.5
θ_2 [deg.] (H_2O)	55.9	52.4	56.1
θ_3 [deg.]	49.2	49.6	49.6
θ in aminosilanized microcapillary			
θ_1 [deg.]	56.5	52.2	49.2
θ_2 [deg.] (H_2O)	59.7	59.8	61.2
θ_3 [deg.]	55.6	58.8	58.3

Table 3 *Contact angles for toluene, n-hexane, and chloroform in contact with water in a borosilicate glass channel for two different glass surface pre-treatments. The contact angles have been determined as described in the experimental section and illustrated in* ***Figures 63*** *and* ***64***

Since toluene and hexane are non-polar solvents whereas chloroform is polar, the contact angles in the microcapillary decrease from toluene, to hexane and chloroform. However the contact angles of pure water are nearly constant in the acidic pre-treated microcapillary.

All contact angles for the acidic pre-treated glass capillary lie between 47.5 and 56.1 degree, those for the aminosilanized between 49.2 and 61.2 degree. For water the contact angles are 55 and 60 degree, respectively. This shows that the aminosilanized glass capillary is only slightly more hydrophobic and has a similar wettability as the acidic treated one. In contrast, it exhibits a contact angle hysteresis of about 20 degree, when moving the liquids back and forth. The calculated interfacial tensions of the two liquids in contact are shown in **table 4**. Data from literature are added for comparison[114, 115]. For both surface treatments the interfacial tensions are in good agreement with experimental data from literature.

Method	$\gamma_{L1/L2}$ [mN/m] L$_1$: Toluene L$_2$: Water	$\gamma_{L1/L2}$ [mN/m] L$_1$: n-Hexane L$_2$: Water	$\gamma_{L1/L2}$ [mN/m] L$_1$: Chloroform L$_2$: Water
Reference from literature	36.8	51.1	32.8
Reference from tensiometry K11	31.0	47.8	28.9
Acidic pre-treated microchannels	36.2	50.9	34.2
Aminosilanized microchannels	37.2	49.0	32.9

Table 4 *Base on the surface tension of toluene (γ_{L1} = 28.5 mN/m), n-hexane (γ_{L1} = 18.4 mN/m), and chloroform (γ_{L1} = 27.3 mN/m) in contact with water (γ_{L2} = 72.9 mN/m) taken from references[114-116], the interfacial tension between each liquid and water in a borosilicate glass channel for two different surface pre-treatments are calculated. Data from literature and tensiometer (K11, in Chapter 3) measurements are shown for comparison.*

The influence of adsorption of one liquid into another one was first examined with a 6 slugs in the sequence of water/air/ solvent/ water/air/solvent (**Figure 65**).

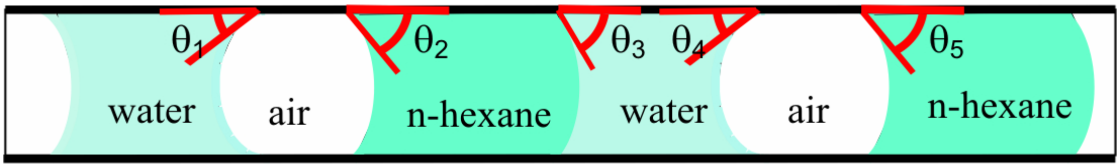

Figure 65 *The interfacial tensions are calculated by θ_2,, θ_3 and θ_4 in the six slugs. The air slug has a length of ~ 2cm and the two ends are opened to the air inside of the microcapillary.*

The contact angles are shown (**table 5**). The contact angles for pure water of the microcapillary change slightly with time. Especially for those on the left of capillary the contact angles increase. For n-hexane, the contact angle is nearly constant.

Time (min)	θ_1	θ_2	θ_3	θ_4	θ_5	Interfacial tension (mN/m)
Right after	49.0	51.5	50.5	51.5	52.0	53.4
30	52.0	51.5	52.0	51.0	51.0	56.4
60	51.0	51.5	51.5	51.5	50.0	55.7

Table 5 *The contact angles in the different interfaces are measured with time.*

The interfacial tensions are constant with increased time. However they are all higher than the interfacial tension measurement in two slugs.

To cross-check this, another two experiments were carried out with tensiometry in order to inspect the adsorption and mixing of n-hexane into pure liquid. The first experiment was performed by leaving a beaker (containing hexane) inside of ring tensiometry during the surface tension measurement of pure water. After 2 hours, the surface tension of the water was measured. No difference is observed comparing the surface tension of fresh water under ambient condition.

Subsequently, the influence of mixing is conducted by adding different amount of n-hexane into ~50 ml water and then measuring the water surface tension. The slight changes are observed when the amount of hexane increased up to 200 µl (**table 6**).

n-hexane in water (µl/50 ml)	Surface tension of pure water (mN/m)
0	72.9
5	72.5
10	72.6
50	72.4
200	71.7
400	70.6

Table 6 *The surface tension measurement of pure water containing different amount of n-hexane*

4.3.2 Interfacial tension measurement between a mixture and an immiscible solvent

Based on the system of pure immiscible solvents described above, the more complex case with one mixture of solvents and one pure solvent is investigated. Here I studied a slug of an ethanol/water mixture, adjacent to a Hexane slug. With **Eq. 35**, interfacial tension was calculated. In addition, I also determined the interfacial tension directly for the same system under the same conditions with ring tensiometry (K11, Krüss, Hamburg, Germany). The interfacial tensions versus percentage of ethanol in water are shown in **Figure 66.** The interfacial tension decreases with the ethanol percentage non-linearly. The maximum deviation between the two methods is roughly 6 mN/m.

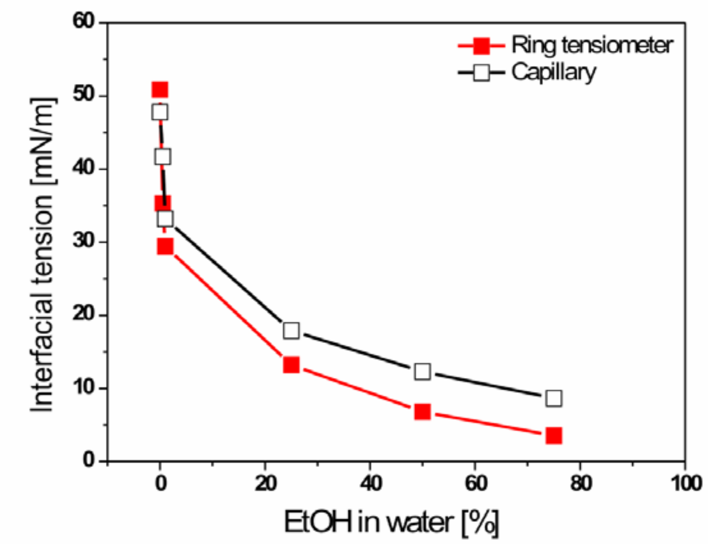

Figure 66 *The interfacial tension versus the mixing ratio of ethanol in water, for a slug of hexane in contact with a slug of a mixture of ethanol in water. The data are compared with data received from ring tensiometer.*

4.3.3 Measurement of interfacial tensions in a microcapillary

The interfacial tensions for two pure immiscible liquids measured with the presented method are consistent with the values obtained from spinning drop method[50]. In fact the surface hydrophilicity affects the accuracy of the interfacial tension. A deviation is observed in aminosilanized capillary, owing to the higher hystereis of glass surface. Beside this, other external parameter e.g. temperature, the hydrophilicity of the inner channel surface may affect the interfacial tension measurement.

A correction for the different temperatures, at which the measurements have been carried out, will presumably change the interfacial tension only slightly[117]. Both liquids show similar contact angles and the change of the surface tensions of the pure liquids with temperature is in the order of 0.1 mN/m/K[50, 116]. Thus, **Eq. 35** will provide a similar interfacial tension. As a result the presented method provides reasonable values for $\gamma_{L1/L2}$. This especially holds if considering the scattering of the data from literature.

Principally, the surface hydrophilicity of the channel wall has to be chosen such that the angle between the liquids is significantly lower or higher than 90 degree. As can be seen from **Eq. 39** the interfacial tension diverges for interfacial contact angle θ_3 of 90°. Usually, this can not occur since wetting of the glass surface is always favored by one of the immiscible liquids. Nevertheless, neither the hydrophilicity, nor the hydrophobicity must be too high to avoid completely wetting of inner glass surface by one of the liquids. In this case θ_1 and θ_2 could not be analyzed anymore. This is also confirmed by a test, in which the inner glass surface is hydrophobized with OTS to give contact angles of 90 degree for water. It is observed that even for a static interfacial contact angle lower than 90 degree, a reasonable interfacial tension can rarely derived for all three liquid-liquid systems. If the contact angle is close to 90°, the meniscus appears black. From the height *h* of the meniscus' apex and the radius *R* of the glass capillary, the contact angle can be calculated as

$$\theta = \pi / 2 - 2\,arctan(h / R) \qquad \text{Eq. 39}$$

For an optical resolution of 1 µm and a capillary radius of 250 µm, we get an error of about 0.45 degree. This can be improved with a better optical resolution or simpler with a higher capillary radius, as long as gravity can be neglected. A capillary radius of 500 µm, for example, provides an error of about 0.2 degree. The effect on the accuracy of the determination of the interfacial tension can be derived from **Eq 35**.

$$\Delta\gamma_{L1/L2} \approx \pm \frac{1}{\cos\theta_3}\left(2(\Delta\gamma)^2 + \left(\gamma_{L1}^2 + \gamma_{L2}^2 + \gamma_{L1/L2}^2\right)\cdot(\Delta\theta)^2\right)^{0.5} \qquad \text{Eq. 40}$$

Assuming that $\Delta\gamma_{L1} = \Delta\gamma_{L2}$ and $\Delta\theta_l = \Delta\theta$, i.e. the error for all interfacial tensions for all contact angles is the same. Additionally, all trigonometric functions were set to 1. Therefore, **Eq.40** provides rather a maximum error than the exact one.

The deviation of interfacial tension in 6 slugs can be due to the adsorption of n-hexane onto glass inner surface. Since the additional two experiments with tensiometer did not show much influences on the water surface tension measurement from either vapor adsorption or the solvent mixing.

When measuring the interfacial tension between a slug of ethanol/water and a slug of hexane, the interfacial tensions measured by both microcapillary and ring tensiometry are quite different. The lower values are found for all the measurement with ring tensiometry. Assuming that the contact angle is not zero when the force is taken, then $\cos\theta$ decreases, finally a higher interfacial tension is resulted (**Eq. 30**).

For the viscose and concentrated liquids, care should be taken during the measurement since the adsorption onto clean solid surface is significant higher and the liquid sticks to the surface. This also increases the risk of entrainment of one of the components during channel filling.

5 SUMMARY AND CONCLUSION

In this thesis, we investigated the evaporation of sessile microdroplets on different solid substrates. Three major aspects were studied: the influence of surface hydrophilicity and heterogeneity on the evaporation dynamics for an insoluble solid substrate, the influence of external process parameters and intrinsic material properties on microstructuring of soluble polymer substrates and the influence of an increased area to volume ratio in a microfluidic capillary, when evaporation is hindered.

In the first part, the evaporation dynamics of pure sessile water drops on smooth self-assembled monolayers (SAMs) of thiols or disulfides on gold on mica was studied. With increasing surface hydrophilicity the drop stayed pinned longer. Thus, the total evaporation time of a given initial drop volume was shorter, since the drop surface, through which the evaporation occurs, stays longer large. Usually, for a *single* drop the volume decreased linearly with $t^{1.5}$, t being the evaporation time, for a diffusion-controlled evaporation process. However, when we measured the total evaporation time, t_{tot}, for *multiple* droplets with different initial volumes, V_0, we found a scaling of the form $V_0 = a \cdot \mathrm{t}_{\mathrm{tot}}^{b}$. The more hydrophilic the substrate was, the more showed the scaling exponent a tendency to an increased value up to 1.6. This can be attributed to an increasing evaporation rate through a thin water layer in the vicinity of the drop. Under the assumption of a constant temperature at the substrate surface a cooling of the droplet and thus a decreased evaporation rate could be excluded as a reason for the different scaling exponent by simulations performed by F. Schönfeld at the IMM, Mainz.

In contrast, for a hairy surface, made of dialkyldisulfide SAMs with different chain lengths and a 1:1 mixture of hydrophilic and hydrophobic end groups (hydroxy versus methyl group), the scaling exponent was found to be ~ 1.4. It increased to ~ 1.5 with increasing hydrophilicity. A reason for this observation can only be speculated: in the case of longer hydrophobic alkyl chains the formation of an air layer between substrate and surface might be favorable. Thus, the heat transport to the substrate might be reduced, leading to a stronger cooling and thus decreased evaporation rate.

In the second part, the microstructuring of polystyrene surfaces by drops of toluene, a good solvent, was investigated. For this a novel deposition technique was developed, with which the drop can be deposited with a syringe. The polymer substrate is lying on a motorized table, which picks up the pendant drop by an upward motion until a liquid bridge is formed. A consecutive downward motion of the table after a variable delay, i.e. the contact time between drop and polymer, leads to the deposition of the droplet, which can evaporate. The resulting microstructure is investigated in dependence of the processes parameters, i.e. the approach and the retraction speed of the substrate and the delay between them, and in dependence of the intrinsic material properties, i.e. the molar mass and the type of the polymer/solvent system. The principal equivalence with the microstructuring by the ink-jet technique was demonstrated.

For a high approach and retraction speed of 9 mm/s and no delay between them, a concave microtopology was observed. In agreement with the literature, this can be explained by a flow of solvent and the dissolved polymer to the rim of the pinned droplet, where polymer is accumulated. This effect is analogue to the well-known formation of ring-like stains after the evaporation of coffee drops (coffee-stain effect). With decreasing retraction speed down to 10 µm/s the resulting surface topology changes from concave to convex. This can be explained with the increasing dissolution of polymer into the solvent drop prior to the evaporation. If the polymer concentration is high enough, gelation occurs instead of a flow to the rim and the shape of the convex droplet is received.

With increasing delay time from 0 ms to 1s the depth of the concave microwells decreases from 4.6 µm to 3.2 µm. However, a convex surface topology could not be obtained, since for longer delay times the polymer sticks to the tip of the syringe. Thus, by changing the delay time a fine-tuning of the concave structure is accomplished, while by changing the retraction speed a principal change of the microtopolgy can be achieved. We attribute this to an additional flow inside the liquid bridge, which enhanced polymer dissolution.

Even if the pendant drop is evaporating about 30 µm *above* the polymer surface without any contact (non-contact mode), concave structures were observed. Rim heights as high as

33 µm could be generated for exposure times of 20 min. The concave structure exclusively lay above the flat polymer surface outside the structure even after drying. This shows that toluene is taken up permanently. The increasing rim height, r_h, with increasing exposure time to the solvent vapor obeys a diffusion law of $r_h = r_{h0} \cdot t^n$, with n in the range of 0.46 ~ 0.65. This hints at a non-Fickian swelling process. A detailed analysis showed that the rim height of the concave structure is modulated, unlike for the drop deposition. This is due to the local stress relaxation, which was initiated by the increasing toluene concentration in the extruded polymer surface.

By altering the intrinsic material parameters i.e. the polymer molar mass and the polymer/solvent combination, several types of microstructures could be formed. With increasing molar mass from 20.9 kDa to 1.44 MDa the resulting microstructure changed from convex, to a structure with a dimple in the center, to concave, to finally an irregular structure. This observation can be explained if one assumes that the microstructuring is dominated by two opposing effects, a decreasing solubility with increasing polymer molar mass, but an increasing surface tension gradient leading to instabilities of Marangoni-type. Thus, a polymer with a low molar mass close or below the entanglement limit is subject to a high dissolution rate, which leads to fast gelation compared to the evaporation rate. This way a coffee-ring like effect is eliminated early and a convex structure results. For high molar masses the low dissolution rate and the low polymer diffusion might lead to increased surface tension gradients and a typical local pile-up of polymer is found. For intermediate polymer masses around 200 kDa, the dissolution and evaporation rate are comparable and the typical concave microtopology is found. This interpretation was supported by a quantitative estimation of the diffusion coefficient and the evaporation rate.

For a different polymer/solvent system, polyethylmethacrylate (PEMA)/ethylacetate (EA), exclusively concave structures were found. Following the statements above this can be interpreted with a lower dissolution rate. At low molar masses the concentration of PEMA in EA most likely never reaches the gelation point. Thus, a concave instead of a convex structure occurs.

At the end of this section, the optically properties of such microstructures for a potential application as microlenses are studied with laser scanning confocal microscopy.

In the third part, the droplet was confined into a glass microcapillary to avoid evaporation. Since here, due to an increased area to volume ratio, the surface properties of the liquid and the solid walls became important, the influence of the surface hydrophilicity of the wall on the interfacial tension between two immiscible liquid slugs was investigated. For this a novel method for measuring the interfacial tension between the two liquids within the capillary was developed. This technique was demonstrated by measuring the interfacial tensions between slugs of pure water and standard solvents. For toluene, n-hexane and chloroform 36.2, 50.9 and 34.2 mN/m were measured at 20°C, which is in a good agreement with data from the literature. For a slug of hexane in contact with a slug of pure water containing ethanol in a concentration range between 0 and 70 (v/v %), a difference of up to 6 mN/m was found, when compared to commercial ring tensiometry. This discrepancy is still under debate.

6 SUPPLEMENT

6.1 Abbreviations

Polystyrene	PS
Self assembled monolayers	SAMs
Poly ethyl methylacrylic	PEMA
Dodecanethiol	DDT, C12SH
11-mercapto-undecanol	HUT, OHC11SH
Asymmetric dialkyldisulfide derivatives	ADD
Constant contact angle	CCA
Constant contact radius	CCR
Tetrahydrofuran	THF
Octadecyltrichlorosilane	OTS
3-Aminopropyltriethoxysilane	APTE
Laser scanning confocal microscopy	LSCM
Scanning electron microscopy	SEM

6.2 List of figures

6.3 List of tables

6.4 Bibliography

Publication from this work:

- **Guangfen Li**, Hans-Jürgen Butt and Karlheinz Graf, “Microstructures by solvent drop evaporation on polymer surfaces: dependence on molar mass”, *Langmuir*, 22, 11395-11399, 2006,
- **Guangfen Li**, Norbert Höhn and Karlheinz Graf, “Micro-topologies in polymer surfaces by solvent drops in contact and non-contact mode”, Applied Physics Letters, 89, 241920, 2006,
- Tomas Haschke, Karlheinz Graf, Elmar. Bonaccurso, **Guangfen Li**, F.-T. Suttmeier and W. Wiechert, “Evaporation of Solvent Microdrops on Polymer Substrates: Crater Geometries and Parameter Sensitivity Analysis”, Proceedings of the Second International Conference on Transport Phenomena in Micro and Nanodevices, editor: M. Gad-el-Hak, Paper No. VIII-5, CD Publication, Engineering Conference International, Brooklyn, New York 2006.
- Tomas Haschke, Karlheinz Graf, Elmar, Bonaccurso, **Guangfen Li**, F.-T. Suttmeier and W. Wiechert, Evaporation of Solvent Microdrops on Polymer Substrate: From Well Controlled Experiments to Mathematical Models and Back, Accepted by NMTE, 2006

Submitted manuscript from this work:

- **Guangfen Li**, Hans-Jürgen Butt, Elmar Bonaccurso, Dimitry Golovko, Andreas Best, Karlheinz Graf, “Evaporation structures of solvent drops evaporating from polymer surfaces: influence of molar mass”, submitted to Macromol. Chem. Phys.
- H. Payer, T. Haschke, R. Reichardt, **Guangfen Li**, Karlheinz Graf, W. Wiechert, “Profile analysis of regularly miscrostructured surface”, submitted to Fluid dynamics & material processing

Patent:

- Karlheinz Graf, Norbert Höhn, **Guangfen Li**, Hans-Jürgen Butt**, “**Verfahren zur Bestimmung der Grenzflächenspannung zwischen zwei nicht mischbaren Flüssigkeiten”, Patentanmeldung EP 05 100 750. 8

1. Grimwood, P., Firefighting flow-rate. 2005
2. Corcoran, T.; Dauber, J.; Chigier, N.; Iacono, A. *Journal of aerosol medicine-deposition lcearance and effects in the drug* **2002,** 15, (3), 271-282.
3. Jing, J.; Reed, J.; Huang, J.; Hu, X.; Clarke, V.; Edington, J.; Housman, D.; Anantharaman, T.; Huff, E.; Mishra, B.; Porter, B.; Shenker, A.; Wolfson, E.; Hiort, C.; Kantor, R.; Aston, C.; Schwartz, D. *Proceedings of the National Academy of Sciences of the United States of America* **1998,** 95, (14), 8046-8051.
4. Bico, J.; Quere, D. *Europhysics Letters* **2000,** 51, (5), 546-550.
5. Zhao, B.; Viernes, N.; Moore, J.; Beebe, D. *Journal of the American Chemical Society* **2002,** 124, (19), 5284-5285.
6. Bergeron, V.; Quere, D. *Physics World* **2001,** 14, (5), 27-31.
7. Bertola, V. *Experiments in Fluids* **2004,** 37, (5), 653-664.
8. Conway, J.; Korns, H.; Fisch, M. *Langmuir* **1997,** 13, (3), 426-431.
9. Birdi, K. S.; Vu, D. T.; Winter, A. *Journal of Physical Chemistry* **1989,** 93, (9), 3702-3703.
10. Picknett, R. G.; Bexon, R. *Journal of Colloid and Interface Science* **1977,** 61, (2), 336-350.
11. Hu, H.; Larson, R. *Langmuir* **2005,** 21, (9), 3963-3971.
12. Petsi, A.; Burganos, V. *Physical Review E* **2006,** 73, (4), 041201(1-9).
13. Soolaman, D. M.; Yu, H. Z. *Journal of Physical Chemistry B* **2005,** 109, (38), 17967-17973.
14. Yu, H. Z.; Soolaman, D. M.; Rowe, A. W.; Banks, J. T. *Chemphyschem* **2004,** 5, (7), 1035-1038.
15. Yu, X.; Wang, Z.; Jiang, Y.; Zhang, X. *Langmuir* **2006,** 22, (10), 4483-4486.
16. Uno, K.; Hayashi, K.; Hayashi, T.; Ito, K.; Kitano, H. *Colloid and Polymer Science* **1998,** 276, (9), 810-815.
17. Sommer, A.; Ben-Moshe, M.; Magdassi, S. *Journal of Physical Chemistry B* **2004,** 108, (1), 8-10.
18. Chang, S.; Velev, O. *Langmuir* **2006,** 22, (4), 1459-1468.
19. Deegan, R. *Physical Review E* **2000,** 61, (1), 475-485.
20. Gonuguntla, M.; Sharma, A. *Langmuir* **2004,** 20, (8), 3456-3463.
21. Gorand, Y.; Pauchard, L.; Calligari, G.; Hulin, J.; Allain, C. *Langmuir* **2004,** 20, (12), 5138-5140.
22. Hashim, S.; Brooks, B. *Chemical Engineering Science* **2004,** 59, (11), 2321-2331.
23. Kajiya, T.; Nishitani, E.; Yamaue, T.; Doi, M. *Physical Review E* **2006,** 73, (1), 011601(1-5).
24. Pauchard, L.; Allain, C. *Europhysics Letters* **2003,** 62, (6), 897-903.
25. Pauchard, L.; Allain, C. *Comptes Rendus Physique* **2003,** 4, (2), 231-239.
26. Pauchard, L.; Allain, C. *Physical Review E* **2003,** 68, 052801(1-4).
27. Sefiane, K. *Journal of colloid and interface science* **2004,** 272, (2), 411-419.
28. Yakhno, T.; Yakhno, V.; Sanin, A.; Sanina, O.; Pelyushenko, A. *Technical Physics* **2004,** 49, (8), 1055-1063.
29. Chopra, M.; Li, L.; Hu, H.; Burns, M.; Larson, R. *Journal of Rheology* **2003,** 47, (5), 1111-1132.
30. Hu, H.; Larson, R. *Langmuir* **2005,** 21, (9), 3972-3980.
31. Nguyen, V.; Stebe, K. *Physical Review Letters* **2002,** 88, (164501), 164501(1-4).
32. von Bahr, M.; Tiberg, F.; Zhmud, B. *Langmuir* **2003,** 19, (24), 10109-10115.
33. Deegan, R.; Bakajin, O.; Dupont, T.; Huber, G.; Nagel, S.; Witten, T. *Nature* **1997,** 389, (6653), 827-829.
34. de Gans, B.; Schubert, U. *Langmuir* **2004,** 20, (18), 7789-7793.

35. Ozawa, K.; Nishitani, E.; Doi, M. *Japanese Journal of Applied Physics Part 1-Regular Papers Short Notes & Review Papers* **2005,** 44, (6A), 4229-4234.
36. Kawase, T.; Sirringhaus, H.; Friend, R.; Shimoda, T. *Advanced Materials* **2001,** 13, (21), 1601-1605.
37. Johnson, B. *Scientist* **1999,** 13, (19), 19-21.
38. Hoffmann, J. *Inovation Report: Forum für Wissenschaft, Industrie und Wirtsch* **2005**.
39. Bonaccurso, E.; Butt, H.; Hankeln, B.; Niesenhaus, B.; Graf, K. *Applied Physics Letters* **2005,** 86, (12), 124101(1-3).
40. Kavehpour, P.; Ovryn, B.; McKinley, G. *Colloids and surfaces A-physicochemical and engineering aspects* **2002,** 206, (1-3), 409-423.
41. Auroux, P.; Iossifidis, D.; Reyes, D.; Manz, A. *Analytical Chemistry* **2002,** 74, (12), 2637-2652.
42. Hong, J.; Quake, S. *Nature Biotechnology* **2003,** 21, (10), 1179-1183.
43. Manz, A.; Graber, N.; Widmer, H. *Sensors and Actuators B- Chemical* **1990,** 1, (1-6), 244-248.
44. Reyes, D.; Iossifidis, D.; Auroux, P.; Manz, A. *Analytical Chemistry* **2002,** 74, (12), 2623-2636.
45. Prakash, M.; Gershenfel, N. *Science* **2007,** 315, 832-835.
46. Fuerstman, M. J.; Garstecki, P.; Whitesides, G. M. *Science* **2007,** 315, 828-832.
47. Tokimoto, T.; Tsukahara, S.; Watarai, H. *Langmuir* **2005,** 21, (4), 1299-1304.
48. Song, H.; Tice, J.; Ismagilov, R. *Angewandte Chemie-International Edition* **2003,** 42, (7), 768-772.
49. Zhao, B.; Moore, J.; Beebe, D. *Science* **2001,** 291, (5506), 1023-1026.
50. Butt, H.-J.; Graf, K.; Kappl, M. Physics and Chemistry of Interfaces. Wiley-VCH, Weinheim, 2003.
51. McHale, G.; Rowan, S. M.; Newton, M. I.; Banerjee, M. K. *Journal of Physical Chemistry B* **1998,** 102, (11), 1964-1967.
52. Erbil, H.; McHale, G.; Newton, M. *Langmuir* **2002,** 18, (7), 2636-2641.
53. Erbil, H.; Meric, R. *Journal of Physical Chemistry B* **1997,** 101, (35), 6867-6873.
54. Hu, H.; Larson, R. G. *Journal of Physical Chemistry B* **2002,** 106, (6), 1334-1344.
55. Erbil, H.; McHale, G.; Rowan, S.; Newton, M. *Langmuir* **1999,** 15, (21), 7378-7385.
56. Erbil, H.; Avci, Y. *Langmuir* **2002,** 18, (13), 5113-5119.
57. Erbil, H. *Journal of Physical Chemistry B* **1998,** 102, (46), 9234-9238.
58. Shanahan, M. E. R.; Bourges, C. *International Journal of Adhesion and Adhesives* **1994,** 14, (3), 201-205.
59. Deegan, R.; Bakajin, O.; Dupont, T.; Huber, G.; Nagel, S.; Witten, T. *Physical Review E* **2000,** 62, (1), 756-765.
60. Li, G.; Hohn, N.; Graf, K. *Applied Physics Letters* **2006,** 89, (24).
61. Morozumi, Y.; Ishizuka, H.; Fukai, J. *Journal of Chemical Engineering of Japan* **2004,** 37, (6), 778-784.
62. Hu, H.; Larson, R. G. *The Journal of Physical Chemistry Letters B* **2006,** 110, 7090-7094.
63. Scriven, L.; Sternling, C. *Nature* **1960,** 187, (4733), 186-188.
64. Stupperich-Sequeira, C.; Graf, K.; Wiechert, W. *Mathematical and computer modelling of dynamcis systems* **2006,** 12, (4), 263-276.
65. Haschke, T.; Graf, K.; Bonaccurso, E.; Li, G.; Suttmeier, F.-T.; Wiechert, W. In *Evaporation of Solvent Microdrops on Polymer Substrates:Crater Geometries and Parameter Sensitivity Analysis*, Proceedings of the Second International Conference on Transport Phenomena in Micro

and Nanodevices, Brooklyn, New York, 2006; Gad-el-Hak, M., Engineering Conference International: Brooklyn, New York, 2006; No. VIII-5.

66. Ma, X.; Xia, Y.; Chen, E.; Mi, Y.; Wang, X.; Shi, A. *Langmuir* **2004,** 20, (22), 9520-9525.
67. Sugiyama, Y.; Larsen, R.; Kim, J.; Weitz, D. *Langmuir* **2006,** 22, (14), 6024-6030.
68. Voltz, C.; Stannarius, R. *Physical Review E* **2005,** 72, (1), 011705(1-8).
69. Wang, J.; Evans, J. *Physical Review E* **2006,** 73, (2), 021501(1-8).
70. Miller-Chou, B.; Koenig, J. *Progress in Polymer Science* **2003,** 28, (8), 1223-1270.
71. Ouano, A.; Carothers, J. *Polymer Engineering and Science* **1980,** 20, (2), 160-166.
72. Papanu, J.; Soane, D.; Bell, A.; Hess, D. *Journal of Applied Polymer Science* **1989,** 38, (5), 859-885.
73. Papanu, J.; Hess, D.; Soane, D.; Bell, A. *Journal of Applied Polymer Science* **1990,** 39, (4), 803-823.
74. Doi, M.; Edwards, S. F., *The theory of polymer dynamics*. ed.; Clarendon Press: Oxford, 1986;
75. Liu, R.; Gao, X.; Adams, J.; Oppermann, W. *Macromolecules* **2005,** 38, (21), 8845-8849.
76. Min, G.; Savin, D.; Gu, Z.; Patterson, G.; Kim, S.; Ramsay, D.; Fishman, D.; Ivanov, I.; Sheina, E.; Slaby, E.; Oliver, J. *International Journal of Polymer Analysis and Characterization* **2003,** 8, (3), 187-207.
77. Phillies, G. *Macromolecules* **1987,** 20, (3), 558-564.
78. Phillies, G. *Macromolecules* **1986,** 19, (9), 2367-2376.
79. McDonald, P.; Godward, J.; Sackin, R.; Sear, R. *Macromolecules* **2001,** 34, (4), 1048-1057.
80. Ugur, S.; Pekcan, O. *Journal of colloid and Interface Science* **2004,** 277, (2), 359-365.
81. Peppas, N.; Wu, J.; Vonmeerwall, E. *Macromolecules* **1994,** 27, (20), 5626-5638.
82. Sackin, R.; Ciampi, E.; Godward, J.; Keddie, J.; McDonald, P. *Macromolecules* **2001,** 34, (4), 890-895.
83. de Gennes, P. *European Physical Journal E* **2002,** 7, (1), 31-34.
84. Mukaiyama.T; Takahash.K. *Tetrahedron Letters* **1968,** 9, (56), 5907-5908.
85. Jonas, U.; del Campo, A.; Kruger, C.; Glasser, G.; Boos, D. *Proceedings of the National Academy of Science of the United States of America* **2002,** 99, (8), 5034-5039.
86. Seemann, R.; Brinkmann, M.; Kramer, E.; Lange, F.; Lipowsky, R. *Proceedings of the National Acedemy of Sciences of the United States of America* **2005,** 102, (6), 1848-1852.
87. Jordan, H.-J.; Brodmann, R.; Valentin, J.; Grigat, M. *Confocal white light microscopy*; p 1-4.
88. Nipkow disk. In *Wikipeida*, 2007
89. Flegler, S. L., John W. Heckman, Jr., and Karen L. Klomparens, *Scanning and Transmission Electron Microscopy*. ed.; W. H. Freeman and Company: New York, 1993.
90. Ulman, A. *Thin Solid Films* **1996,** 273, (1-2), 48-53.
91. Bain, C.; Evall, J.; Whitesides, G. *Journal of the America Chemistry Society* **1989,** 111, (18), 7155-7164.
92. Flores, S.; Shaporenko, A.; Vavilala, C.; Butt, H.; Schmittel, M.; Zharnikov, M.; Berger, R. *Surface Science* **2006,** 600, (14), 2847-2856.
93. Sefiane, K.; Tadrist, L. *Internataional communications in heat and mass transfer* **2006,** 33, (4), 482-490.
94. Haschke, T.; Graf, K.; Bonaccurso, E.; Li, G.; Suttmeier, F.-T.; Wiechert, W. *Proceedings of the Second International Conference on Transport Phenomena in Micro and Nanodevices* **2006**.
95. Bonaccurso, E.; Butt, H.; Graf, K. *European Polymer Journal* **2004,** 40, (5), 975-980.

96. Bowden, N.; Brittain, S.; Evans, A.; Hutchinson, J.; Whitesides, G. *Nature* **1998,** 393, (6681), 146-149.

97. Buscher, K.; Berger, R.; Brunger, W.; Graf, K. *Microelectronic Engineering* **2006,** 83, (4-9), 819-822.

98. Katzenberg, F. *Surface & Coatings Technology* **2005,** 200, (1-4), 1097-1100.

99. Stafford, C.; Harrison, C.; Beers, K.; Karim, A.; Amis, E.; Vanlandingham, M.; Kim, H.; Volksen, W.; Miller, R.; Simonyi, E. *Nature Materials* **2004,** 3, (8), 545-550.

100. Hao, W.; Elbro, H. S.; Alessi, P., *Polymer Solution Data Collection. Part 1: Vapor-Liquid Equilibria*. ed.; Dechema: Frankfurt, 1992.

101. Brandrup, J.; Immergut, E. H.; Grulke, E. A. *Polymer Handbook*. John Wiley & Sons, USA, 1999.

102. Fetters, L. J.; Lohse, D. J.; Milner, S. T.; Graessley, W. W. *Macromolecules* **1999,** 32, 6847-6851.

103. Pickup, S.; Blum, F. *Macromolecules* **1989,** 22, (10), 3961-3968.

104. Cerpa-Gallegos, M.; Jasso-Gastinel, C.; Lara-Valencia, V.; Gonzalez-Ortiz, L. *Langmuir* **2005,** 21, (17), 7726-7732.

105. Ober, R.; Paz, L.; Tapin, C.; Pincus, P.; Bollieau, S. *Macromolecules* **1983,** 16, (1), 50-55.

106. Redon, C.; Ausserre, D.; Rondelez, F. *Macromolecules* **1992,** 25, (22), 5965-5969.

107. de Gennes, P. *European Physical Journal* **2001,** 6, (5), 421-424.

108. Ueberreiter, K.; Asmussen, F. *Journal of Polymer Science* **1957,** 23, (103), 75-81.

109. Miller-Chou, B.; Koenig, J. *Macromolecules* **2003,** 36, (13), 4851-4861.

110. Ueberreiter, K.; Asmussen, F. *Journal of Polymer Science* **1962,** 57, (165), 187.

111. Parsonage, E.; Peppas, N.; Lee, P. *Journal of Vacuum Science & Technology B* **1987,** 5, (2), 538-545.

112. Koenig, J. *Advanced Materials* **2002,** 14, (6), 457-460.

113. Ribar, T.; Bhargava, R.; Koenig, J. *Macromolecules* **2000,** 33, (23), 8842-8849.

114. Freitas, A. A.; Quina, F. H.; Carroll, F. A. *Journal of Physical Chemistry B* **1997,** 101, (38), 7488-7493.

115. Weast, R. C., *CRC Handbook of chemistry and physics*. 64th ed.; CRC press: Boca Raton, 1983-1984.

116. Adamson, A. W. *Physical chemistry of surfaces*. John Wiley & Sons, New York, 1990.

117. Chavepeyer, G.; Desaedeleer, C.; Platten, J. *Journal of Colloid and Interface Science* **1994,** 167, (2), 464-466.